

Four distinct trajectories of tau deposition identified in Alzheimer's disease

Jacob W. Vogel¹, Alexandra L. Young², Neil P. Oxtoby^{3,4}, Ruben Smith^{5,6}, Rik Ossenkoppele^{5,7}, Olof T. Strandberg⁵, Renaud La Joie⁸, Leon M. Aksman^{3,9}, Michel J Grothe^{10,11}, Yasser Iturria-Medina¹, the Alzheimer's Disease Neuroimaging Initiative^{*}, Michael J. Pontecorvo¹², Michael D. Devous¹², Gil D. Rabinovici^{8,13}, Daniel C. Alexander^{3,4}, Chul Hyung Lyou¹⁴, Alan C. Evans¹, and Oskar Hansson^{5,15}

¹ Montreal Neurological Institute, McGill University, Montréal, QC, Canada

² Department of Neuroimaging, Institute of Psychiatry, Psychology and Neuroscience, King's College London, London, UK.

³ Centre for Medical Image Computing, University College London, London, WC1E 6BT, UK

⁴ Department of Computer Science, University College London, London, WC1E 6BT, UK

⁵ Clinical Memory Research Unit, Lund University, Lund, Sweden

⁶ Department of Neurology, Skåne University Hospital, Lund, Sweden

⁷ Alzheimer Center Amsterdam, Department of Neurology, Amsterdam Neuroscience, Vrije Universiteit Amsterdam, Amsterdam UMC, Amsterdam, The Netherlands

⁸ Memory and Aging Center, Department of Neurology, Weill Institute for Neurosciences, University of California, San Francisco, San Francisco, CA

⁹ Department of Medical Physics and Biomedical Engineering, University College London, London, WC1E 6BT, UK

¹⁰ Wallenberg Centre for Molecular and Translational Medicine, University of Gothenburg, Gothenburg, Sweden

¹¹ Instituto de Biomedicina de Sevilla, Hospital Universitario Virgen del Rocío/CSIC/Universidad de Sevilla, Seville, Spain

¹² Avid Radiopharmaceuticals, Philadelphia, PA, USA

¹³ Department of Radiology and Biomedical Imaging; University of California, San Francisco, San Francisco, CA

¹⁴ Departments of Neurology, Gangnam Severance Hospital, Yonsei University College of Medicine, Seoul, Republic of Korea

¹⁵ Memory Clinic, Skåne University Hospital, Malmö, Sweden

* Data used in preparation of this article were obtained from the Alzheimer's Disease Neuroimaging Initiative (ADNI) database (adni.loni.usc.edu). As such, the investigators within the ADNI contributed to the design and implementation of ADNI and/or provided data but did not participate in analysis or writing of this report. A complete listing of ADNI investigators can be found at: https://adni.loni.usc.edu/wp-content/uploads/how_to_apply/ADNI_Acknowledgement_List.pdf

Abstract: Alzheimer's disease (AD) is characterized by spread of tau pathology throughout the cerebral cortex. The spreading pattern was thought to be fairly consistent across individuals, though recent work has demonstrated substantial variability in the AD population. Using tau-PET scans from 1612 individuals, we identified four distinct spatio-temporal trajectories of tau pathology, ranging in prevalence from 18 to 33%. We replicated previously described limbic-predominant and medial temporal lobe-sparing patterns, while also discovering posterior and lateral temporal patterns resembling atypical clinical variants of AD. These "subtypes" were stable during longitudinal follow-up, and were replicated in a separate sample using a different radiotracer. The subtypes presented with distinct demographic and cognitive profiles, and differing longitudinal outcomes. Additionally, network diffusion models implicated that pathology originates and spreads through distinct corticolimbic networks in the different subtypes. Together, our results suggest variation in tau pathology is common and systematic, perhaps warranting a re-examination of the notion of "typical AD", and a revisiting of tau pathological staging.

Correspondence: jacob.vogel@mail.mcgill.ca; oskar.hansson@med.lu.se

Introduction

Alzheimer's disease (AD) is the leading cause of dementia worldwide and prevalence is expected to double in the next twenty years¹. At autopsy, AD presents with diffuse extracellular and neuritic amyloid- β (A β) plaques, and intracellular neurofibrillary tangles and neuropil threads of hyperphosphorylated tau, along with extensive neurodegeneration^{2,3}. Leading hypotheses have postulated these two hallmark proteins, A β and tau, either alone or in combination, are causative agents in disease etiology and progression^{4,5}. Cortical tau colocalizes with cortical atrophy and predicts future neurodegeneration⁶, while the appearance of tau in specific cognitive networks leads to domain-specific cognitive impairments⁷. Recently, the focus of treatment discovery has shifted to tau, and numerous therapeutic interventions are currently undergoing research and development. A better understanding of tau pathophysiology is therefore of imminent need in order to aid development of these interventions.

51 Tau tangles are thought to exhibit a stereotypical pattern of cortical spread, which has been formal-
52 ized into the Braak staging system^{8,9}. The six Braak stages describe the first appearance of cortical tau
53 tangles in the transentorhinal cortex, subsequent spread throughout the medial and basal temporal lobes,
54 then into neocortical associative regions, and finally into the unimodal sensory and motor cortex⁹. While
55 this stereotyped progression was derived from histopathological staining at autopsy, tau can now be
56 measured *in vivo* in the human brain using positron emission tomography (PET). Early tau-PET imaging
57 studies described average spatial patterns that have mostly converged with the Braak staging system^{10,11}.

58 However, many examples have emerged of individual tau patterns that do not fit neatly into the
59 Braak staging system. A medial temporal lobe (MTL)-sparing phenotype with extensive cortical tau burden
60 but limited MTL burden has been described, as well as a limbic-predominant phenotype with most promi-
61 nent tau pathology in limbic and medial temporal cortex, which were found to be associated with specific
62 patient profiles¹²⁻¹⁴. In addition, clinical variants of AD have been described that exhibit specific patterns
63 of pathology that deviate from the Braak staging scheme¹⁵, e.g., posterior cortical atrophy (PCA)¹⁶, log-
64 penic primary progressive aphasia (lvPPA)¹⁷, and others¹⁸. These latter clinical variants of AD are relatively
65 uncommon and most frequently associated with early-onset AD, but represent another example of atyp-
66 ical tau patterning.

67 Taken together, the examples above suggest that, while the Braak staging system appears to be a
68 good description of tau spreading at the population level, it does not account for systematic variability at
69 the individual level. Variation in tau patterning may be indicative of distinct underlying neurobiology^{19,20},
70 which may affect treatment response. Different subtypes may also have distinct rates and profiles of cog-
71 nitive decline^{21,22}, potentially affecting clinical trials. For these reasons, a systematic description of varia-
72 tion in AD pathological spread is needed. Previous studies have provided invaluable information toward
73 this effort^{12,13,23-26}, but carry certain limitations. Pathology studies, for example, are limited by spatial
74 sampling and semi-quantitation. Neuroimaging studies overcome some of those limitations, but often use
75 non-specific measurements, and rely on methods designed to parse spatial rather than spatiotemporal
76 variation.

77 Here we present a systematic characterization of heterogeneity in tau patterning in AD. We
78 amassed the largest and most diverse sample of tau-PET data to date (n=2324), covering the full clinical
79 spectrum from asymptomatic through mild cognitive impairment (MCI) to AD dementia, allowing unprec-
80 edented power to detect and characterize AD subtypes. We fit this data using the Subtype and Stage In-
81 ference (SuStaln) model, a paradigm-shifting algorithm that combines disease progression modeling with
82 traditional clustering to achieve probabilistic spatiotemporal partitioning and classification²³. SuStaln re-
83 quires only cross-sectional datasets to automatically detect multiple spatiotemporal trajectories, and it
84 provides probabilistic and quantitative information for individualized inference. We apply SuStaln to our
85 multi-cohort sample of tau-PET data to discover systematic spatiotemporal variation in tau spreading. We
86 validate the subtypes across different PET radiotracers, and we validate the progression patterns using
87 serial longitudinal tau-PET data.

88 **Results**

89 We compiled an initial sample of 1667 individuals with flortaucipir-PET tau images, spanning five separate
90 cohorts. 1143 individuals were identified as either cognitively normal (n=707), or showed biomarker evi-
91 dence for A β pathology (A β + MCI, n=223; A β + AD dementia, n=213), and were used as a discovery sample
92 for subsequent analysis. Demographic information and cross-cohort comparisons can be found in Table
93 [S1](#).
94
95

96 **Spatiotemporal subtypes of Alzheimer's disease.** We applied the SuStaln algorithm (Extended Data Fig.
97 S1a) to the 1143 flortaucipir-PET images in order to extract distinct spatiotemporal trajectories of tau
98 spreading. As expected, many individuals (n=700; 61%) did not demonstrate any abnormal tau-PET signal,
99 and were therefore automatically assigned to a tau-negative group (S0) (see Supplementary Note 1). Us-
100 ing cross-validation, we determined a four-subtype solution to best represent the remaining data (n=443;

101 See Methods, Extended Data Fig. S1c-f). The four-subtype model was applied to probabilistically assign
102 individuals to one of 30 progressive stages along one of the four subtype trajectories (Fig 1).

103 The distribution of clinical diagnoses across stages and subtypes can be found in Extended Data
104 Fig. S2f,g,i. 145 (32.7%) individuals exhibited a limbic-predominant phenotype, with a Braak-like spatial
105 progression across SuStaln stages (S1: Limbic). An additional 79 individuals (17.8%) expressed a parietal-
106 dominant and MTL-sparing phenotype, where early precuneus binding accumulated across temporoparietal
107 and frontal cortex, but with relative sparing of the MTL (S2: MTL-Sparing). The third subtype composed
108 135 (30.5%) individuals with a predominant posterior occipitotemporal phenotype, involving early occipi-
109 tal lobe binding and gradual anterior progression across SuStaln stage (S3: Posterior). The remaining 84
110 (19.0%) individuals showed a temporoparietal phenotype with distinct left-sided lateralization, character-
111 ized by early left-temporal tau eventually spreading to parietal and frontal cortex across disease stage (S4:
112 Lateral [L] Temporal). The differences highlight inconsistencies between tau-PET binding and pathological
113 sequencing of specific brain regions found in previous studies, such as the hippocampus, lingual gyrus and
114 insula^{10,11,27}, which exhibited different binding patterns across subtypes (Extended Data Fig. S3).

115
116 **Stability of AD subtypes.** While variation in subtype proportion was observed (and expected) across co-
117 horts, all subtypes were represented across all cohorts (Extended Data Fig. S4). Most individuals fell neatly
118 into the stereotypical progression of each subtype (Fig 1b), allowing a clean stepwise progression across
119 tau abnormality events to be observed across each subtype population (Extended Data Fig. S5). 12% of
120 individuals did not fall cleanly into any subtype due to having either too little or too much pathology, both
121 of which are uninformative for subtype (Fig 1b, Extended Data Fig. S2d,h). In general, early stage and cog-
122 nitively normal individuals were assigned to subtypes with less confidence, though median subtype prob-
123 ability neared 100% by SuStaln stage 7 (Extended Data Fig. S2e), and by the MCI clinical stage (Extended
124 Data Fig. S2h). This provides evidence that the earliest phases of each subtype may overlap, or that they
125 are difficult to distinguish above measurement error. We further confirmed that the subtypes produced
126 by SuStaln were not driven by, or specific to, arbitrary user inputs relating to the anchoring of regional
127 pseudotimes (Methods, Extended Data Fig. S6).

128 We next assessed whether the same subtypes could be derived within a separate replication sample
129 of 469 individuals scanned with the RO948 tau-PET tracer. The replication cohort, BioFINDER II²⁸, is de-
130 scribed in Supplementary Table S1. SuStaln was run separately on these individuals, constraining the anal-
131 ysis to produce four subtypes. Three of the four replication subtypes greatly resembled those derived in
132 the discovery sample (Fig 2). The only exception involved the S4: L Temporal subtype, which had a similar
133 overall tau-PET pattern but involved right-sided rather than left-sided lateralization. Further analysis de-
134 termined that this related to the smaller sample size rather than the differing radiotracer, and further
135 suggested that the S4: L Temporal subtype has a consistent overall pattern but a high propensity for
136 marked lateralization (see Supplemental Note 2, Extended Data Fig. S7).

137
138 **Subtypes characterized by distinct clinical profiles.** Next, we compared demographic, cognitive and genetic
139 (i.e. APOE4 status) variables between the subtypes and the tau-negative S0 group (Table 1). Individuals
140 across all four subtypes expressed worse MMSE and worse memory scores compared to S0 individuals. In
141 addition, all subtypes except S1 (Limbic) had worse global cognitive composite scores, individuals across
142 all subtypes except S2 (MTL-Sparing) were more likely to be APOE4 carriers, and all subtypes except S4 (L
143 Temporal) were more likely to be female, compared to S0 individuals. Compared to tau-negative individu-
144 als in S0, S1 and S3 were older, S2 exhibited poorer executive function, S2 and S3 exhibited poorer
145 visuospatial function, and S4 had worse language scores.

146 Compared to other subtypes (i.e., other tau-positive individuals), individuals within the S1 (Limbic)
147 subtype were more likely to be APOE4 carriers, had less overall tau with a more right-sided pattern, and
148 had better overall cognition, but worse memory relative to their overall cognition. S2 (MTL Sparing) indi-
149 viduals were younger, less likely to carry an APOE4 allele, had more overall tau burden, had a more right-
150 sided tau pattern and had worse relative executive function, compared to other subtypes. S4 (L Temporal)
151 individuals had more overall tau with a more left-lateralized pattern. These individuals also trended at

152 having worse overall cognition, but had better relative memory and worse relative language scores com-
153 pared to other subtypes. Finally, individuals with the S3 (Posterior) subtype did not exhibit any significant
154 cognitive, demographic or *APOE4* differences compared to the other subtypes. These relationships (after
155 adjustment for demographics, diagnosis, cohort and SuStaln stage) are described in Table 1 and visualized
156 in Extended Data Fig. S8.

157 Each individual was assigned a stage along their respective subtype trajectory. As expected, increas-
158 ing SuStaln stage was associated with worse global cognition as measured with MMSE ($r=0.54$, $p<0.0001$;
159 Fig 3a). This relationship was consistent across all subtypes (S1: $r = -0.51$, S2: $r = -0.53$, S3: $r = -0.64$, S4: $r =$
160 -0.40 , all $p<0.001$). A strong negative relationship between SuStaln stage and age was also observed, such
161 that individuals at later SuStaln stages tended to be younger ($r = -0.59$, $p<0.0001$). This relationship was
162 again consistent across all subtypes, though less prominent for S1 (S1: $r = 0.20$, S2: $r = -0.68$, S3: $r = -0.64$,
163 S4: $r = -0.73$, all $p<0.05$; Fig 3b). This inverse relationship was also present among individuals both 65 and
164 younger ($n = 100$, $r = -0.43$, $p < 0.0001$) and individuals older than 65 ($n = 342$, $r = -0.28$, $p < 0.0001$), sug-
165 gesting the effect is not driven purely by early onset cases. Lateralization also increased with increasing
166 SuStaln stage (Extended Data Fig. S9). However, despite trends in lateralization at higher SuStaln stage,
167 many individuals were observed with a “reversed” lateralization compared to the group average tau lat-
168 eralization patterns for their subtype (Extended Data Fig. S9), suggesting lateralization to be at least par-
169 tially orthogonal with subtype.

170
171 **Cognitive prognosis of AD subtypes.** Longitudinal MMSE data was available for a subset of 697 individuals
172 (mean follow-up = 1.74 years from PET scan, $sd = 0.64$). Individuals with the S3 (Posterior) subtype had
173 significantly slower decline compared to all other subtypes independently (S1: $t=2.03$, $p=0.043$; S2: $t=2.88$,
174 $p=0.004$; S4: $t=4.83$, $p<0.0001$), as well as in a one vs all analysis ($t=3.64$, $p=0.0003$; Fig 3c). This finding
175 persisted across different clinical diagnoses (Fig 3d, Supplemental Table S2), and was confirmed through a
176 meta-analysis across the five cohorts, which also showed a significantly slower decline for the S3 (Posterior)
177 group ($t=1.67$, $p=0.047$; Fig 3e). Individuals with the S4 (L Temporal) subtype additionally showed
178 steeper cognitive decline compared to S1 (Limbic) subtype individuals ($t=3.40$, $p=0.0008$), and generally
179 showed faster decline compared to other subtypes in a one vs all analysis ($t=-4.49$, $p<0.0001$) and across
180 clinical diagnoses (Fig 3d, Supplementary Table S2). A meta-analysis once again confirmed a significant
181 overall effect ($t=1.88$, $p=0.031$; Fig 3e).

182
183 **Stability and progression of AD subtypes over time.** SuStaln uses cross-sectional data to infer longitudinal
184 trajectories for the tau data, so evaluating how well longitudinal data fits the model is a key aspect of val-
185 idation. 519 individuals from the discovery sample also had follow-up flortaucipir-PET scans (mean follow-
186 up time = 1.42, $sd = 0.58$, years). Overall, 88.5% of individuals exhibited the same subtype at both baseline
187 and follow-up, or progressed from S0 into a subtype (Fig 3f). Stability when excluding individuals classified
188 as S0 at baseline (tau-positive stability) and follow-up was 83.9%. Stable individuals were classified with a
189 higher degree of confidence at baseline compared to individuals whose subtype changed at follow-up
190 (stable mean = 0.91, $sd = 0.17$; change mean = 0.74, $sd = 0.27$; $t = 5.26$, $p < 0.0001$; Fig 3g). Supplementary
191 Table S3 shows longitudinal tau-positive stability (i.e. excluding S0) when excluding individuals using vari-
192 ous subtype probability thresholds.

193 We next examined how SuStaln stage changed over time for each subtype. Across the whole sample,
194 we observed significant yearly increase in SuStaln stage (mean Δ /year = 0.8, $t[148]=6.54$, $p<0.0001$) (Fig
195 3h, Table S4), and a significant difference in mean annual rate of SuStaln stage change was seen across
196 subtypes (details in Supplementary Note 3). The annual SuStaln stage increased faster in S4 (L Temporal)
197 compared to S2 (MTL-Sparing) and S3 (Posterior) subtypes (Fig 3h, Supplementary Note 3). Younger age
198 ($r=-0.22$, $p=0.006$), but not higher baseline SuStaln stage ($r = 0.12$, $p=0.15$), was associated with faster
199 annual change in stage. As a final validation, we used SuStaln to forecast longitudinal rate of regional tau-
200 PET change at the individual level. On average, predictions were significantly better than chance for all
201 subtypes (S1 (Limbic): $t[78]=5.00$, $p<0.0001$; S2 (MTL-Sparing): $t[52]=2.16$, $p=0.035$; S3 (Posterior):
202 $t[45]=3.05$, $p=0.0039$; S4 (L Temporal): $t[29]=4.93$, $p<0.0001$; Fig 3i).

203
204 **Subtype patterns resemble distinct cortico-limbic networks.** Based on our previous work²⁹, we used net-
205 work diffusion models to examine the possibility that the observed subtype-specific tau spreading pat-
206 terns may be driven by spread through distinct networks. We found that an entorhinal cortex epicenter
207 was optimal for the S1 (Limbic) subtype tau pattern and strongly replicated the pattern of tau spreading
208 ($r^2=0.70$), but did not reproduce other subtype patterns nearly as well (S2: $r^2=0.04$; S3: $r^2=0.41$; S4:
209 $r^2=0.37$). Models using different epicenters substantially improved fit for these others subtypes (Fig
210 4a,b,e): best fitting models used the middle temporal gyrus ($r^2=0.27$) for S2 (MTL-Sparing), the fusiform
211 gyrus ($r^2=0.59$) for S3 (Posterior) and the inferior temporal gyrus ($r^2=0.50$) for S4 (L Temporal) (Fig 4c),
212 suggesting a possible predominance of these regions in secondary tau seeding for different subtypes.
213 Highly similar results were found using a different brain atlas and different connectivity data (Extended
214 Data Fig. S10). We further tracked how the best-fitting epicenter changed at higher disease stages, per-
215 haps reflecting participation of different regions as secondary seeding points with advancing disease pro-
216 gression (Fig 4d). All but the S2 (MTL-Sparing)_subtype exhibited MTL spreading in earlier stages, whereas
217 early stages of S2 involved parietal spread. Later stages involved secondary seeding in the temporal lobes,
218 as well as subtype-specific regions. Together, these results suggest that distinct tau patterns across differ-
219 ent subtypes may be driven in part by vulnerability of, or selective spread through, distinct temporal lobe
220 networks.

221 222 **Discussion**

223 For the last thirty years, the progression of tau pathology in AD has principally been described by a single
224 model of spatiotemporal evolution^{8,9}, despite frequent examples of nonconforming cases¹². We show that
225 the cortical cascade of tau pathology is better described by a data-driven model including multiple spatio-
226 temporal patterns (Fig. 5). Importantly, our findings may reconcile atypical AD variants with common vari-
227 ations of typical AD into a single unified model of pathological progression. First, the model reaffirms the
228 existence of observed cortical-predominant and limbic-predominant pathological patterns as distinct sub-
229 types of tau progression, rather than phases along a continuum. In addition, the model also accounts for
230 the most frequently occurring atypical clinical variants of AD, PCA and lvPPA, as the extremes of regularly
231 occurring posterior and lateral-temporal AD subtypes. Together, our data align with a recent model¹⁴ to
232 suggest variation in the pathological expression of AD along two orthogonal axes: subtype and severity,
233 the latter of which is strongly and inversely correlated with age (Fig 5). Given that no dominant pattern
234 emerged, our data suggest the existence of multiple common AD subtypes, challenging the notion that
235 there is such a pathological entity that can be described as "typical" AD. Rather, the spatial pattern of tau
236 spreading appears to vary along at least four archetypes, depending on factors such as age and genotype.
237 Therefore, we propose heterogeneity in AD is best represented as a quadrilateral axis (Fig 5).

238 Our results are robust across datasets and radiotracers. We found individuals representing each
239 of four subtype patterns in each of the five contributing cohorts, and we reproduced a very similar set of
240 subtypes in a totally separate sample using a different radiotracer. Further, most individuals were confi-
241 dently assigned into one subtype pattern, which was consistent over time. The limbic subtype was the
242 most frequent, and presented with many characteristics typically associated with AD, including a greater
243 proportion of *APOE4* carriers, a strongly amnesic phenotype, and medial temporal pathology with a
244 Braak-like progression of tau spread. However, this subtype represented only a third of all tau-positive
245 cases in our dataset (though the earliest stages of three of the four subtypes featured prominent MTL
246 binding, Fig 4d). Our data suggest instead that, at older onset ages or earlier disease stages, the subtypes
247 may present with subtle differences that may be difficult to detect in the clinic, while at younger onset
248 ages or later stages, the more aggressive phenotype can amplify the distinct subtype expressions. The
249 existence of these phenotypes, if further validated, may necessitate a reform in pathological tau staging,
250 where key regions are surveyed to increase sensitivity to detect subtype-specific patterns.

251 Many pioneering studies have noted variation in AD pathology. For example, limbic-predominant
252 and MTL-sparing phenotypes are contrasted against "typical" phenotypes that express tau pathology in

253 both the MTL and neocortex^{12,13}. In contrast to this notion, we found a subtype of individuals expressing
254 both cortical and MTL tau exhibiting a more aggressive phenotype with marked lateralization, the latter
255 being a feature that has not been well characterized in histopathological studies of AD, which typically
256 assess only one hemisphere. In addition, our model allows the concurrence of MTL and cortical pathology
257 at later stages of several distinct progressions, perhaps suggesting that solely contrasting cortical and MTL
258 tau (e.g. ^{21,22}) may not be sufficient to describe AD heterogeneity. Indeed, while some spatial convergence
259 could be observed in our AD subtypes, particularly at early or late stages, subtle regional variation con-
260 sistentlly distinguishes individuals of one subtype from another.

261 We reproduce previous reports describing a strong negative correlation between age and tau pro-
262 gression³⁰⁻³⁴, as well as previous reports that a younger age of onset of AD is associated with a more rapid
263 progression of tau pathology^{35,36}. Interestingly, in our study, this phenomenon was observable across all
264 subtypes (Fig 3b). Previous work has noted that early-onset AD (EOAD) is more likely to present with an
265 atypical (i.e. nonamnestic) phenotype³⁷. This may be a specific characteristic of EOAD. However, ours and
266 others studies^{26,38,39} suggest that posterior or left-lateralized temporal binding are not uncommon across
267 the age spectrum, but our data suggest that the phenotype is more pronounced at earlier ages. There-
268 fore, atypical variants of AD may represent an accelerated and intensified manifestation of common AD
269 subtypes, though this will require further validation.

270 Our findings complement other supervised and unsupervised AD subtyping studies from the imaging
271 and pathology literature^{12-14,21,22,26,38}, though our analysis also produced some novel findings worth fur-
272 ther investigation. Despite the extreme of the posterior subtype being represented by PCA, an aggressive
273 disease variant, the posterior subtype overall demonstrated slower cognitive decline compared to all oth-
274 er subtypes. These individuals exhibited considerable tau pathology in posterior (including occipital) brain
275 regions, but also relatively less MTL and frontal binding. These findings, however, are in agreement with
276 pathology literature describing common variation in occipital tau pathology in both preclinical and symp-
277 tomatic AD^{2,40-42}. These studies, variously surveying Brodmann areas 17, 18 and 19, find evidence for oc-
278 cipital lobe tau in 24-52% of sampled brains, including in cognitively normal individuals. Our study sug-
279 gests this population variation may indeed be systematic, and could be associated with a specific progres-
280 sion pattern. However, tau in the occipital lobe remains understudied, and future studies will be neces-
281 sary to validate the precise characteristics of this posterior subtype. It is still unclear if the posterior sub-
282 type is related to PCA beyond a shared predominance of posterior tau, though it may at least signify the
283 existence of a posterior cortical network selectively vulnerable to tau pathology.

284 Different manifestations of AD may represent subtle variations in the spread of pathology, or could
285 signal the influence of highly distinct processes relevant to treatment intervention. For example, a recent
286 pathology study found increased NFT pathology and neuronal loss in the cholinergic basal forebrain spe-
287 cifically in patients with a MTL-sparing phenotype, and that earlier disease onset was associated with
288 more NFT pathology in these subjects⁴³. Furthermore, another recent study indicated that a targeted ba-
289 sal forebrain treatment could be most effective for patients with a MTL-sparing phenotype⁴⁴. This re-
290 search may suggest a unique role of the basal forebrain in certain subtypes of AD. Meanwhile, APOE has
291 been consistently associated with limbic manifestations of AD^{12,34}, including the present study, and APOE
292 or hippocampus-focused therapies could prove more effective for these individuals. Together, these re-
293 sults point to the possibility that clinical trials may benefit from stratification or enrichment based on AD
294 subtype, or as a first step, post-hoc identification of within-subtype effects.

295 There are currently very few explanations as to why subtypes of AD manifest. Fascinating work has
296 found PCA and lvPPA patients are more likely to exhibit learning disabilities in childhood^{45,46}, perhaps me-
297 diated by abnormalities during brain development⁴⁷. While lvPPA and PCA may represent extremes along
298 the AD continua (as indicated by the present results), this points to the possibility that distinct subtypes
299 may be influenced by variation in cognitive development or other premorbid factors. Another possible
300 explanation for subtypes is interactions between post-translational tau modification and synaptic tau
301 spreading. Several studies have shown that the regional pattern of pathological tau expression in mice is
302 dependent on conformation and injection site of tau seeds^{35,48,49}. It is therefore possible that subtypes of
303 tau spread may simply be dictated by distinct tau conformations and/or systematic variation in the human

304 connectome, perhaps at key synaptic junctures. Supporting the latter hypothesis, we found the tau-PET
305 pattern of AD subtypes resembled macroscale neuronal networks seeded from different brain regions.
306 These findings do not presuppose tau pathology necessarily starts in different regions, but instead that
307 different regions may play a more prominent role in tau propagation across subtypes as "amplifying
308 nodes". This could be mediated by involvement of distinct neuronal cell subtypes⁵⁰, which may incur dis-
309 rupted development due to environmental or genetic factors, leading to network abnormality during life
310 and network vulnerability in late life.

311 This study has a number of limitations. The SuStaln method fits data based on the assumption that
312 several discrete sequences are represented within the data, and it uses cross-sectional information to
313 create pseudo-longitudinal sequences. This framework is based off of the same logic as most pathological
314 staging schema (e.g. ⁸) and hypotheses of biomarker trajectories (e.g. ⁵), but does so in an automated
315 fashion. It is therefore possible that a SuStaln subtype trajectory could be created by "appending" or
316 "stitching" unrelated disease states together. However, we did find most individuals to remain the same
317 subtype at longitudinal follow up, and we could predict regional individual tau accumulation greater than
318 chance using just the SuStaln model. While the use of tau-PET imaging is a great improvement over using
319 MRI to measure AD pathology, there is still some discrepancy between tau-PET signal and true tau pa-
320 thology⁵¹. While flortaucipir binds to paired-helical filament tau, off-target binding is an issue with flor-
321 taucipir, particularly in the striatum, white matter and choroid plexus⁵². We mitigated this issue by regres-
322 sion of choroid plexus signal, exclusion of subcortical ROIs and non-AD dementia patients, and region-
323 specific normalization against non-specific binding, as well as replication with RO948 which exhibits less
324 off-target binding⁵³. Similarly, recent reports question whether elevated flortaucipir binding is detectable
325 before advanced stages of tau accumulation⁵⁴⁻⁵⁶. However, SuStaln's modeling is based on relative re-
326 gional differences in pathology, and regional variation in tau-PET and tau pathology are correlated⁵⁵⁻⁵⁷.
327 Still, while the unbiased spatial sampling of tau-PET data across the brain aided our discovery of these
328 subtype patterns, they must still be validated using histopathology studies. Sample size was an obvious
329 strength of our study, but it comes with the caveat of mixing data from multiple cohorts, scanners, and
330 cognitive batteries. We addressed this issue somewhat by examining subtypes in each cohort separately,
331 replicating our results in a separate sample and adjusting for cohort in our comparisons. In addition, de-
332 spite our study boasting the largest tau-PET sample to date, even larger samples would be preferable in
333 order to elucidate the spatiotemporal progression of each subtype in more detail. We arrived at a four-
334 subtype solution to describe our data using established statistical methodology to identify a solution the
335 data supports with confidence. However, this does not preclude the possibility that other, more subtly
336 distinct subtypes exist (Extended Data Fig. S1f).

337 In conclusion, we describe four distinct but stable spatiotemporal phenotypes of tau accumulation
338 in AD. These subtypes exhibit differing clinical profiles and longitudinal outcomes, and their tau patterns
339 resemble distinct temporal lobe networks. Our data-driven results call into question whether "typical AD"
340 is a quantifiable entity, rather suggesting that several AD subtypes exist, and that their individual differ-
341 ences are exacerbated by more aggressive phenotypes with younger onset ages. Future studies should
342 seek to validate the existence and temporal evolution of these subtypes, as well as identify genetic, cellu-
343 lar and developmental factors that may influence their expression. This may include identifying differ-
344 ences in brain activity and connectivity between individuals, as well as differences in regional vulnerabil-
345 ity. This framework may also be useful for enrichment of clinical trials, for providing more individualized
346 clinical care, and eventually for more individualized treatment.

347
348

349 **Acknowledgements**

350 The authors would like to acknowledge Drs. Mallar Chakravarty, Bratislav Mistic, Pierre Bellec, Pedro Rosa-Neto,
351 Alain Dagher, Edith Hamel and William Seeley for feedback during the composition of this manuscript. JWV
352 acknowledges support from the government of Canada through a tri-council Vanier Canada Graduate Doctoral
353 fellowship, from the McGill Centre for Integrative Neuroscience and the Healthy Brains, Healthy Lives initiative,

354 and by the NIH (T32MH019112). ALY is supported by an MRC Skills Development Fellowship. NPO is a UKRI Future
355 Leaders Fellow (MR/S03546X/1). NPO and DCA acknowledge support from the UK National Institute for Health
356 Research University College London Hospitals Biomedical Research Centre, and DCA acknowledges support from
357 EPSRC grant EP/M020533/1. MJG is supported by the "Miguel Servet" program [CP19/00031] and a research grant
358 [PI20/00613] of the Instituto de Salud Carlos III-Fondo Europeo de Desarrollo Regional (ISCIII-FEDER). Author RL
359 acknowledges support from the NIH (K99AG065501). This project has received funding from the European Union's
360 Horizon 2020 research and innovation programme under grant agreement No. 666992. The BioFINDER studies are
361 supported by the Swedish Research Council (2016-00906), the Knut and Alice Wallenberg foundation (2017-0383),
362 the Marianne and Marcus Wallenberg foundation (2015.0125), the Strategic Research Area MultiPark (Multidisci-
363 plinary Research in Parkinson's disease) at Lund University, the Swedish Alzheimer Foundation (AF-939932), the
364 Swedish Brain Foundation (FO2019-0326), The Parkinson foundation of Sweden (1280/20), the Skåne University
365 Hospital Foundation (2020-0000028), Regionalt Forskningsstöd (2020-0314) and the Swedish federal government
366 under the ALF agreement (2018-Projekt0279). The Tau PET study in Gangnam Severance Hospital was supported
367 by a grant from Basic Science Research Program through the National Research Foundation of Korea (NRF) funded
368 by the Ministry of Education (NRF2018R1D1A1B07049386 & NRF2020R1F1A1076154) and a grant of the Korea
369 Health Technology R&D Project through the Korea Health Industry Development Institute (KHIDI) funded by the
370 Ministry of Health & Welfare, Republic of Korea (Grant number: HI18C1159). We would additionally like to thank
371 Bruce Miller, Howie Rosen, Marilu Gorno Tempini and Bill Jagust for supporting the UCSF tau-PET studies, which
372 were funded through the following sources: NIA R01 AG045611 (Rabinovici), P50 AG23501 (Miller, Rosen, Rabinov-
373 vici), P01 AG019724 (Miller, Rosen, Rabinovici). The precursor of 18F-flortaucipir was provided by AVID radiophar-
374 maceuticals. The precursor of 18F-flutemetamol was sponsored by GE Healthcare. The precursor of 18F-RO948
375 was provided by Roche. Data collection and sharing for this project was funded by the Alzheimer's Disease Neu-
376 roimaging Initiative (ADNI) (National Institutes of Health Grant U01 AG024904) and DOD ADNI (Department of De-
377 fense award number W81XWH-12-2-0012). ADNI is funded by the National Institute on Aging, the National Insti-
378 tute of Biomedical Imaging and Bioengineering, and through generous contributions from the following: AbbVie,
379 Alzheimer's Association; Alzheimer's Drug Discovery Foundation; Araclon Biotech; BioClinica, Inc.; Biogen; Bristol-
380 Myers Squibb Company; CereSpir, Inc.; Cogstate; Eisai Inc.; Elan Pharmaceuticals, Inc.; Eli Lilly and Company; Euro-
381 Immun; F. Hoffmann-La Roche Ltd and its affiliated company Genentech, Inc.; Fujirebio; GE Healthcare; IXICO
382 Ltd.; Janssen Alzheimer Immunotherapy Research Development, LLC.; Johnson Johnson Pharmaceutical Research
383 Development LLC.; Lumosity; Lundbeck; Merck Co., Inc.; Meso Scale Diagnostics, LLC.; NeuroRx Research; Neuro-
384 track Technologies; Novartis Pharmaceuticals Corporation; Pfizer Inc.; Piramal Imaging; Servier; Takeda Pharma-
385 ceutical Company; and Transition Therapeutics. The Canadian Institutes of Health Research is providing funds to
386 support ADNI clinical sites in Canada. Private sector contributions are facilitated by the Foundation for the National
387 Institutes of Health (www.fnih.org). The grantee organization is the Northern California Institute for Research and
388 Education, and the study is coordinated by the Alzheimer's Therapeutic Research Institute at the University of
389 Southern California. ADNI data are disseminated by the Laboratory for Neuro Imaging at the University of Southern
390 California. Finally, we would like to all participants of this study, and families and care-givers of included patients,
391 for their support in volunteering data for this study.

392 393 **Author Contributions**

394 JWV, OH & ACE conceptualized the work. JWV, ALY, NPO, LMA, MJP & OH contributed to analytic design.
395 MJP, MDD, GDR, CHL & OH acquired and provided the data. RS, RO, OTS & RLJ contributed to data cura-
396 tion and processing. JWV analyzed the data. ALY & DCA originally created the SuStaln algorithm, and NPO
397 & LMA contributed to its execution. YIM created the ESM algorithm. JWV & OH drafted the manuscript.
398 All authors interpreted the data and substantively contributed to revising the manuscript.

399 400 **Competing interests**

401 MJP and MDD are employees of Avid Radiopharmaceuticals, a wholly owned subsidiary of Eli Lilly and
402 Company and are minor stockholders in Eli Lilly. OH has acquired research support (for the institution)

403 from AVID Radiopharmaceuticals, Biogen, Eli Lilly, Eisai, GE Healthcare, Pfizer, and Roche. In the past 2
404 years, he has received consultancy/speaker fees from AC Immune, Alzpath, Biogen, Cerveau and Roche.
405 The remaining authors declare no competing interests.

406
407

408 **Data Availability statement**

409 Tau-PET data contributing to this study was sourced from six different cohorts. One of them, ADNI, is a
410 public access dataset and can be obtained through an application at <http://adni.loni.usc.edu/>. Data from
411 the other datasets are not publicly available for download, but access requests can be made to the re-
412 spective study Investigators: BioFINDER 1,2 – Oskar Hansson; UCSF Memory and Aging Center – Gil D
413 Rabinovici; Gangnam Severence Hospital, Seoul – Chul Hyoung Lyoo; AVID Radiopharmaceuticals – Mi-
414 chael J Pontecorvo, Michael D Devous. Additionally, CMU60 DTI data used to create template DTI connec-
415 tomes are publicly available, and can be accessed at
416 <https://www.cmu.edu/dietrich/psychology/cognitiveaxon/data.html>.

417

418 **Code Availability statement**

419 Python and MatLab implementations of the SuStain algorithm are available on the UCL-POND github
420 page: <https://github.com/ucl-pond>. The ESM algorithm is available for academics as part of an open-
421 access, user-friendly software (for further details, visit <https://www.neuropm-lab.com/>).

422

423 **References**

424

- 425 1. Hurd, M. D., Martorell, P., Delavande, A., Mullen, K. J. & Langa, K. M. Monetary Costs of Dementia in the
426 United States. *N. Engl. J. Med.* **368**, 1326–1334 (2013).
- 427 2. Alafuzoff, I. *et al.* Staging of Neurofibrillary Pathology in Alzheimer’s Disease: A Study of the BrainNet Eu-
428 rope Consortium. *Brain Pathol.* **0**, 080509082911413-??? (2008).
- 429 3. Hyman, B. T. *et al.* National Institute on Aging-Alzheimer’s Association guidelines for the neuropathologic
430 assessment of Alzheimer’s disease. *Alzheimer’s Dement.* **8**, 1–13 (2012).
- 431 4. Hardy, J. & Selkoe, D. J. The Amyloid Hypothesis of Alzheimer’s Disease: Progress and Problems on the
432 Road to Therapeutics. *Science (80-.)*. **297**, 353–356 (2002).
- 433 5. Jack, C. R. *et al.* Tracking pathophysiological processes in Alzheimer’s disease: An updated hypothetical
434 model of dynamic biomarkers. *Lancet Neurol.* **12**, 207–216 (2013).
- 435 6. La Joie, R. *et al.* Prospective longitudinal atrophy in Alzheimer’s disease correlates with the intensity and
436 topography of baseline tau-PET. *Sci. Transl. Med.* **12**, 1–13 (2020).
- 437 7. Bejanin, A. *et al.* Tau pathology and neurodegeneration contribute to cognitive impairment in Alzheimer ’ s
438 disease. 1–15 (2017) doi:10.1093/brain/awx243.
- 439 8. Braak, H. & Braak, E. Neuropathological staging of Alzheimer-related changes. *Acta Neuropathol.* **82**, 239–
440 59 (1991).
- 441 9. Braak, H., Alafuzoff, I., Arzberger, T., Kretschmar, H. & Tredici, K. Staging of Alzheimer disease-associated
442 neurofibrillary pathology using paraffin sections and immunocytochemistry. *Acta Neuropathol.* **112**, 389–
443 404 (2006).
- 444 10. Schöll, M. *et al.* PET Imaging of Tau Deposition in the Aging Human Brain. *Neuron* (2016)
445 doi:10.1016/j.neuron.2016.01.028.
- 446 11. Schwarz, A. J. *et al.* Regional profiles of the candidate tau PET ligand ¹⁸F-AV-1451 recapitulate key features
447 of Braak histopathological stages. *Brain* aww023 (2016) doi:10.1093/brain/aww023.
- 448 12. Murray, M. E. *et al.* Neuropathologically defined subtypes of Alzheimer’s disease with distinct clinical char-
449 acteristics: A retrospective study. *Lancet Neurol.* **10**, 785–796 (2011).
- 450 13. Whitwell, J. L. *et al.* Neuroimaging correlates of pathologically defined subtypes of Alzheimer’s disease: A

- 451 case-control study. *Lancet Neurol.* **11**, 868–877 (2012).
- 452 14. Ferreira, D., Nordberg, A. & Westman, E. Biological subtypes of Alzheimer’s disease: a systematic review
453 and meta-analysis. *Neurology* **0**, under-review (2020).
- 454 15. Ossenkoppele, R. *et al.* Tau PET patterns mirror clinical and neuroanatomical variability in Alzheimer’s dis-
455 ease. *Brain* **139**, 1551–1567 (2016).
- 456 16. Crutch, S. J. *et al.* Consensus classification of posterior cortical atrophy. *Alzheimer’s Dement.* **13**, 870–884
457 (2017).
- 458 17. Gorno-Tempini, M. L. *et al.* Classification of primary progressive aphasia and its variants. *Neurology* **76**,
459 1006–1014 (2011).
- 460 18. Ossenkoppele, R. *et al.* The behavioural/dysexecutive variant of Alzheimer’s disease: Clinical, neuroimaging
461 and pathological features. *Brain* **138**, 2732–2749 (2015).
- 462 19. Drummond, E. *et al.* Proteomic differences in amyloid plaques in rapidly progressive and sporadic Alz-
463 heimer’s disease. *Acta Neuropathol.* **133**, 933–954 (2017).
- 464 20. Crist, A. M. *et al.* Leveraging selective hippocampal vulnerability among Alzheimer’s disease subtypes re-
465 veals a novel tau binding partner SERPINA5. *bioRxiv* 2020.12.18.423469 (2020)
466 doi:10.1101/2020.12.18.423469.
- 467 21. Risacher, S. L. *et al.* Alzheimer disease brain atrophy subtypes are associated with cognition and rate of
468 decline. *Neurology* **89**, 2176–2186 (2017).
- 469 22. Ossenkoppele, R. *et al.* Distinct tau PET patterns in atrophy-defined subtypes of Alzheimer’s disease.
470 *Alzheimer’s Dement.* **16**, 335–344 (2020).
- 471 23. Young, A. L. *et al.* Uncovering the heterogeneity and temporal complexity of neurodegenerative diseases
472 with Subtype and Stage Inference. *Nat. Commun.* **9**, 4273 (2018).
- 473 24. Dong, A. *et al.* Heterogeneity of neuroanatomical patterns in prodromal Alzheimer’s disease: links to cogni-
474 tion, progression and biomarkers. *Brain* **140**, 735–747 (2017).
- 475 25. Noh, Y. *et al.* Anatomical heterogeneity of Alzheimer disease: based on cortical thickness on MRIs. *Neurol-*
476 *ogy* **83**, 1936–44 (2014).
- 477 26. Tam, A. *et al.* A highly predictive signature of cognition and brain atrophy for progression to Alzheimer’s
478 dementia. *Gigascience* **8**, 1–16 (2019).
- 479 27. Vogel, J. W. *et al.* Data-driven approaches for tau-PET imaging biomarkers in Alzheimer’s disease. *Hum.*
480 *Brain Mapp.* **40**, 638–651 (2019).
- 481 28. Leuzy, A. *et al.* Diagnostic Performance of RO948 F 18 Tau Positron Emission Tomography in the Differenti-
482 ation of Alzheimer Disease from Other Neurodegenerative Disorders. *JAMA Neurol.* 1–12 (2020)
483 doi:10.1001/jamaneurol.2020.0989.
- 484 29. Vogel, J. W. *et al.* Spread of pathological tau proteins through communicating neurons in human Alz-
485 heimer’s disease. *Nat. Commun.* **11**, 2612 (2020).
- 486 30. Marshall, G. A., Fairbanks, L. A., Tekin, S., Vinters, H. V. & Cummings, J. L. Early-onset Alzheimer’s disease is
487 associated with greater pathologic burden. *J. Geriatr. Psychiatry Neurol.* **20**, 29–33 (2007).
- 488 31. Whitwell, J. L. *et al.* The role of age on tau PET uptake and gray matter atrophy in atypical Alzheimer’s dis-
489 ease. *Alzheimer’s Dement.* **15**, 675–685 (2019).
- 490 32. Pontecorvo, M. J. *et al.* A multicentre longitudinal study of flortaucipir (18F) in normal ageing, mild cogni-
491 tive impairment and Alzheimer’s disease dementia. *Brain* **142**, 1723–1735 (2019).
- 492 33. Jack, C. R. *et al.* Predicting future rates of tau accumulation on PET. *Brain* **143**, 3136–3150 (2020).
- 493 34. La Joie, R. *et al.* Association of APOE4 and clinical variability in Alzheimer disease with the pattern of tau-
494 and amyloid-PET. *Neurology* 10.1212/WNL.0000000000011270 (2020)
495 doi:10.1212/wnl.0000000000011270.

- 496 35. Dujardin, S. *et al.* Tau molecular diversity contributes to clinical heterogeneity in Alzheimer's disease. *Nat.*
497 *Med.* (2020) doi:10.1038/s41591-020-0938-9.
- 498 36. Aoyagi, A. *et al.* A β and tau prion-like activities decline with longevity in the Alzheimer's disease human
499 brain. *Sci. Transl. Med.* **11**, 1–14 (2019).
- 500 37. Koedam, E. L. G. E. *et al.* Early-Versus Late-Onset Alzheimer's Disease: More than Age Alone. *J. Alzheimer's*
501 *Dis.* **19**, 1401–1408 (2010).
- 502 38. Sun, N., Mormino, E. C., Chen, J., Sabuncu, M. R. & Yeo, B. T. T. Multi-modal latent factor exploration of
503 atrophy, cognitive and tau heterogeneity in Alzheimer's disease. *Neuroimage* **201**, (2019).
- 504 39. Franzmeier, N. *et al.* Patient-centered connectivity-based prediction of tau pathology spread in Alzheimer's
505 disease. *Sci. Adv.* **6**, eabd1327 (2020).
- 506 40. Mukaetova-Ladinska, E. B. *et al.* Regional Distribution of Paired Helical Filaments and Normal Tau Proteins
507 in Aging and in Alzheimer's Disease with and without Occipital Lobe Involvement. *Dement. Geriatr. Cogn.*
508 *Disord.* **3**, 61–69 (1992).
- 509 41. McKee, A. C. *et al.* Visual Association Pathology in Preclinical Alzheimer Disease. *J. Neuropathol. Exp.*
510 *Neurol.* **65**, 621–630 (2006).
- 511 42. Pikkarainen, M., Kauppinen, T. & Alafuzoff, I. Hyperphosphorylated Tau in the Occipital Cortex in Aged
512 Nondemented Subjects. *J. Neuropathol. Exp. Neurol.* **68**, 653–660 (2009).
- 513 43. Hanna Al-Shaikh, F. S. *et al.* Selective Vulnerability of the Nucleus Basalis of Meynert among Neuropathologic
514 Subtypes of Alzheimer Disease. *JAMA Neurol.* **32224**, 225–233 (2019).
- 515 44. Machado, A. *et al.* The cholinergic system in subtypes of Alzheimer's disease: an in vivo longitudinal MRI
516 study. *Alzheimers. Res. Ther.* **12**, 51 (2020).
- 517 45. Rogalski, E., Johnson, N., Weintraub, S. & Mesulam, M. Increased Frequency of Learning Disability in Pa-
518 tients With Primary Progressive Aphasia and Their First-Degree Relatives. *Arch. Neurol.* **65**, 1–7 (2008).
- 519 46. Ossenkoppele, R. *et al.* Discriminative accuracy of [18F]flortaucipir positron emission tomography for Al-
520zheimer disease vs other neurodegenerative disorders. *JAMA - J. Am. Med. Assoc.* **320**, 1151–1162 (2018).
- 521 47. Miller, Z. A. *et al.* Cortical developmental abnormalities in logopenic variant primary progressive aphasia
522 with dyslexia. *Brain Commun.* 1–8 (2019) doi:10.1093/braincomms/fcz027.
- 523 48. Hyman, B. T. Tau propagation, different tau phenotypes, and prion-like properties of tau. *Neuron* **82**, 1189–
524 1190 (2014).
- 525 49. He, Z. *et al.* Transmission of tauopathy strains is independent of their isoform composition. *Nat. Commun.*
526 **11**, (2020).
- 527 50. Leng, K. *et al.* Molecular characterization of selectively vulnerable neurons in Alzheimer's Disease. (2020).
- 528 51. Lemoine, L., Leuzy, A., Chiotis, K., Rodriguez-Vieitez, E. & Nordberg, A. Tau positron emission tomography
529 imaging in tauopathies: The added hurdle of off-target binding. *Alzheimer's Dement. Diagnosis, Assess. Dis.*
530 *Monit.* **10**, 232–236 (2018).
- 531 52. Baker, S. L., Harrison, T. M., Maaß, A., La Joie, R. & Jagust, W. Effect of off-target binding on 18 F-
532 Flortaucipir variability in healthy controls across the lifespan . *J. Nucl. Med.* jnumed.118.224113 (2019)
533 doi:10.2967/jnumed.118.224113.
- 534 53. Smith, R. *et al.* Head-to-head comparison of tau positron emission tomography tracers [18F]flortaucipir
535 and [18F]RO948. *Eur. J. Nucl. Med. Mol. Imaging* **47**, 342–354 (2020).
- 536 54. Fleisher, A. S. *et al.* Positron Emission Tomography Imaging with [18F]flortaucipir and Postmortem Assess-
537-ment of Alzheimer Disease Neuropathologic Changes. *JAMA Neurol.* **77**, 829–839 (2020).
- 538 55. Lowe, V. J. *et al.* Tau-positron emission tomography correlates with neuropathology findings. *Alzheimer's*
539 *Dement.* **16**, 561–571 (2020).
- 540 56. Soleimani-Meigooni, D. N. *et al.* 18F-flortaucipir PET to autopsy comparisons in Alzheimer's disease and
541 other neurodegenerative diseases. *Brain* **143**, (2020).
- 542 57. Smith, R., Wibom, M., Pawlik, D., Englund, E. & Hansson, O. Correlation of in Vivo [18 F]Flortaucipir with
543 Postmortem Alzheimer Disease Tau Pathology. *JAMA Neurol.* **76**, 310–317 (2019).

544
545
546
547
548
549
550
551
552
553
554
555
556
557
558
559
560
561
562
563
564
565
566
567
568
569
570
571
572
573
574
575
576
577
578
579
580
581
582
583
584
585
586
587
588
589
590
591
592
593
594

Figure Legends

Figure 1

Spatiotemporal subtypes of tau progression. A) Tau-PET pattern of tau-positive (subtyped) individuals. B) Quarterly plot showing probability each individual is classified as each subtype. Dots are labeled by final subtype classification: S1 (blue), S2 (green), S3 (orange) or S4 (pink). Inset box shows individuals that had a probability < 0.5 to be classified as any of the four subtypes (i.e. showing poor fit). C) Average tau-PET pattern for each subtype. The colorbar is the same as Panel A. D) Regions showing significant difference between one subtype and all other subtypes using OLS linear models adjusting for SuStaln stage, after FDR correction. E) Progression of each subtype through SuStaln stages. Each image is a mean of individuals classified at the listed stage and up to four stages lower. Only the left hemisphere is shown.

Figure 2

Subtype stability: AD spatiotemporal subtypes replicate in another cohort using a different PET tracer. A) For both the discovery (Orig) and replication (Repl) cohorts, maps showing regions significantly different between one subtype and all others (excluding S0) within the cohort (after FDR correction). Similar spatial patterns were observed, except for a reversed pattern in S4. B) Confusion matrix comparing subtypes identified in the original (discovery) sample (y-axis), and subtypes separately identified in the replication sample (x-axis). Values represent spatial correlation between average regional tau for each subtype. Values along the diagonal indicates similarity between the same subtype across both cohorts.

Figure 3

Progression of AD subtypes. Increasing SuStaln stage is associated with lower age a) and worse cognition b) across all subtypes. c) Rate of longitudinal decline in MMSE for each subtype. The x-axis was jittered for visualization purposes only. The y-axis shows MMSE across all observations as predicted by linear mixed models adjusted for covariates. d) Boxplots showing the distribution of predicted MMSE slopes for each subtype, stratified by clinical diagnosis (stats in Supplementary Table S2). e) Cross-cohort meta-analysis for the effects of S4: L Temporal declining faster (left) and S3: Posterior declining slower (right) than other subtypes, respectively. Diamonds represent effect sizes, while diamond size reflects relative sample size. Red diamonds indicate significant effects. Error bars = SEM. f) Confusion matrix showing longitudinal stability of subtypes. Each row shows the number of subjects from a given subtype at Visit 1 that were classified as each subtype at Visit 2. The diagonal represents the number of subjects that were classified as the same subtype at Visit 1 and Visit 2. g) Individuals with a higher probability of being classified into their subtype at baseline were more likely to show a stable subtype over time (two-sided $t[156,53]=5.26, p=3.6e-07$). h) Annual change in SuStaln stage for each subtype, in individuals with stable subtypes over time (stats in Supplementary Note 3). i) SuStaln was used to predict longitudinal change in regional tau accumulation. Each dot represents a subject, and the y-axis represents the spatial correlation between the true regional tau change and the predicted regional tau change. Average predictions were significantly greater than chance based on a two-tailed, one-sample t-test against 0 (S1: $t[78]=5.00, p=3.5e-06$; S2: $t[52]=2.16, p=0.035$; S3: $t[45]=3.05, p=0.0039$; S4: $t[29]=4.93, p=3.1e-05$). * $p(\text{unc.}) < 0.05$, *** $p(\text{unc.}) < 0.001$. Error bars in a-c represent 95% CI of model fit across 1000 bootstrap samples. For boxplots in d, g-i, center line=median, box=inner quartiles, whiskers=extent of data distribution except *=outliers

Figure 4

Application of epidemic spreading model to determine subtype-specific corticolimbic circuit vulnerability. An epidemic spreading model was fit separately for each subtype; once using an entorhinal cortex epicenter (a, blue), and once with a subtype-specific best-fitting epicenter (b, red). For each plot, each dot represents a region. The x-axis represents the mean simulated tau-positive probabilities across the population, while the y-axis represents the mean observed tau-positive probability. Each row represents a subtype. Error bars in a-c represent 95% CI of model fit across 1000 bootstrap samples. c) For each subtype, the probability that each region is the best fitting epicen-

595 ter for that subtype, based on bootstrap resampling. d) For each subtype, the proportion of individuals at various
 596 stages that had best-fitting epicenters within each of five major brain divisions: medial temporal lobe (MTL, blue),
 597 temporal lobe (yellow), parietal lobe (purple), occipital lobe (gray) and frontal lobe (turquoise). e) For each subtype,
 598 spatial representation of ESM results from panel B using best-fitting epicenter. From left to right, observed region-
 599 al tau-PET probabilities (tau-P), regional connectivity to best-fitting epicenter (Cx), tau-PET probabilities predicted
 600 by the ESM. These images show the degree to which constrained diffusion of signal through a connectome (Pred.),
 601 starting in a given epicenter and its associated fiber network (Cx.), recapitulates the tau patterns of each subtype
 602 (Obs.).

603
 604 **Figure 5**
 605 A theoretical model summarizing variation in the spread of tau pathology in AD. Tau pathology varies along an axis
 606 of severity (vertical in the diagram), which is inversely associated with onset age. In addition, tau varies along a
 607 spatiotemporal dimension (horizontal plane in the diagram), such that an individual can be described by their fit
 608 along one of at least four trajectories. Text indicates clinical characteristics of each subtypes. Emboldened text re-
 609 flects robust differences between subtypes, while normal text reflects less-robust characteristics that differentiate
 610 subtypes from tau-negative individuals

611
 612
 613
 614
 615
 616
 617
 618
 619
 620
 621
 622
 623 **Table 1**
 624

	S0: No Tau	S1: Limbic	S2: MTL-Sparing	S3: Posterior	S4: L Temporal
n	687	137	73	131	80
Age	71.52 (8.1)	75.28 (7.7)#	71.34 (8.3)*	75.06 (7.3)#	73.41 (6.9)
Prop. Female	0.49	0.70#	0.60‡	0.64#	0.56
Education	15.17 (2.9)	14.42 (3.9)	14.29 (4.0)	14.6 (3.0)	14.82 (2.9)
Prop. APOE4	0.26	0.75#*	0.47*	0.63#	0.59#

Carrier					
Cortical Tau SUVR	1.04 (0.1)	1.41 (0.1)#*	1.44 (0.1)#	1.44 (0.1)#	1.47 (0.1)#*
Laterality	0.0 (0.2)	-0.28 (1.3)*#R	-0.13 (1.6)‡*R	0.04 (1.5)	1.95 (1.2)#*L
MMSE	28.9 (1.5)	24.33 (3.0)#	24.32 (4.2)#	24.19 (3.0)#	23.33 (5.0)#
Global Cognition	0.36 (0.5)	-0.03 (0.8)*	-0.29 (0.8)#	-0.23 (0.8)#	-0.39 (0.9)#†
Abs. Memory	0.48 (0.7)	-0.62 (0.7)#†	-0.36 (0.7)#	-0.55 (0.7)#	-0.3 (0.8)#†
Abs. Language	0.22 (0.7)	-0.11 (0.8)	0.01 (0.9)	-0.18 (0.8)	-0.64 (1.1)#*
Abs. Executive	0.19 (0.6)	0.02 (0.9)	-0.33 (0.9)#	0.03 (0.8)	-0.17 (1.0)‡
Abs. Visuospatial	0.19 (0.6)	0.08 (1.0)	-0.25 (1.2)#	-0.23 (1.2)#	-0.09 (1.0)
Rel. Memory	0.26 (0.8)	-0.61 (1.0)#*	-0.14 (1.0)	-0.37 (1.0)#	-0.06 (1.1)*
Rel. Language	-0.02 (0.8)	0.05 (1.0)	0.31 (1.2)#	0.06 (1.0)	-0.51 (1.3)#*
Rel. Executive	-0.14 (0.8)	0.25 (1.0)‡	-0.22 (1.0)‡*	0.38 (1.1)#	0.22 (1.2)
Rel. Visuospatial	-0.1 (0.7)	0.31 (1.1)‡	0.03 (1.3)	0.0 (1.3)	0.27 (1.3)

625
626
627
628

Table 1 Comparison of means of different variables between subtypes in the discovery sample, after correction for age (except in the case of age), sex (except in the case of sex), education (except in the case of education), cohort, clinical diagnosis (i.e. CN, MCI, AD), and SuStain stage

629 (except comparisons with S0). Standard deviations are given in parentheses where relevant. All p-values were corrected for multiple compari-
630 sons.

631 MMSE = Mini-Mental State Examination; Abs. = Absolute; Rel. = Relative; Prop. = Proportion

632 * = Adj. $p < \$0.05$ (vs all other subtypes, not including S0)

633 † = Adj. $p < \$0.1$ (vs all other subtypes, not including S0)

634 # = Adj. $p < \$0.05$ (vs S0)

635 ‡ = Adj. $p < \$0.1$ (vs S0).

636 R = Significant right-sided laterality in this subtype compared to others

637 L = Significant left-sided laterality in this subtype compared to other subtypes.

638

639

640

641

642

643

644 Online Methods

645 Unless otherwise noted, all data analysis was conducted, and all figures were created, using Python
646 v.3.7.3, mostly using the numpy, scipy, pandas, scikit-learn, nilearn, matplotlib, seaborn and statsmodels
647 libraries.

648

649 **Sample Characteristics.** The total sample for the following analyses comprised of flortaucipir tau-PET scans
650 from 1667 individuals from five different cohorts (BioFINDER I, Seoul, AVID, UCSF, ADNI), and RO948 PET
651 scans from 657 individuals from a sixth cohort (BioFINDER II). Information pertaining to recruitment, diag-
652 nostic criteria and A β positivity assessment for the BioFINDER I (BioF)⁴⁶, ADNI²⁷, AVID³², Seoul⁵⁹, UCSF⁶ and
653 BioFINDER II (BF2)²⁸ cohorts have been previously reported. Informed written consent was provided for all
654 participants or their designated caregiver, and all protocols were approved by each cohort's respective
655 institutional ethical review board. Specifically: All BioFINDER subjects provided written informed consent
656 to participate in the study according to the Declaration of Helsinki; ethical approval was given by the Eth-
657 ics Committee of Lund University, Lund, Sweden, and all methods were carried out in accordance with the
658 approved guidelines. Approval for PET imaging was obtained from the Swedish Medicines and Products
659 Agency and the local Radiation Safety Committee at Skåne University Hospital, Sweden. For UCSF, the
660 study was approved by the University of California (San Francisco and Berkeley) and Lawrence Berkeley
661 National Laboratory institutional review boards for human research. Data from the AVID sample were
662 collected in compliance with the Declaration of Helsinki and the International Conference on Harmoniza-
663 tion guideline on good clinical practice. Data collection for the Gangnam Severance hospital sample was
664 approved by the institutional review board of Gangnam Severance Hospital. Information related to partic-
665 ipant consent in ADNI can be found at (ADNI; <http://adni.loni.usc.edu>). Some of the data used in the
666 preparation of this article were obtained from the Alzheimer's Disease Neuroimaging Initiative (ADNI)
667 database (adni.loni.usc.edu). The ADNI was launched in 2003 as a public-private partnership, led by Prin-
668 cipal Investigator Michael W. Weiner, MD. The primary goal of ADNI has been to test whether serial mag-
669 netic resonance imaging (MRI), positron emission tomography (PET), other biological markers, and clinical
670 and neuropsychological assessment can be combined to measure the progression of mild cognitive im-
671 pairment (MCI) and early Alzheimer's disease (AD). For up-to-date information, see www.adni-info.org.

672 From this total sample of 1667 subjects with flortaucipir scans, a subsample was derived including i)
673 all cognitively unimpaired individuals older than 40 years; and ii) individuals who had both a diagnosis of
674 MCI or AD, *and* imaging or fluid evidence of brain A β pathology. All subjects with a primary diagnosis oth-
675 er than cognitively unimpaired (which included subjective cognitive decline), MCI or AD were excluded.
676 This subsample, used for all subsequent analysis, comprised 1143 individuals. The same screening proce-
677 dures were used to filter individuals from BioFINDER II, reducing the samples size from 657 to 469. Char-
678 acteristics of all samples, including inter-cohort differences, are detailed in Table S1.

679

680 **Image Acquisition and Preprocessing.** Tau-PET data acquisition procedures for each cohort have been pre-
681 viously described^{6,27,28,32,46,59}. All tau-PET data were processed centrally in Lund by analysts blinded to de-
682 mographic and clinical data, in a manner previously described⁴⁶. Briefly, resampling procedures were used
683 to harmonize image size and voxel dimension across sites. Each image underwent motion correction using
684 AFNI's 3dvolreg (<https://afni.nimh.nih.gov/>), and individual PET volumes were averaged within-subject.

685 Each subject's mean PET image next underwent rigid coregistration to it's respective skull-stripped native
686 T1 image, and images were intensity normalized using an inferior cerebellar gray reference region, result-
687 ing in standardized uptake value ratio (SUVR) images. T1 images were processed using Freesurfer v6.0
688 (<https://surfer.nmr.mgh.harvard.edu/>), resulting in native space parcellations of each subject's brain using
689 the Desikan-Killiany (freesurfer) atlas. These parcellations were used to extract mean SUVR values within
690 different regions of interest (ROIs) for each subject in native space.

691
692 **Subtype and Stage Inference.** Typical efforts to perform data-driven subtyping of neuroimages in AD are
693 limited by the confound of disease stage. In a sample spanning the AD spectrum from healthy to dement-
694 ed such as ours, disease progression represents the main source of variation in MR and PET images.
695 Therefore, unless disease stage is somehow accounted for, most clustering algorithms will partition indi-
696 viduals based on their disease stage. This is not useful for parsing heterogeneous patterns related to pro-
697 gression subtypes, which are theoretically orthogonal to disease progression itself. The Subtype and Stage
698 Inference (SuStaln)²³ algorithm surmounts this limitation by combining clustering with disease progression
699 modeling. Detailed formalization of SuStaln has been published previously²³.

700 SuStaln models linear transition across discrete points along a progression of indices of severity (typ-
701 ically z-scores), separately across different ROIs (Fig. S1a). Input requires a subject x feature matrix where,
702 in this case, features represent mean tau-PET signal within different ROIs. In addition, "severity scores",
703 indicating different waypoints along the natural progression of ROI severity, must be provided. Whereas
704 the choice of ROI constrains the spatial dimensions along which individuals may vary, the severity scores
705 instead constrain the temporal dimension of variation. The total number of features is therefore repre-
706 sented by the product of N ROIs by N ROI-specific severity scores. A balance must thus be struck between
707 resolution in the spatial and temporal dimensions, with respect to overall sample size.

708 Our discovery sample boasts scans from 1143 individuals, but even given our inclusion criteria, we
709 expected from previous work²⁹ that the majority of individuals (50-60%) will have minimal tau binding
710 (note that SuStaln will automatically detect these individuals and exclude them from progression model-
711 ing). We therefore expect the modeling to be performed on a sample of closer to N~450-550. We there-
712 fore decided on ten different ROIs (spatial features), each with three severity scores (temporal dimen-
713 sion), totalling 30 features. Given an arbitrary rule of 10-20 observations per feature, 300-600 observa-
714 tions should provide sufficient power, and our sample size should therefore be sufficient.

715 For the ten spatial features, we opted for left and right lobar regions of interest: parietal, frontal,
716 occipital, temporal and medial temporal lobe (MTL). This choice is justified as follows: i) previous imaging
717 and pathology subtyping studies have revealed variation in AD pathology to often occur within specific
718 lobes, e.g. limbic-predominant (MTL), MTL-sparing (parietal), posterior cortical atrophy (occipital), loge-
719 penic aphasia (temporal) and behavioral variant AD (perhaps frontal)¹⁸; ii) hemispheric laterality in AD is
720 understudied, perhaps due to pathological staining often occurring on single hemispheres. However,
721 some laterality has been observed in AD clinical variants (i.e. lvPPA¹⁵) and may point to differing pheno-
722 types in typical AD; iii) These lobar regions maintain some orthogonality to disease progression, as multi-
723 ple lobes are involved in Braak stages IV - VI⁸.

724 To define severity score cutoffs, we first sought to normalize SUVR values to account for regional
725 differences in PET signal (due to nonuniformity of off-target binding, perfusion, etc. across the brain)²⁹.
726 Two-component Gaussian mixture models were used to define, for each ROI, a normal (Gaussian-shaped
727 noise) and abnormal distribution. We then created tau Z-scores by normalizing all values using the mean
728 of the normal distribution (Extended Data Fig. S1b). This procedure centered the Z-score values on the

729 normal distribution to allow for more interpretable values (i.e. $2=2$ SDs from normal), and also accounted
730 for region-specific differences in normal and abnormal SUVR distributions. Uniform values of $Z = 2, 5, 10$
731 were arbitrarily chosen as severity score control points for all ROIs (Extended Data Fig. S1)B. However,
732 analyses were also run with alternative z-score values, see the Replication Analysis section below.

733 The number of subtypes (i.e. distinct spatiotemporal progressions) was determined through cross-
734 validation. Separately for each $k=1-7$ subtypes, 10-fold cross-validation was performed where, for each
735 fold, SuStaln was fit to 90% of the data, and this model was used to evaluate sample likelihood for the
736 10% left-out subjects. For each left-out set, model fit was evaluated using the cross-validation information
737 criterion (CVIC; as described in ²³), as well as out-of-sample log-likelihood. In addition, we used the inner-
738 fold SuStaln model to assign all outer-fold individuals to a subtype, and we evaluated the probability of
739 the maximum-likelihood subtype. In theory, a better fit model should produce more high probability as-
740 signments of left-out data, though more subtypes will also make assignment more challenging. k was cho-
741 sen by evaluating these three metrics in concert (Extended Data Fig. S1c-e). CVIC increased significantly
742 with increasing k , indicating better fit to the data as the number of subtypes increased, though the curve
743 flattened somewhat after $k=4$ (Extended Data Fig. S1c). Similarly, log-likelihood increased indicating better
744 model fit, up until $k=4$, after which no improvement was seen (Extended Data Fig. S1d). In contrast to the-
745 se fit statistics, cross-validated maximum-likelihood subtype probability decreased with increasing k , indi-
746 cating less-confident assignment of left-out data with more subtypes. This decline was steady, though the
747 median probability dropped below 0.5 after $k=4$. Taken together, $k=4$ appeared to be the best solution to
748 maximize model fit but minimize detriment to subtype confidence. We also noted that no subtypes after
749 $k=4$ had more than one "parent" subtype. In other words, solutions 3 and 4 feature subtypes that were
750 composed of multiple parent subtypes, whereas all solutions thereafter featured only subtypes that split
751 off from a single parent subtype. This could be indicative of a certain level of hierarchical convergence at
752 $k=4$ (Extended Data Fig. S1f).

753 Finally, SuStaln was run on the whole sample with the selected $k=4$. Note that for model fitting, SuSt-
754 taln uses a uniform prior on disease subtype and stage (i.e. assumes all subtype and stage combinations
755 equally likely). Note also that the model is initialized with an expectation-maximization algorithm, and
756 therefore does not require a burn-in period.²³ The model was fit using 10000 Markov chain Monte Carlo
757 (MCMC) iterations. SuStaln calculates the probability that each individual falls into each stage of each sub-
758 type, and individuals are assigned to their maximum likelihood subtype and stage. Note that individuals
759 that do not express abnormal tau in any region are classified by SuStaln as "Stage 0", and are not assigned
760 to a subtype. The proportion of individuals classified into each subtype was quantified. We also stratified
761 this quantification by clinical diagnosis, and to cohort to assess the frequency of subtypes in each contrib-
762 uting dataset. Finally, we quantified the proportion of subjects that did not fall well into any subtype (no
763 subtype probability $>50\%$).

764
765 **Post-hoc subtype correction.** Manual inspection of subtype progressions suggested that the early stages of
766 one subtype (S2: MTL-Sparing; see Results) were composed mostly of cognitively normal individuals with
767 abnormally high tau-PET binding throughout the cortex, but little-to-no tau in typical early-mid AD re-
768 gions, i.e. false (tau) positives. Specifically, these individuals showed elevated binding throughout the cor-
769 tex, including sensorimotor and frontal regions (regions where tau typically accumulates only in the latest
770 stages of AD⁸), but had low tau levels in the temporal lobes (Extended Data Fig. S1a). On an individual
771 basis, such individuals showed tau-PET signal that was slightly but globally elevated, with several small
772 "hotspots" distributed diffusely throughout frontal, parietal and occipital cortex. While it is unclear
773 whether this elevated binding represents off-target binding, diffuse low-level target binding, or other
774 methodological issues, consensus among co-authors was that these individuals were not consistent with
775 an AD phenotype. We used Gaussian mixture modeling across all individuals as described in ²⁹ to define
776 the probability of abnormal tau-positivity in each of the left and right entorhinal cortex and precuneus,
777 respectively. We then marked individuals who had $<90\%$ probability of tau in all four regions as low-
778 probability tau individuals (T-). These individuals also underwent manual inspection. Next, we identified T-
779 individuals in the MTL-Sparing subtype, finding 40.6% of this subtype was composed of this group, and all

780 were classified as stage 5 (of 31) or below. Furthermore these individuals showed many other indications
781 of being false (tau) positives: they had normal MMSE scores, were older, were less likely to be A β + and
782 less likely to be MCI or AD (Extended Data Fig. S2b,c). We assume SuStaln appended this specific group of
783 T- individuals to the MTL-Sparing subtype because the individuals i) had abnormally high tau in at least
784 one ROI as per our calculations (even if that abnormal signal was not driven by pathology); ii) the abnor-
785 mal tau was located mainly in the isocortex inclusive of the parietal lobe; iii) these individuals did not have
786 elevated MTL binding. As SuStaln is an unsupervised algorithm, the pathological MTL-sparing phenotype
787 became conflated with this specific profile of T- individuals. To correct this issue, we converted all T- indi-
788 viduals classified as MTL-sparing to Subtype 0 for all further analysis.

789
790 **Visualization of subtype-specific tau-PET patterns.** To visualize tau-PET patterns for each subtype, we calcu-
791 lated the mean tau Z-score for each Desikan-Killiany (freesurfer) atlas ROI. To visualize the progression of
792 the subtype pattern across SuStaln stages, for each subtype, we created mean images for all individuals
793 falling into the following SuStaln stage bins: 2-6, 7-11, 12-16, 17-21, 22-26. To deduce regions with rela-
794 tively greater or less tau signal for each subtype, we created region-wise one-vs-all ordinary least squares
795 (OLS) linear models comparing regional tau in one subtype to all others. This analysis was performed to
796 visualize subtype models inferred by SuStaln using individual data, and to explore differences between
797 subtypes. Each model included ROI tau Z-scores as the dependent variable, a one-hot dummy variable
798 representing membership in the reference subtype, and SuStaln stage as a covariate. These models were
799 FDR-corrected for the number of comparisons (i.e. number of ROIs).

800
801 **Subtype Characterization.** Several demographic, cognitive and genetic variables were available for nearly
802 all individuals across the five cohorts in our main (discovery) cohort. These variables included clinical di-
803 agnosis (100%), age (99.8%), sex (100%), years of education (97.1%), mini mental state examination
804 (MMSE) score (97.7%) and *APOE4* allele carriage (89.5%). Only the UCSF sample provided diagnoses of
805 clinical AD variants such as PCA¹⁶ and IvPPA¹⁷. In addition, most individuals underwent extensive cohort-
806 specific cognitive batteries assessing multiple domains of cognition. In order to utilize this rich cognitive
807 data, we created cognitive domain scores separately within each cohort by taking the mean of several z-
808 scored tests within the following cognitive domains: memory, executive function, language and visuospa-
809 tial function. Supplemental Table S5 indicates which cognitive tests were used in each cognitive domain
810 score across each cohort. We calculated global cognition as the mean between the four domain scores.
811 Finally, we additionally regressed global cognition out of each domain score to create "relative" cognitive
812 domain scores. These scores are useful for assessing the degree of domain-specific impairment above and
813 beyond global impairment. The various absolute and relative domain scores were then aggregated across
814 all cohorts to maximize the sample size available for cognitive tests: memory (86.6%), language (81.3%),
815 executive function (85.5%), visuospatial function (82.0%). While aggregating scores of different composi-
816 tions across cohorts of different compositions presents a suboptimal solution, we rest on sample sizes and
817 statistical correction helping to overcome these limitations.

818 Subtypes were statistically compared to one another, and to tau-negative (i.e. Stage 0) individuals,
819 in order to determine subtype-specific characteristics. These analyses compared age, sex, education, AP-
820 OE4 carriage, MMSE, global cognition, total tau, and total tau asymmetry. Comparisons between subtypes
821 and Stage 0 individuals additionally included the four cognitive domain scores, while comparison between
822 subtypes instead included the four "relative" cognitive domain scores. This statistical comparison involved
823 three steps: 1) Comparison to tau-negative individuals: Tau-negative individuals were those characterized
824 as "Subtype 0" by SuStaln, i.e. those individuals that did not demonstrate any abnormal tau events. An
825 OLS linear model was fit with each variable described above as the dependent variable, and with dummy-
826 coded subtype entered as the independent variable (with S0 as the reference subtype). The model also
827 included age, sex, education, clinical status (CN, MCI, AD) and cohort as covariates (except when that co-
828 variate was the dependent variable). Model t- and p-values were stored for each model and the latter
829 were FDR-corrected. 2) Comparison between subtypes. A one-vs-all approach was applied to subtyped
830 individuals only to assess how different tau-progression subtypes differed from one another. Separately

831 for each subtype, models were fit for each variable with a single dummy variable entered indicating
832 membership to that subtype. Models once again covaried for age, sex, education, clinical status (CN, MCI,
833 AD), cohort, and, this time, SuStaln stage. T and p values were stored, and the latter was FDR-corrected
834 for the number of variables assessed. 3) Finally, each subtype was compared directly to each other sub-
835 type (i.e. one-vs-one comparison). OLS models were fit with dummy coded subtype variables as the de-
836 pendent variable, cycling each subtype as the reference subtype. T and p values for each of these models
837 were stored, and the latter was FDR-corrected for number of comparisons (i.e. number of dependent var-
838 iables). These models were also adjusted for age, sex, education, clinical status (CN, MCI, AD), cohort and
839 SuStaln stage. For space reasons, the results of 3) are only visible in Extended Data Fig. S8.

840 All models were subjected to diagnostics to ensure our data fulfilled assumptions of OLS regression
841 models. We found the residuals of all models to be normally distributed (Anderson-Darling tests $p > 0.05$).
842 Further, we found no strong evidence for autocorrelation (Durbin Watson test, $1.5 < \text{all models} < 2.5$),
843 outliers (Cooks distance of all subjects < 0.5), multicollinearity (variance inflation factor (VIF) for all covari-
844 ates < 100 ; besides age [23-27], sex [8-12] and education [13-17], all VIF < 10) or heteroscedasticity (visual
845 assessment of distribution around mean of residuals) in any of our models.

846 We also assessed the relationship between SuStaln stage and two variables: age and MMSE. For
847 these analyses, stage was correlated with age and MMSE, and the results were visualized across the
848 whole sample and also stratified by subtype. As a post-hoc analysis, we separated individuals into differ-
849 ent age groups: 65 or younger, and older than 65. We then reassessed age by SuStaln stage correlations
850 within each of these age groups.

851 Longitudinal MMSE data was also available for individuals from all cohorts, totalling 735 individuals
852 with at least two timepoints. 195 individuals had an additional third timepoint, 29 had a fourth, and 3 had
853 a fifth. Mean latest follow-up was 1.72 years from PET scan ($sd = 0.64$). Linear mixed effect models were
854 used to assess difference in longitudinal MMSE change between subtypes. All models were fit using the
855 lme4 library in R, using type-III sum of squares, unstructured covariance matrices, and Satterthwaite's
856 approximation to calculate the denominator degrees of freedom for p-values. Models featured MMSE
857 measurements as the dependent variable, interactions between time from baseline and dummy coded
858 subtype variables as the independent variables of interest (cycling the reference subtype), subject ID as a
859 random effect (allowing for random intercepts and slopes), and age, sex, education, cohort, dummy cod-
860 ed variables for MCI and AD, and SuStaln stage as covariates of no interest. One vs all models were also fit
861 for each subject using dummy coded subtype variables, and significant effects were reported. We addi-
862 tionally repeated the one vs. all subtype models within each cohort separately, and used this to calculate
863 a meta-analysis by finding a weighted mean of the t-values and standard errors. Since this analysis was
864 confirmatory, we used a one-tailed significance test to calculate the p-values.

865
866 **Replication Analysis.** We performed two types of replication analysis. To ensure that our results were not
867 driven by arbitrary z-score cutoffs, we reran models with completely different cutoffs. To ensure the re-
868 sults were not driven by our sample or unique to the flortaucipir radiotracer, we repeated the analysis *de*
869 *novo* in a separate cohort using a different tau-PET radiotracer.

870 SuStaln require z-score values to anchor the pseudotime for each ROI (see section Subtype and
871 Stage Inference above), and we chose values of 2,5,10 for all ROIs so as to not let any region bias or influ-
872 ence the model unduly, and to aid comparability across different regions. To ensure our results were not
873 driven by this choice, we reran the model with a different set of z-score values chosen in a data-driven
874 manner. The object was to allow the distribution of tau-PET data in each region to define natural way-
875 points in the data. For each input region, we fit Gaussian mixture models to the data, varying the number
876 of components between 1 and 5. We used the model fit (AIC) to decide the optimal number of compo-
877 nents for each region. Finally, we used five-fold cross-validation to determine the boundaries of these
878 Gaussians to define anchors for each regions. We did this separately for each ROI, and as a result, differ-
879 ent ROIs had different waypoints, and even different numbers of waypoints (Table S6). We then refit the

880 SuStaln model to the data and compared the results to the original model using spatial correlation (see
881 below).

882 While the five cohorts from the main discovery sample all use flortaucipir as the tau-PET tracer, a
883 sixth cohort (BioFINDER II; BF2) was available that instead used the RO948 radiotracer. While the two
884 tracers have similar binding patterns, RO948 tends to have less off-target binding in the basal ganglia and
885 better MTL signal, but frequently boasts high meningeal signal that can affect cortical SUVR measure-
886 ment⁵³. Because of these differences, we opted to leave BF2 out of the discovery sample, and instead use
887 it as a replication cohort. This strategy allowed us to not only evaluate the stability of the subtypes in a
888 new cohort, but also allowed us to evaluate whether the subtypes are robust to tau-PET radiotracer.

889 We reran SuStaln *de novo* in the BF2 sample, using identical procedures to those described above
890 (Methods: Subtype and Stage Inference), although using the discovery sample to inform the number of
891 subtypes. The resulting subtypes were visualized and quantitatively assessed using spatial correlations.
892 Specifically, mean within-subtype SUVRs were computed for each (freesurfer) ROI, and each discovery
893 subtype ROI-vector was correlated to each replication (BF2) subtype ROI-vector. To account for whether
894 different sample sizes contribute to differing results between the discovery and replication datasets, we
895 performed a split-half analysis with the discovery sample. Specifically, we split the discovery sample in
896 half and ran SuStaln separately on each half, once again using the original discovery sample to inform the
897 number of subtypes. We then compared each half, which had a sample size comparable to that of BF2, to
898 the BF2 samples using spatial correlations.

899
900 **Assessment of Longitudinal Stability.** Longitudinal PET data was available for individuals across all cohorts
901 except for UCSF, totaling 519 individuals with at least two time points (mean follow-up time = 1.42, sd =
902 0.58, years). These longitudinal scans were used to validate the stability of subtypes over time, under the
903 hypothesis that individuals should remain the same subtype, but should advance (or remain stable) in
904 SuStaln stage over time. ROIs for the longitudinal datasets were Z-scored as described above, but using
905 the cross-sectional cohort as the cohort for normalization. The SuStaln model fitted to the cross-sectional
906 dataset was used to infer subtype and stage of longitudinal data (all timepoints). Confusion matrices were
907 built to assess subtype stability between baseline and first follow-up. Stability was calculated as propor-
908 tion of individuals classified as the same subtype at follow-up, or who advanced from Stage 0 into a sub-
909 type, compared to the total number of individuals. Stability was also calculated excluding individuals who
910 were classified as Stage 0 at baseline or follow-up. We also assessed the influence of subtype probability
911 (i.e. the probability a subject falls into their given subtype) on individual subtype stability. Specifically, we
912 compared the subtype probability of stable individuals to unstable individuals with a t-test. We addition-
913 ally calculated overall model stability after excluding individuals using various subtype probability thresh-
914 olds.

915 Subtype progression was assessed by observing change in SuStaln stage over time in stable subtype
916 individuals. We calculated the proportion of individuals who advanced, were stable, or regressed in dis-
917 ease stage over time, before and after accounting for model uncertainty. Specifically, while stages are
918 generally characterized by advancing abnormality in a given region, uncertainty leads to some stages be-
919 ing characterized by probabilities of progressing abnormalities in more than one region. Therefore, indi-
920 viduals who advanced or regressed to a stage with event probabilities overlapping with their previous
921 stage were considered to be stable. We also calculated annual change in SuStaln stage by dividing total
922 change in SuStaln stage by number of years between baseline and final available timepoint. We used one-
923 sample t-test against zero to assess whether significant change over time was observed across the whole
924 sample, and within each subtype. We used ANOVAs and Tukey's post-hoc tests to assess differences in
925 annual change in stage across the different subtypes. We also correlated annual change in stage with
926 baseline stage, and with age.

927
928 **Individual forecasting of longitudinal tau progression.** SuStaln models spatiotemporal subtype progressions,
929 but does so using only cross-sectional data. Therefore, longitudinal data can be used as "unseen" or "left-

930 out" data, which can be used to test whether and to what extent individuals follow the trajectories pre-
 931 dicted by SuStaln. We accomplish this by using an individual's subtype and stage probability to generate a
 932 predicted second time point, and comparing the change between baseline and predicted follow-up to
 933 change between baseline and actual follow-up.

934 To do this, we first sought to predict the rate of change of stage for each individual. We trained a
 935 Lasso model to predict individual annualized change in SuStaln stage (Δ stage) using available data, and
 936 cross-validation to get out-of-sample predictions for each individual. Features included age, sex, educa-
 937 tion, amyloid status, APOE4 status, baseline stage MMSE and dummy coded variables for MCI, AD, and
 938 each subtype. For each fold, the model was trained on 90% of the data, and this model was used to pre-
 939 dict Δ stage in the 10% left out subjects. This process was repeated until predictions were made for each
 940 subject. The mean absolute error between the predicted and true Δ stage was 0.91 stages/year. The pre-
 941 dicted Δ stage was used for subsequent aspects of the tau prediction. This is important, as we are there-
 942 fore minimizing the amount of longitudinal information leaking into the forecast.

943 Using this predicted Δ stage, we were then able to predict an individual's stage at follow-up $k_{i,new}$ giv-
 944 en any stage at baseline k , as $k_{i,new} = k + \Delta_{stage} t_i$, where t_i is the time between follow-up visits in years.

945 We can then evaluate the SuStaln-predicted pattern of regional tau deposition at baseline Y_{ij} as

$$Y_{ij} = \sum_{c=1}^C \sum_{k=0}^K A_{j,c,k} P_{i,c,k}$$

946 or at follow-up Z_{ij} as

$$Z_{ij} = \sum_{c=1}^C \sum_{k=0}^K A_{j,c,k_{i,new}} P_{i,c,k}$$

947 where $A_{j,c,k}$ is an 'archetype' indicating the expected amount of tau deposition for biomarker j at stage k of
 948 subtype c and $P_{i,c,k}$ is the probability subject i is at stage k of subtype c . The archetype $A_{j,c,k}$ is estimated
 949 probabilistically from the Markov chain Monte Carlo (MCMC) samples of uncertainty provided by the Su-
 950 staln algorithm, giving an average archetypal pattern accounting for the uncertainty in the progression
 951 pattern of each subtype. This means that each SuStaln-predicted pattern Y_{ij} accounts for both uncertainty
 952 in the progression pattern of each subtype as well as uncertainty in the subtype and stage of each individ-
 953 ual.

954 We can therefore represent the predicted change in tau as $Z_{ij} - Y_{ij}$. This vector represents the pre-
 955 dicted change in tau Z-score in each of the ten spatial input features to SuStaln (i.e. left and right tem-
 956 poral, parietal, occipital, frontal and medial temporal lobes). We evaluate the prediction by computing,
 957 for each individual, the correlation between the predicted and true regional tau change vectors. We eval-
 958 uate the overall prediction across the whole sample, and within-subtypes, by comparing the average pre-
 959 diction against chance using one-sample t-tests against a correlation of zero.

960
 961 **Epidemic spreading model.** Perhaps the most prominent hypothesis of tau spread suggests tau oligomers
 962 spread directly from neuron to neuron through axonal connections. Under this hypothesis, diverse but
 963 systematic variations in tau spreading may be driven by variability in macroscale connectivity, network
 964 organization or vulnerable circuits. We test this idea by investigating whether a network diffusion model
 965 simulating tau spread through the human connectome can recapitulate the various subtype patterns dis-
 966 covered by SuStaln. We have previously applied the epidemic spreading model (ESM)⁵⁸ to tau-PET data,
 967 showing diffusion of an agent through human connectivity data (measured with diffusion imaging-based
 968 tractography) can explain a majority of the variance of spatial tau patterns across a population of individ-
 969 uals along the AD spectrum²⁹. We here conduct the exact same analysis separately for each subtype iden-
 970 tified through SuStaln. We further allow the ESM to identify regional epicenters separately for each sub-
 971 type, under the hypothesis that different subtype patterns may be driven by prominence of different cor-
 972 ticolimbic networks.

973 As described in²⁹, each tau-PET ROI was converted to tau-positive probabilities using mixture mod-
974 eling. This process is similar to the Z-scoring procedure (Extended Data Fig. S1), though in this case, the
975 probability that values fall onto the abnormal distribution is ascertained using five-fold cross-validation.
976 These measures represent the probability that a given ROI exhibits tau in the abnormal range. Connectivi-
977 ty was measured from a dataset of 60 young healthy subjects from the CMU-60 DSI Template
978 (<http://www.psy.cmu.edu/coaxlab/data.html>). Deterministic tractography was calculated for each indi-
979 vidual by finding connections between ROIs using orientation distribution functions, and connectivity was
980 measured using the anatomical connection density (ACD) metric⁵⁸. Images were assessed for quality and
981 connectomes were averaged across all 60 individuals. For each subtype separately, the ESM was fitted
982 across all individuals, cycling through the average of each left-right pair of cortical ROIs (including hippo-
983 campus and amygdala, 33 pairs in total) as the model epicenter. The best fitting epicenter was selected by
984 finding the model with the minimum mean euclidian distance between model predicted and observed tau
985 spatial pattern across subjects. Model accuracy was represented as the r^2 between the mean observed
986 ROI-level tau-PET probabilities and mean predicted probabilities across subjects. For each subtype, we
987 compared the r^2 of the model using the best-fitting epicenter to the r^2 of models using an entorhinal epi-
988 center. To gain confidence in the subject-specific epicenter, we bootstrapped the sample 1000 times and
989 recomputed the best-fitting epicenter for each subtype. Epicenter probability was calculated as the fre-
990 quency that an epicenter was selected as best epicenter across bootstrap samples.

991 We were additionally interested in how secondary seeding evolved over the course of each subtype
992 progression. While the ESM is designed to ascertain the true pathological epicenter, the selected epicen-
993 ter reflects the seeding point that best matches the spatial pattern of the dependent variable. As such, it
994 is likely that "secondary epicenters" become important for disease spread at later disease stages. We
995 binned individuals for each subtype into disease stage bins, as with Fig 1e. Individual epicenters were as-
996 certained for each subject, and were aggregated based on lobe (MTL, temporal, frontal, parietal, occipi-
997 tal). We then calculated epicenter frequency among individuals in each stage bin for each subtype. This
998 allowed us to track how the secondary epicenter evolve throughout the disease course for each subtype
999 trajectory.

1000 We repeated this same analysis with a different connectome based on rsfMRI connectivity from an
1001 elderly population, and using a higher-resolution atlas. The sample consisted of rsfMRI scans from 422
1002 healthy elderly controls (166 A β -positive), 138 individuals with subjective cognitive decline but without
1003 objective impairment (48 A β -positive), and 83 A β -positive MCI patients. 57 individuals overlapped be-
1004 tween this sample and the tau-PET discovery sample used for analysis. Functional data was processed
1005 using modified CPAC pipeline⁶⁰ involving slice time correction, bandpass filtering at 0.01-0.1 Hz, regression
1006 of motion, white matter and CSF signal, compcor physiological noise, and the 24 Friston parameters. The
1007 timeseries also underwent adaptive censoring of volumes for which DVARS jumps above median+1.5*IQR
1008 were observed. Timeseries were averaged within ROIs of the 246-ROI Brainnetome cortical/subcortical
1009 atlas (<https://atlas.brainnetome.org/>), nodewise connectivity was calculated using either Fisher's Z trans-
1010 formed correlations or partial-correlation (see below). The ESM was fit using the bilateral A35/36r ROI as
1011 model epicenter, and the following combinations of parameters were varied: regions (cortical only or all
1012 regions), subject-base (A β -negative only vs. all subjects), density (edgewise thresholding at 0.02, 0.5, 0.1,
1013 0.25, 1, or partial correlation with no thresholding, and normalization (whether connectivity matrices
1014 were normalized after density thresholding). The only parameter strongly affecting model performance
1015 was density threshold – partial correlation far outperformed all other conditions. Using all regions over
1016 only cortical regions bore slight advantages, as did using all subjects over only A β -negative. Normalization
1017 had no effect on outcomes. The best-fitting model was used for further analysis. The ESM was fit to each
1018 subject separately, and epicenter bootstrapping was performed, both as described above.

1021 **Methods References**

1022
1023 58. Iturria-Medina, Y., Sotero, R. C., Toussaint, P. J. & Evans, A. C. Epidemic Spreading Model to Characterize

- 1024 Misfolded Proteins Propagation in Aging and Associated Neurodegenerative Disorders. *PLoS Comput. Biol.*
1025 **10**, (2014).
1026 59. Cho, H. *et al.* Predicted sequence of cortical tau and amyloid- β deposition in Alzheimer disease spectrum.
1027 *Neurobiol. Aging* **68**, 76–84 (2018).
1028 60. Craddock C, Sikka S, Cheung B, Khanuja R, Ghosh SS, Yan C, Li Q, Lurie D, Vogelstein J, Burns R, C. S. &
1029 Mennes M, Kelly C, Di Martino A, C. F. and M. M. Towards Automated Analysis of Connectomes: The Con-
1030 figurable Pipeline for the Analysis of Connectomes (C-PAC). *Front. Neuroinform.* **7**, (2013).
1031
1032

1033 **Alzheimer's Disease Neuroimaging Initiative**

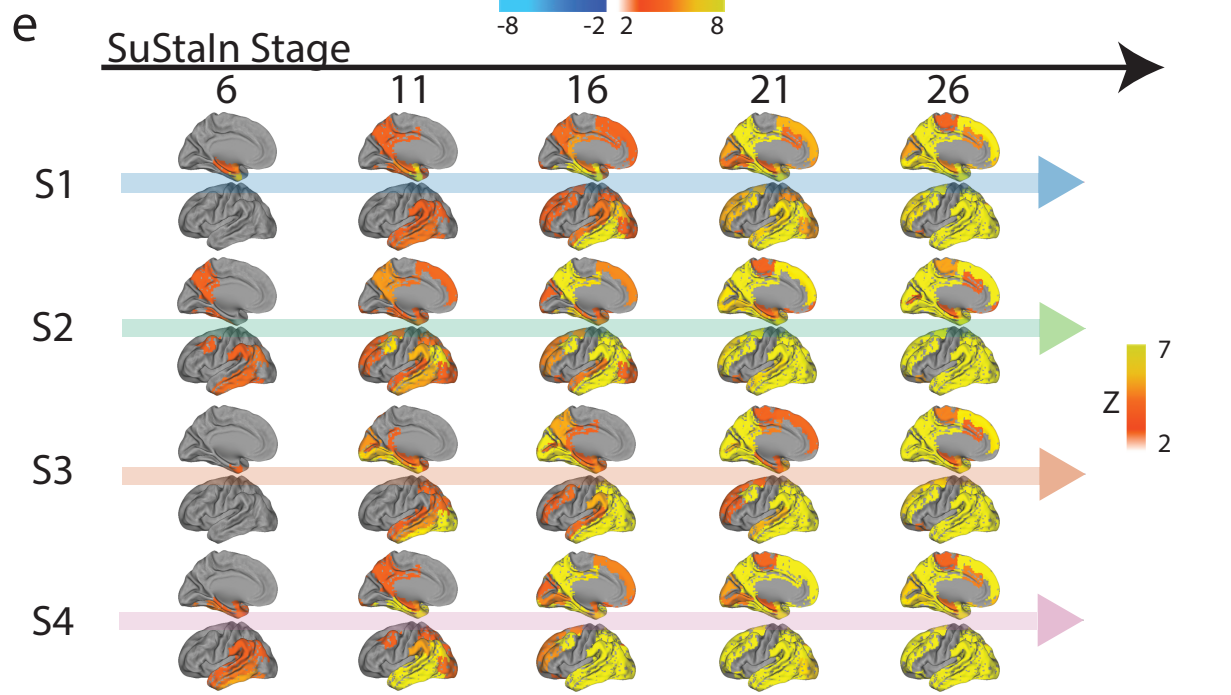
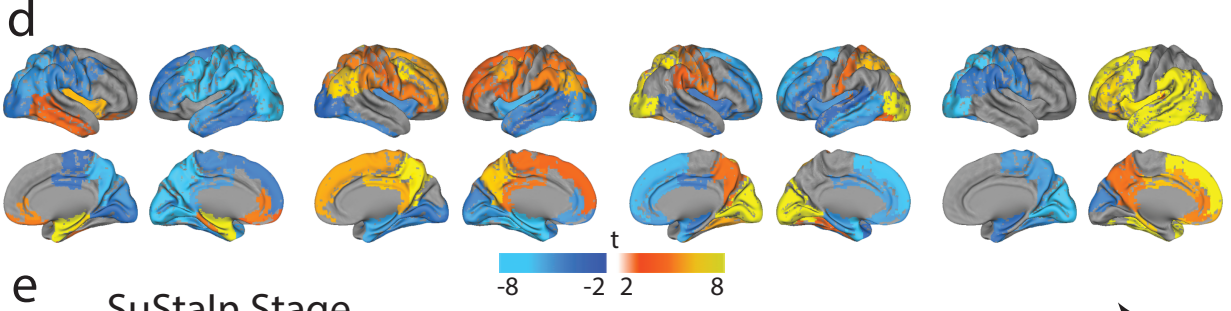
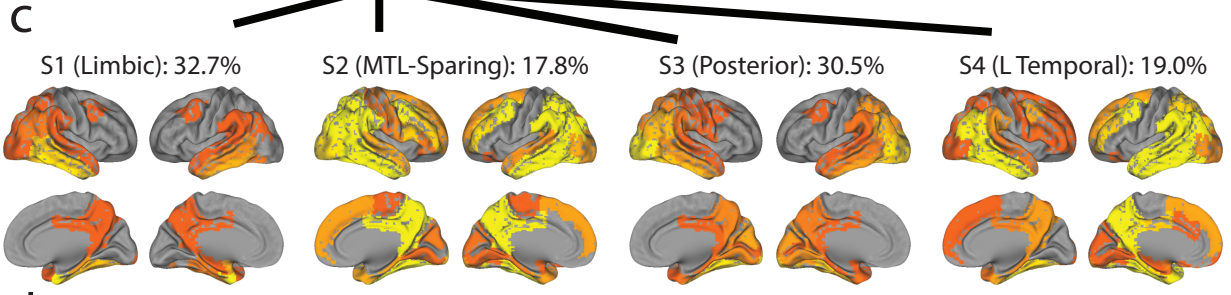
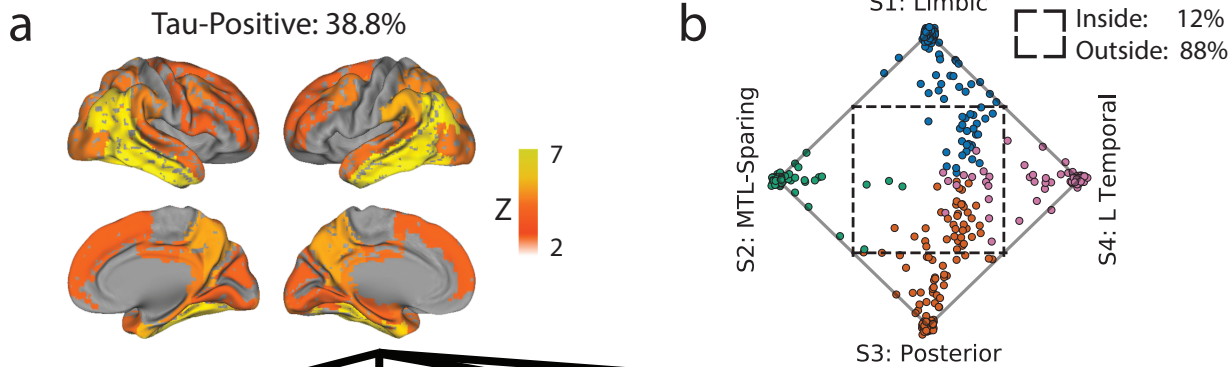
- 1034 Michael Weiner¹⁷, Paul Aisen¹⁸, Ronald Petersen¹⁹, Clifford R. Jack Jr.¹⁹, William Jagust²⁰, John
1035 Q. Trojanowki²¹, Arthur W. Toga²², Laurel Beckett²³, Robert C. Green²⁴, Andrew J. Saykin²⁵,
1036 John Morris²⁶, Leslie M. Shaw²⁷, Enchi Liu²⁸, Tom Montine²⁹, Ronald G. Thomas¹⁸, Michael
1037 Donohue¹⁸, Sarah Walter¹⁸, Devon Gessert¹⁸, Tamie Sather¹⁸, Gus Jiminez¹⁸, Danielle Harvey²³,
1038 Matthew Bernstein¹⁹, Nick Fox³⁰, Paul Thompson³¹, Norbert Schuff³², Charles DeCarli²³, Bret
1039 Borowski¹⁹, Jeff Gunter¹⁹, Matt Senjem¹⁹, Prashanthi Vemuri¹⁹, David Jones¹⁹, Kejal Kantarci¹⁹,
1040 Chad Ward¹⁹, Robert A. Koeppe³³, Norm Foster³⁴, Eric M. Reiman³⁵, Kewei Chen³⁵, Chet
1041 Mathis³⁶, Susan Landau²⁰, Nigel J. Cairns²⁶, Erin Householder²⁶, Lisa Taylor Reinwald²⁶,
1042 Virginia Lee³⁷, Magdalena Korecka³⁷, Michal Figurski³⁷, Karen Crawford²², Scott Neu²², Tatiana
1043 M. Foroud²⁵, Steven Potkin³⁸, Li Shen²⁵, Faber Kelley²⁵, Sungeun Kim²⁵, Kwangsik Nho²⁵,
1044 Zaven Kachaturian³⁹, Richard Frank⁴⁰, Peter J. Snyder⁴¹, Susan Molchan⁴², Jeffrey Kaye⁴³,
1045 Joseph Quinn⁴³, Betty Lind⁴³, Raina Carter⁴³, Sara Dolen⁴³, Lon S. Schneider⁴⁴, Sonia
1046 Pawluczyk⁴⁴, Mauricio Beccera⁴⁴, Liberty Teodoro⁴⁴, Bryan M. Spann⁴⁴, James Brewer⁴⁵, Helen
1047 Vanderswag⁴⁵, Adam Fleisher³⁵, Judith L. Heidebrink³³, Joanne L. Lord³³, Sara S. Mason¹⁹,
1048 Colleen S. Albers¹⁹, David Knopman¹⁹, Kris Johnson¹⁹, Rachelle S. Doody⁴⁶, Javier Villanueva
1049 Meyer⁴⁶, Munir Chowdhury⁴⁶, Susan Rountree⁴⁶, Mimi Dang⁴⁶, Yaakov Stern⁴⁷, Lawrence S.
1050 Honig⁴⁷, Karen L. Bell⁴⁷, Beau Ances⁴⁸, John C. Morris⁴⁸, Maria Carroll⁴⁸, Sue Leon⁴⁸, Mark A.
1051 Mintun⁴⁸, Stacy Schneider⁴⁸, Angela Oliver⁴⁹, Randall Griffith⁴⁹, David Clark⁴⁹, David
1052 Geldmacher⁴⁹, John Brockington⁴⁹, Erik Roberson⁴⁹, Hillel Grossman⁵⁰, Effie Mitsis⁵⁰, Leyla
1053 deToledo-Morrell⁵¹, Raj C. Shah⁵¹, Ranjan Dua⁵², Daniel Varon⁵², Maria T. Greig⁵², Peggy
1054 Roberts⁵², Marilyn Albert⁵³, Chiadi Onyike⁵³, Daniel D'Agostino II⁵³, Stephanie Kielb⁵³, James
1055 E. Galvin⁵⁴, Dana M. Pogorelec⁵⁴, Brittany Cerbone⁵⁴, Christina A. Michel⁵⁴, Henry Rusinek⁵⁴,
1056 Mony J de Leon⁵⁴, Lidia Glodzik⁵⁴, Susan De Santi⁵⁴, P. Murali Doraiswamy⁵⁵, Jeffrey R.
1057 Petrella⁵⁵, Terence Z. Wong⁵⁵, Steven E. Arnold²⁷, Jason H. Karlawish²⁷, David Wolk²⁷, Charles
1058 D. Smith⁵⁶, Greg Jicha⁵⁶, Peter Hardy⁵⁶, Partha Sinha⁵⁶, Elizabeth Oates⁵⁶, Gary Conrad⁵⁶, Oscar

1059 L. Lopez³⁶, MaryAnn Oakley³⁶, Donna M. Simpson³⁶, Anton P. Porsteinsson⁵⁷, Bonnie S.
1060 Goldstein⁵⁷, Kim Martin⁵⁷, Kelly M. Makino⁵⁷, M. Saleem Ismail⁵⁷, Connie Brand⁵⁷, Ruth A.
1061 Mulnard⁵⁸, Gaby Thai⁵⁸, Catherine Mc Adams Ortiz⁵⁸, Kyle Womack⁵⁹, Dana Mathews⁵⁹, Mary
1062 Quiceno⁵⁹, Ramon Diaz Arrastia⁵⁹, Richard King⁵⁹, Myron Weiner⁵⁹, Kristen Martin Cook⁵⁹, Mi-
1063 chael DeVous⁵⁹, Allan I. Levey⁶⁰, James J. Lah⁶⁰, Janet S. Cellar⁶⁰, Jeffrey M. Burns⁶¹, Heather
1064 S. Anderson⁶¹, Russell H. Swerdlow⁶¹, Liana Apostolova⁶², Kathleen Tingus⁶², Ellen Woo⁶²,
1065 Daniel H. S. Silverman⁶², Po H. Lu⁶², George Bartzokis⁶², Neill R Graff Radford⁶³, Francine
1066 ParfittH⁶³, Tracy Kendall⁶³, Heather Johnson⁶³, Martin R. Farlow²⁵, Ann Marie Hake²⁵, Brandy
1067 R. Matthews²⁵, Scott Herring²⁵, Cynthia Hunt²⁵, Christopher H. van Dyck⁶⁴, Richard E. Carson⁶⁴,
1068 Martha G. MacAvoy⁶⁴, Howard Chertkow⁶⁵, Howard Bergman⁶⁵, Chris Hosein⁶⁵, Sandra
1069 Black⁶⁶, Bojana Stefanovic⁶⁶, Curtis Caldwell⁶⁶, Ging Yuek Robin Hsiung⁶⁷, Howard Feldman⁶⁷,
1070 Benita Mudge⁶⁷, Michele Assaly Past⁶⁷, Andrew Kertesz⁶⁸, John Rogers⁶⁸, Dick Trost⁶⁸, Charles
1071 Bernick⁶⁹, Donna Munic⁶⁹, Diana Kerwin⁷⁰, Marek Marsel Mesulam⁷⁰, Kristine Lipowski⁷⁰,
1072 Chuang Kuo Wu⁷⁰, Nancy Johnson⁷⁰, Carl Sadowsky⁷¹, Walter Martinez⁷¹, Teresa Villena⁷¹,
1073 Raymond Scott Turner⁷², Kathleen Johnson⁷², Brigid Reynolds⁷², Reisa A. Sperling⁷³, Keith A.
1074 Johnson⁷³, Gad Marshall⁷³, Meghan Frey⁷³, Jerome Yesavage⁷⁴, Joy L. Taylor⁷⁴, Barton Lane⁷⁴,
1075 Allyson Rosen⁷⁴, Jared Tinklenberg⁷⁴, Marwan N. Sabbagh⁷⁵, Christine M. Belden⁷⁵, Sandra A.
1076 Jacobson⁷⁵, Sherye A. Sirrel⁷⁵, Neil Kowall⁷⁶, Ronald Killiany⁷⁶, Andrew E. Budson⁷⁶,
1077 Alexander Norbash⁷⁶, Patricia Lynn Johnson⁷⁶, Thomas O. Obisesan⁷⁷, Saba Wolday⁷⁷, Joanne
1078 Allard⁷⁷, Alan Lerner⁷⁸, Paula Ogrocki⁷⁸, Leon Hudson⁷⁸, Evan Fletcher⁷⁹, Owen Carmichael⁷⁹,
1079 John Olichney⁷⁹, Charles DeCarli⁷⁹, Smita Kittur⁸⁰, Michael Borrie⁸¹, T Y Lee⁸¹, Rob Bartha⁸¹,
1080 Sterling Johnson⁸², Sanjay Asthana⁸², Cynthia M. Carlsson⁸², Steven G. Potkin⁸³, Adrian Preda⁸³,
1081 Dana Nguyen⁸³, Pierre Tariot³⁵, Stephanie Reeder³⁵, Vernice Bates⁸⁴, Horacio Capote⁸⁴, Michelle
1082 Rainka⁸⁴, Douglas W. Scharre⁸⁵, Maria Katakis⁸⁵, Anahita Adeli⁸⁵, Earl A. Zimmerman⁸⁶, Dzintra
1083 Celmins⁸⁶, Alice D. Brown⁸⁶, Godfrey D. Pearlson⁸⁷, Karen Blank⁸⁷, Karen Anderson⁸⁷, Robert
1084 B. Santulli⁸⁸, Tamar J. Kitzmiller⁸⁸, Eben S. Schwartz⁸⁸, Kaycee M. SinkS⁸⁹, Jeff D.
1085 Williamson⁸⁹, Pradeep Garg⁸⁹, Franklin Watkins⁸⁹, Brian R. Ott⁹⁰, Henry Querfurth⁹⁰, Geoffrey
1086 Tremont⁹⁰, Stephen Salloway⁹¹, Paul Malloy⁹¹, Stephen Correia⁹¹, Howard J. Rosen¹⁷, Bruce L.
1087 Miller¹⁷, Jacobo Mintzer⁹², Kenneth Spicer⁹², David Bachman⁹², Elizabeth Finger⁹³, Stephen
1088 Pasternak⁹³, Irina Rachinsky⁹³, Dick Drost⁹³, Nunzio Pomara⁹⁴, Raymundo Hernando⁹⁴, Antero

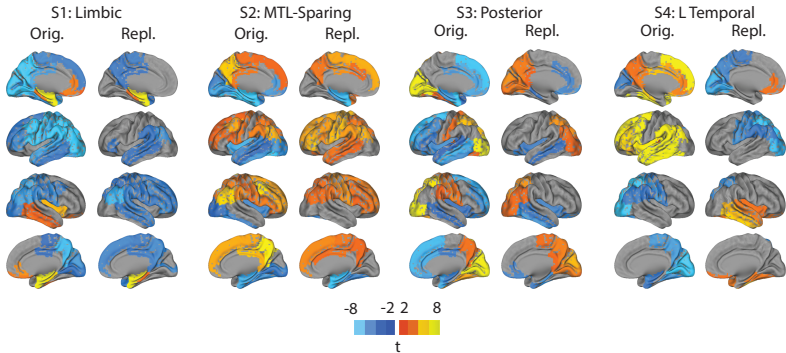
1089 Sarrael⁹⁴, Susan K. Schultz⁹⁵, Laura L. Boles Ponto⁹⁵, Hyungsub Shim⁹⁵, Karen Elizabeth
1090 Smith⁹⁵, Norman Relkin⁹⁶, Gloria Chaing⁹⁶, Lisa Raudin⁹⁶, Amanda Smith⁹⁷, Kristin Fargher⁹⁷,
1091 Balebail Ashok Raj⁹⁷
1092
1093 ¹⁷ UC San Francisco, San Francisco, CA, USA
1094 ¹⁸ UC San Diego, San Diego, CA, USA
1095 ¹⁹ Mayo Clinic, Rochester, NY, USA
1096 ²⁰ UC Berkeley, Berkeley, CA, USA
1097 ²¹ U Pennsylvania, Pennsylvania, CA, USA
1098 ²² USC, Los Angeles, CA, USA
1099 ²³ UC Davis, Davis, CA, USA
1100 ²⁴ Brigham and Women's Hospital, Harvard Medical School, Boston, MA, USA
1101 ²⁵ Indiana University, Bloomington, IND, USA
1102 ²⁶ Washington University St. Louis, St. Louis, MO, USA
1103 ²⁷ University of Pennsylvania, Philadelphia, PA, USA
1104 ²⁸ Janssen Alzheimer Immunotherapy, South San Francisco, CA, USA
1105 ²⁹ University of Washington, Seattle, WA, USA
1106 ³⁰ University of London, London, UK
1107 ³¹ USC School of Medicine, Los Angeles, CA, USA
1108 ³² UCSF MRI, San Francisco, CA, USA
1109 ³³ University of Michigan, Ann Arbor, MI, USA
1110 ³⁴ University of Utah, Salt Lake City, UT, USA
1111 ³⁵ Banner Alzheimer's Institute, Phoenix, AZ, USA
1112 ³⁶ University of Pittsburgh, Pittsburgh, PA, USA
1113 ³⁷ UPenn School of Medicine, Philadelphia, PA, USA
1114 ³⁸ UC Irvine, Newport Beach, CA, USA
1115 ³⁹ Khachaturian, Radebaugh & Associates, Inc and Alzheimer's Association's Ronald and Nancy Reagan's
1116 Research Institute, Chicago, IL, USA
1117 ⁴⁰ General Electric, Boston, MA, USA
1118 ⁴¹ Brown University, Providence, RI, USA
1119 ⁴² National Institute on Aging/National Institutes of Health, Bethesda, MD, USA
1120 ⁴³ Oregon Health and Science University, Portland, OR, USA
1121 ⁴⁴ University of Southern California, Los Angeles, CA, USA
1122 ⁴⁵ University of California San Diego, San Diego, CA, USA
1123 ⁴⁶ Baylor College of Medicine, Houston, TX, USA
1124 ⁴⁷ Columbia University Medical Center, New York, NY, USA

- 1125 ⁴⁸ Washington University, St. Louis, MO, USA
- 1126 ⁴⁹ University of Alabama Birmingham, Birmingham, MO, USA
- 1127 ⁵⁰ Mount Sinai School of Medicine, New York, NY, USA
- 1128 ⁵¹ Rush University Medical Center, Chicago, IL, USA
- 1129 ⁵² Wien Center, Vienna, Austria
- 1130 ⁵³ Johns Hopkins University, Baltimore, MD, USA
- 1131 ⁵⁴ New York University, New York, NY, USA
- 1132 ⁵⁵ Duke University Medical Center, Durham, NC, USA
- 1133 ⁵⁶ University of Kentucky, city of Lexington, NC, USA
- 1134 ⁵⁷ University of Rochester Medical Center, Rochester, NY, USA
- 1135 ⁵⁸ University of California, Irvine, CA, USA
- 1136 ⁵⁹ University of Texas Southwestern Medical School, Dallas, TX, USA
- 1137 ⁶⁰ Emory University, Atlanta, GA, USA
- 1138 ⁶¹ University of Kansas, Medical Center, Lawrence, KS, USA
- 1139 ⁶² University of California, Los Angeles, CA, USA
- 1140 ⁶³ Mayo Clinic, Jacksonville, FL, USA
- 1141 ⁶⁴ Yale University School of Medicine, New Haven, CT, USA
- 1142 ⁶⁵ McGill Univ., Montreal Jewish General Hospital, Montreal, WI, USA
- 1143 ⁶⁶ Sunnybrook Health Sciences, Toronto, ON, Canada
- 1144 ⁶⁷ U.B.C. Clinic for AD & Related Disorders, British Columbia, BC, Canada
- 1145 ⁶⁸ Cognitive Neurology St. Joseph's, Toronto, ON, Canada
- 1146 ⁶⁹ Cleveland Clinic Lou Ruvo Center for Brain Health, Las Vegas, NV, USA
- 1147 ⁷⁰ Northwestern University, Evanston, IL, USA
- 1148 ⁷¹ Premiere Research Inst Palm Beach Neurology, West Palm Beach, FL, USA
- 1149 ⁷² Georgetown University Medical Center, Washington, DC, USA
- 1150 ⁷³ Brigham and Women's Hospital, Boston, MA, USA
- 1151 ⁷⁴ Stanford University, Santa Clara County, CA, USA
- 1152 ⁷⁵ Banner Sun Health Research Institute, Sun City, AZ, USA
- 1153 ⁷⁶ Boston University, Boston, MA, USA
- 1154 ⁷⁷ Howard University, Washington, DC, USA
- 1155 ⁷⁸ Case Western Reserve University, Cleveland, OH, USA
- 1156 ⁷⁹ University of California, Davis Sacramento, CA, USA
- 1157 ⁸⁰ Neurological Care of CNY, New York, NY, USA

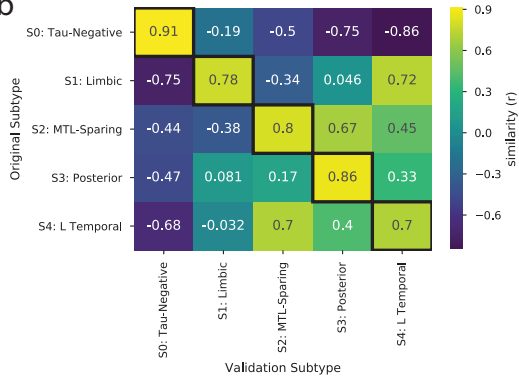
- 1158 ⁸¹ Parkwood Hospital, Parkwood, CA, USA
- 1159 ⁸² University of Wisconsin, Madison, WI, USA
- 1160 ⁸³ University of California, Irvine BIC, Irvine, CA, USA
- 1161 ⁸⁴ Dent Neurologic Institute, Amherst, MA, USA
- 1162 ⁸⁵ Ohio State University, Columbus, OH, USA
- 1163 ⁸⁶ Albany Medical College, Albany, NY, USA
- 1164 ⁸⁷ Hartford Hosp, Olin Neuropsychiatry Research Center, Hartford, CT, USA
- 1165 ⁸⁸ Dartmouth Hitchcock Medical Center, Albany, NY, USA
- 1166 ⁸⁹ Wake Forest University Health Sciences, Winston-Salem, NC, USA
- 1167 ⁹⁰ Rhode Island Hospital, Rhode Island, USA
- 1168 ⁹¹ Butler Hospital, Providence, RI, USA
- 1169 ⁹² Medical University South Carolina, Charleston, SC, USA
- 1170 ⁹³ St. Joseph's Health Care, Toronto, Canada
- 1171 ⁹⁴ Nathan Kline Institute, Orangeburg, SC, USA
- 1172 ⁹⁵ University of Iowa College of Medicine, Iowa City, IA, USA
- 1173 ⁹⁶ Cornell University, Ithaca, NY, USA
- 1174 ⁹⁷ University of South Florida: USF Health Byrd Alzheimer's Institute, Tampa, FL 33613 USA

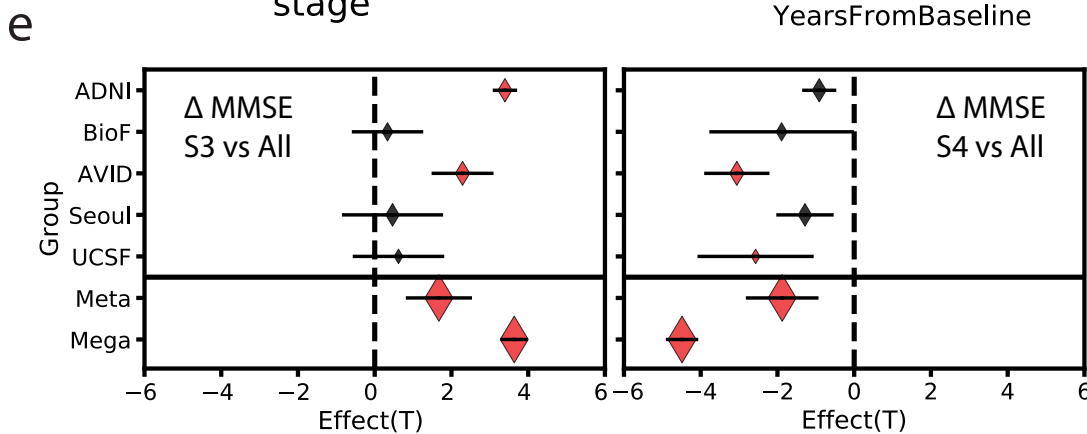
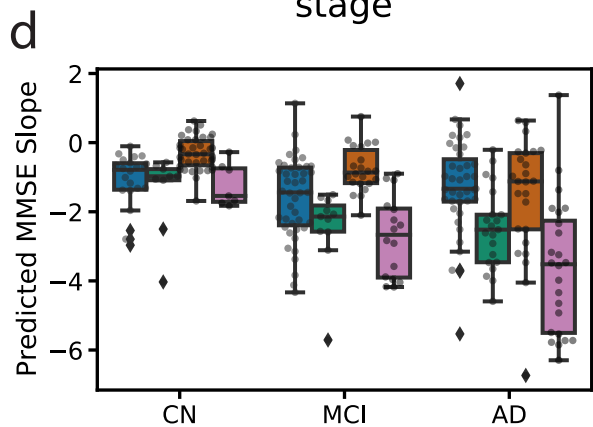
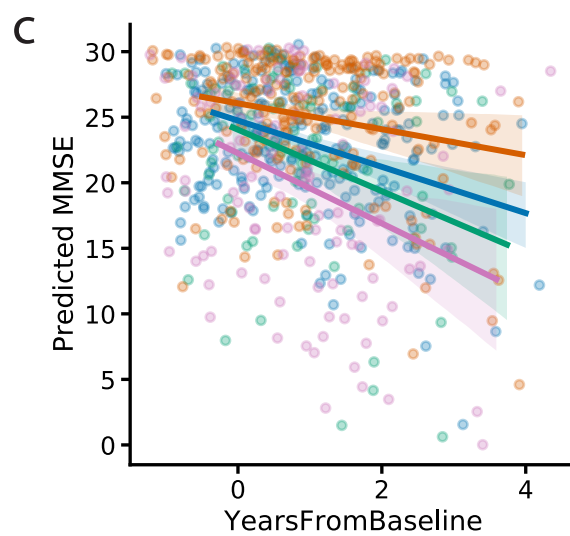
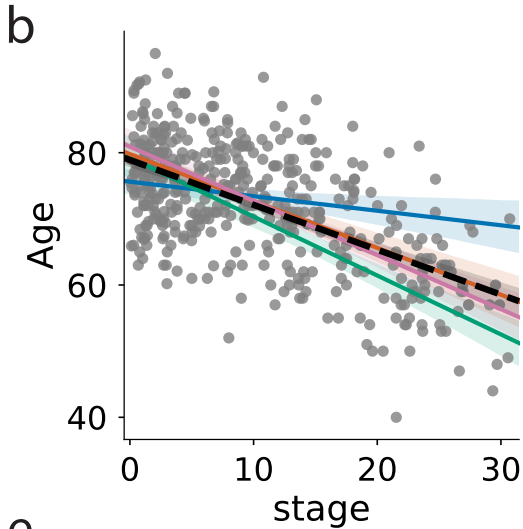
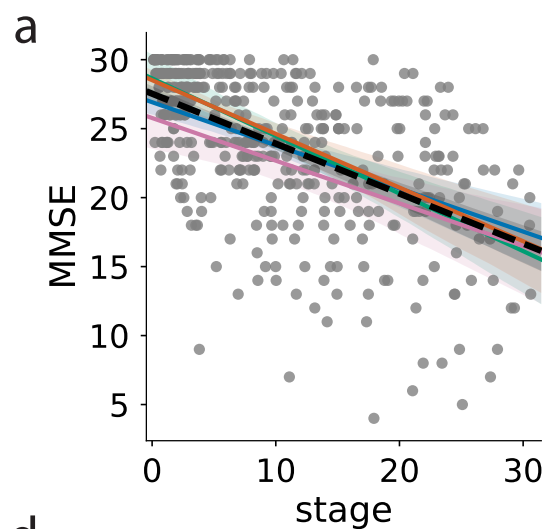


a



b



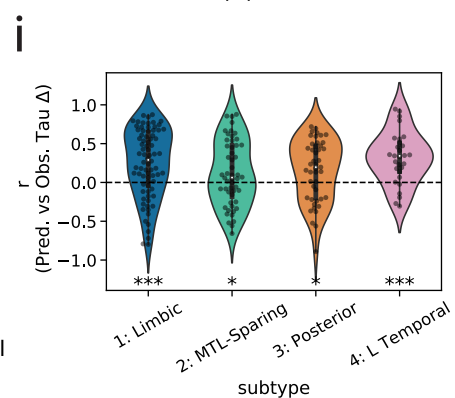
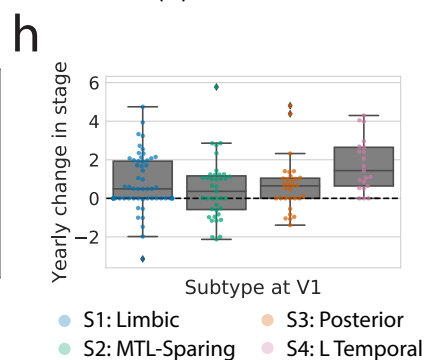
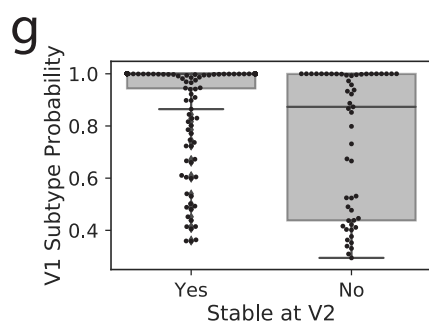


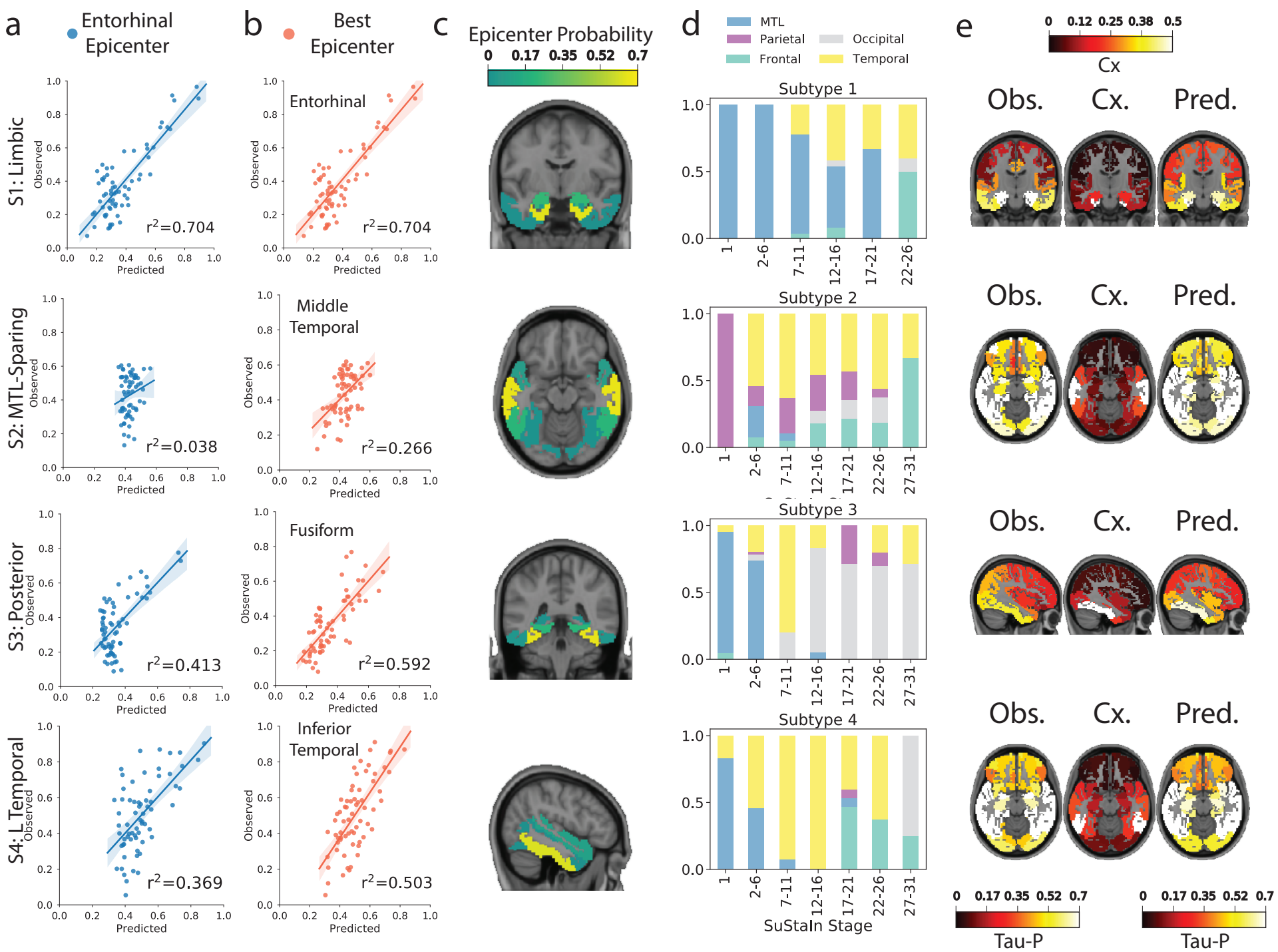
f

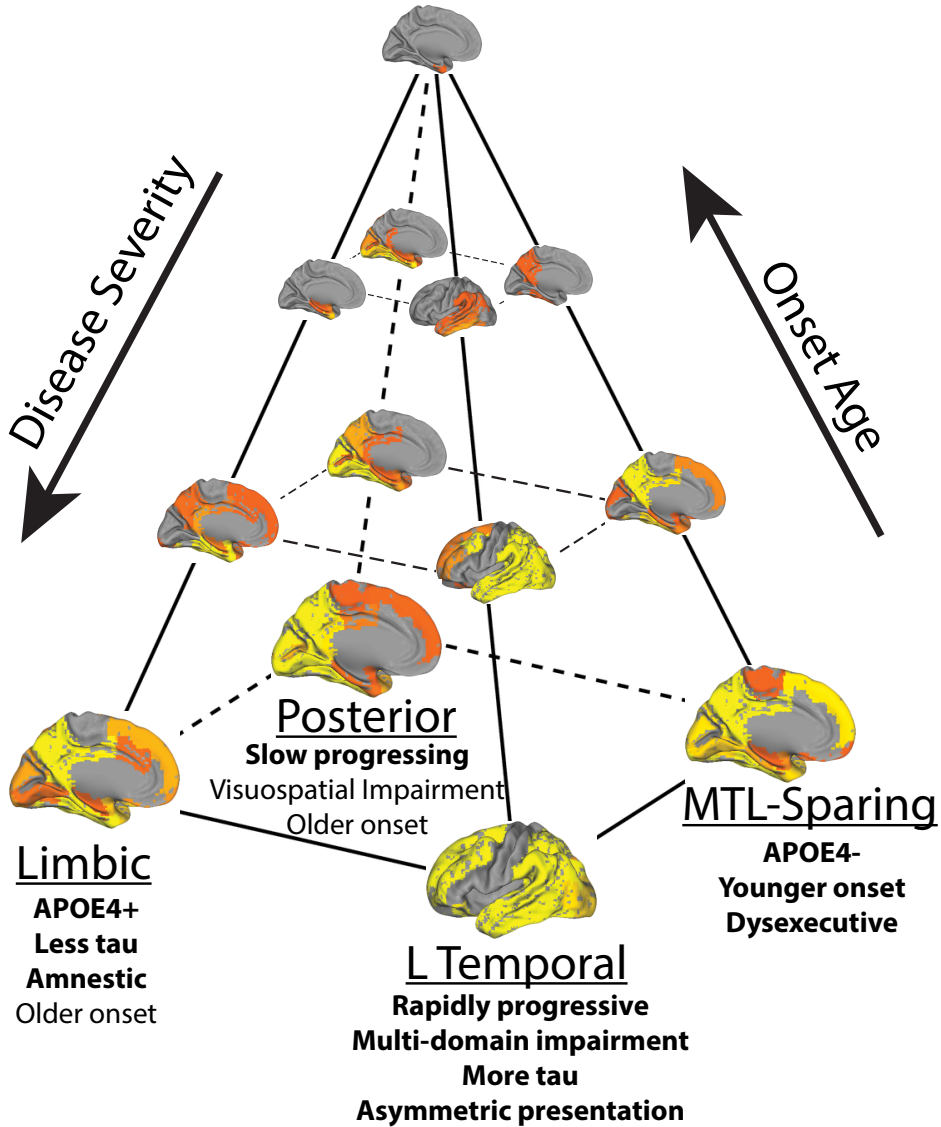
Stage 0	275	7	7	7	2
Visit 1					
S1: Limbic	7	60	1	5	1
S2: MTL-Sparing	9	5	42	1	4
S3: Posterior	12	6	1	33	1
S4: L Temporal	1	1	4	0	21
Visit 2					
S0					
S1					
S2					
S3					
S4					

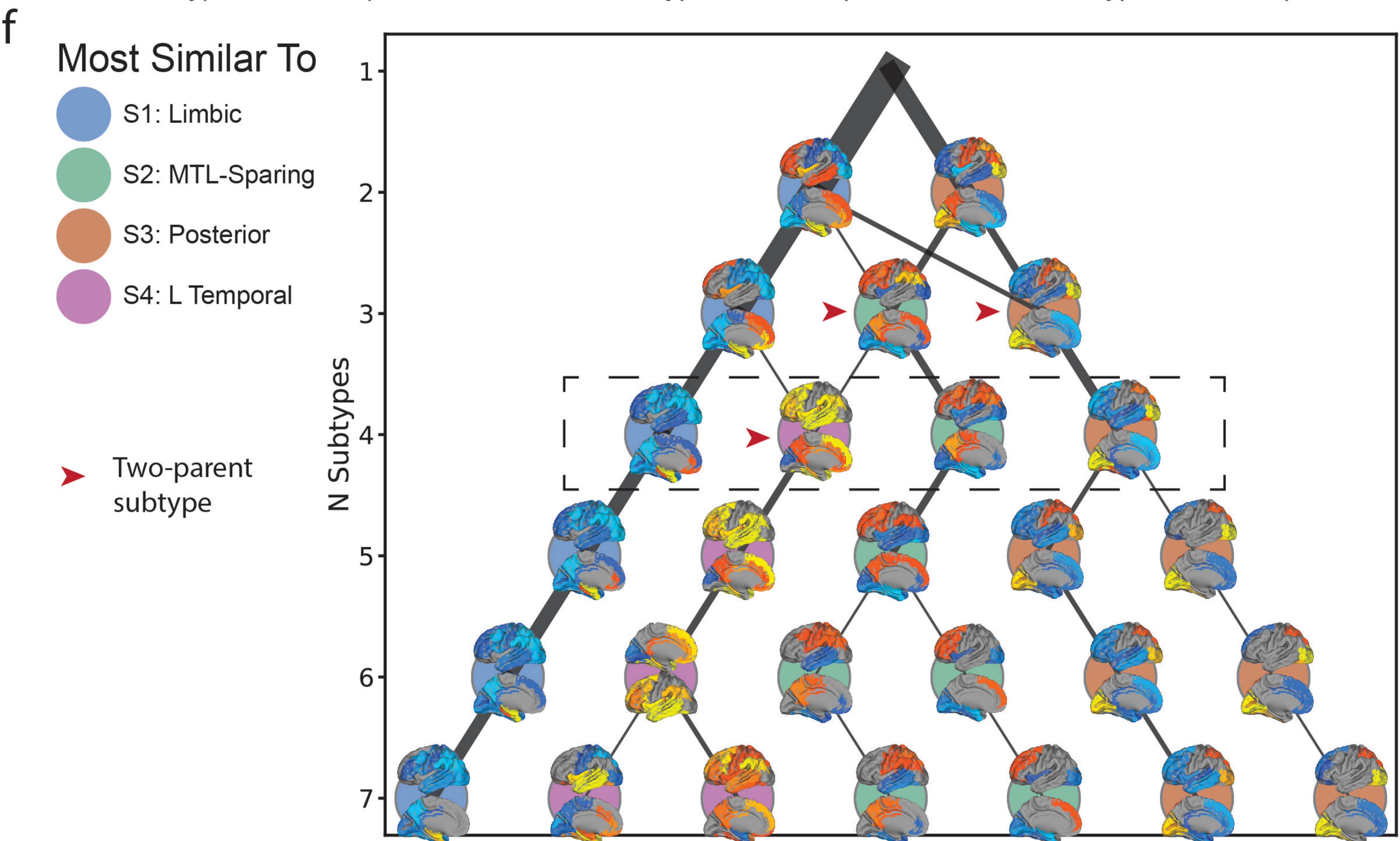
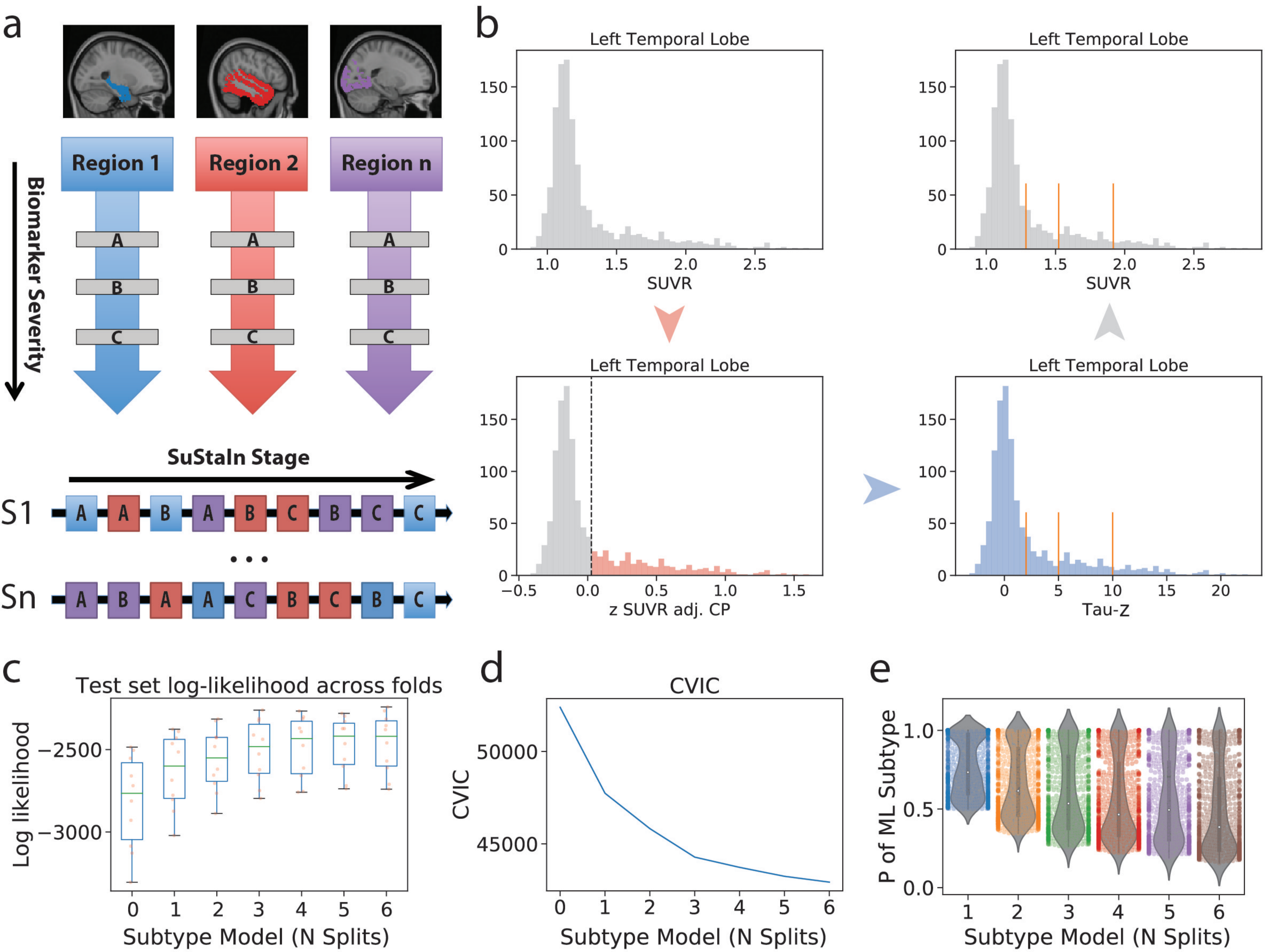
Visit 1

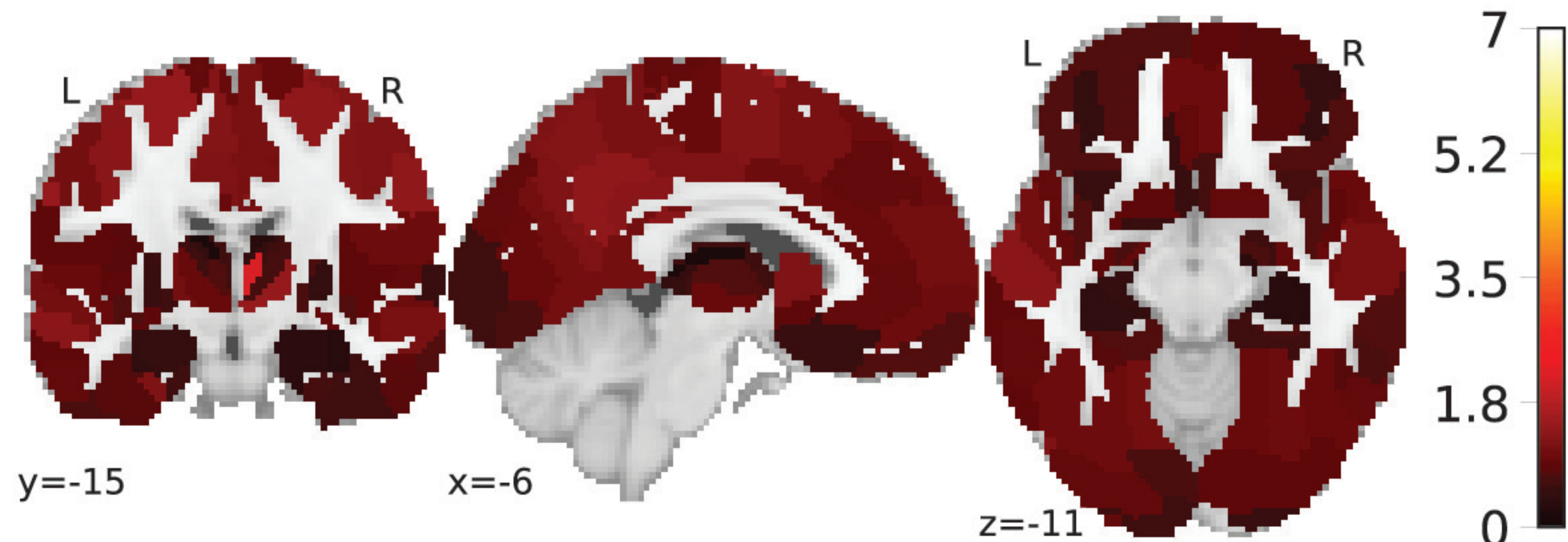
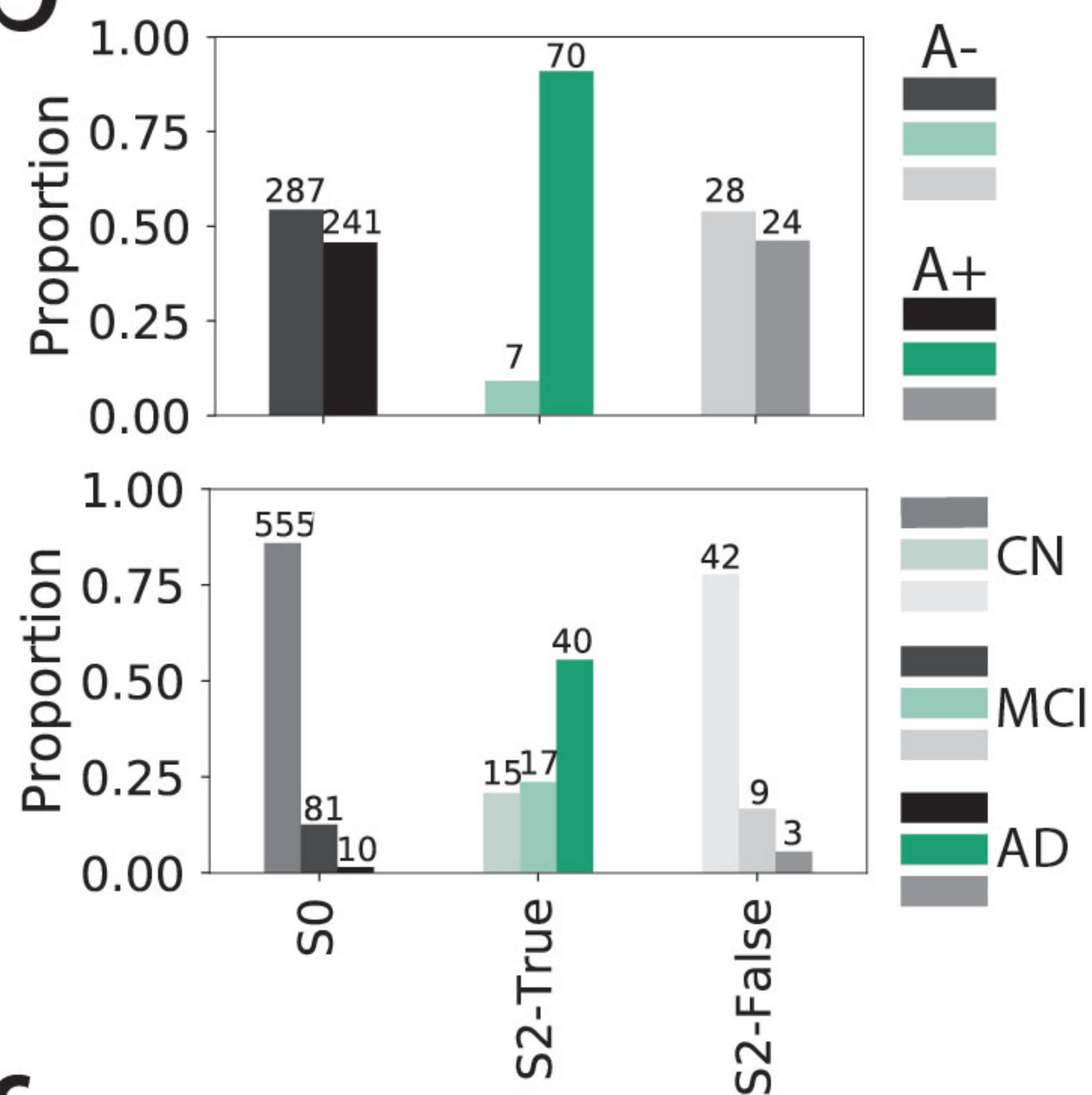
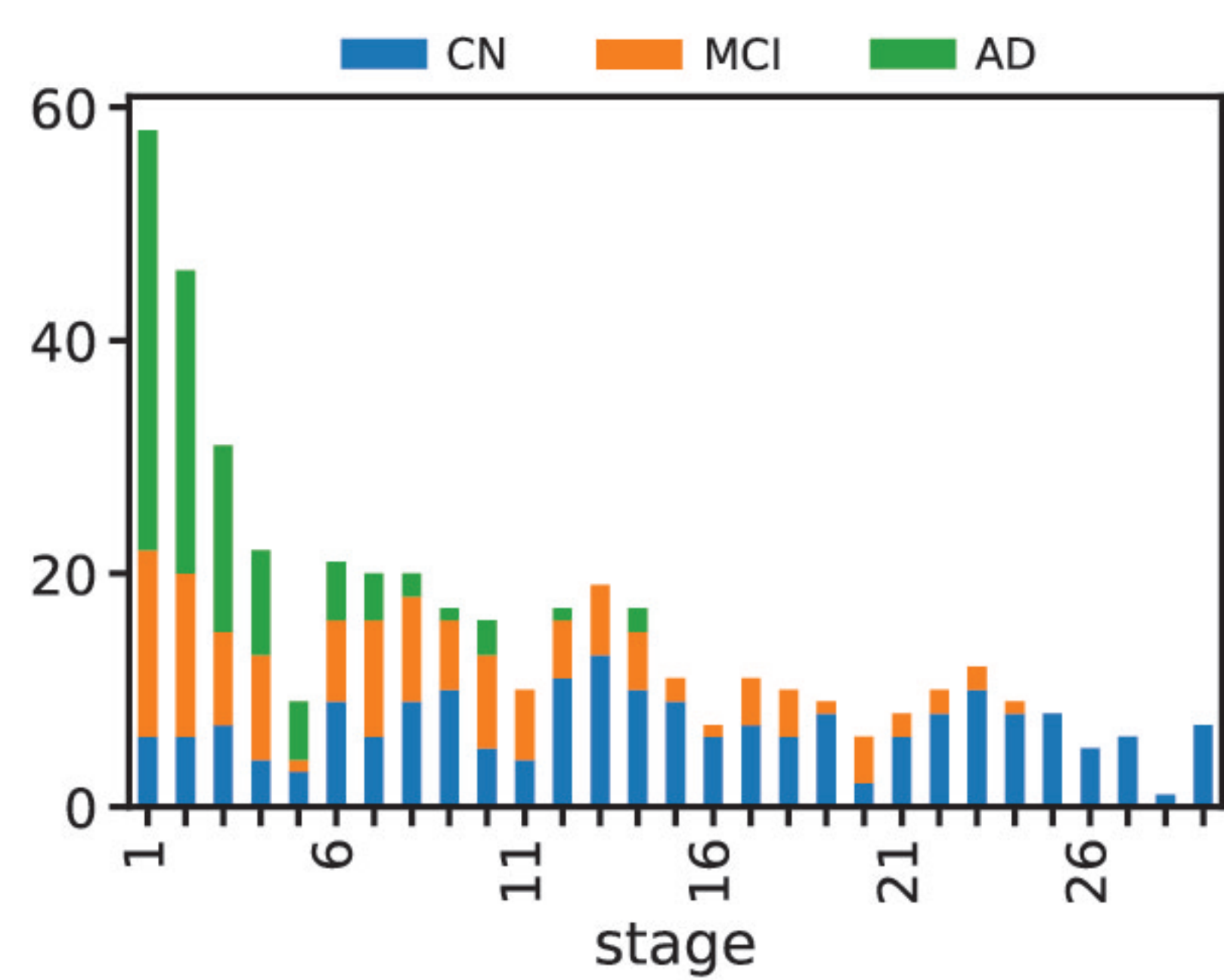
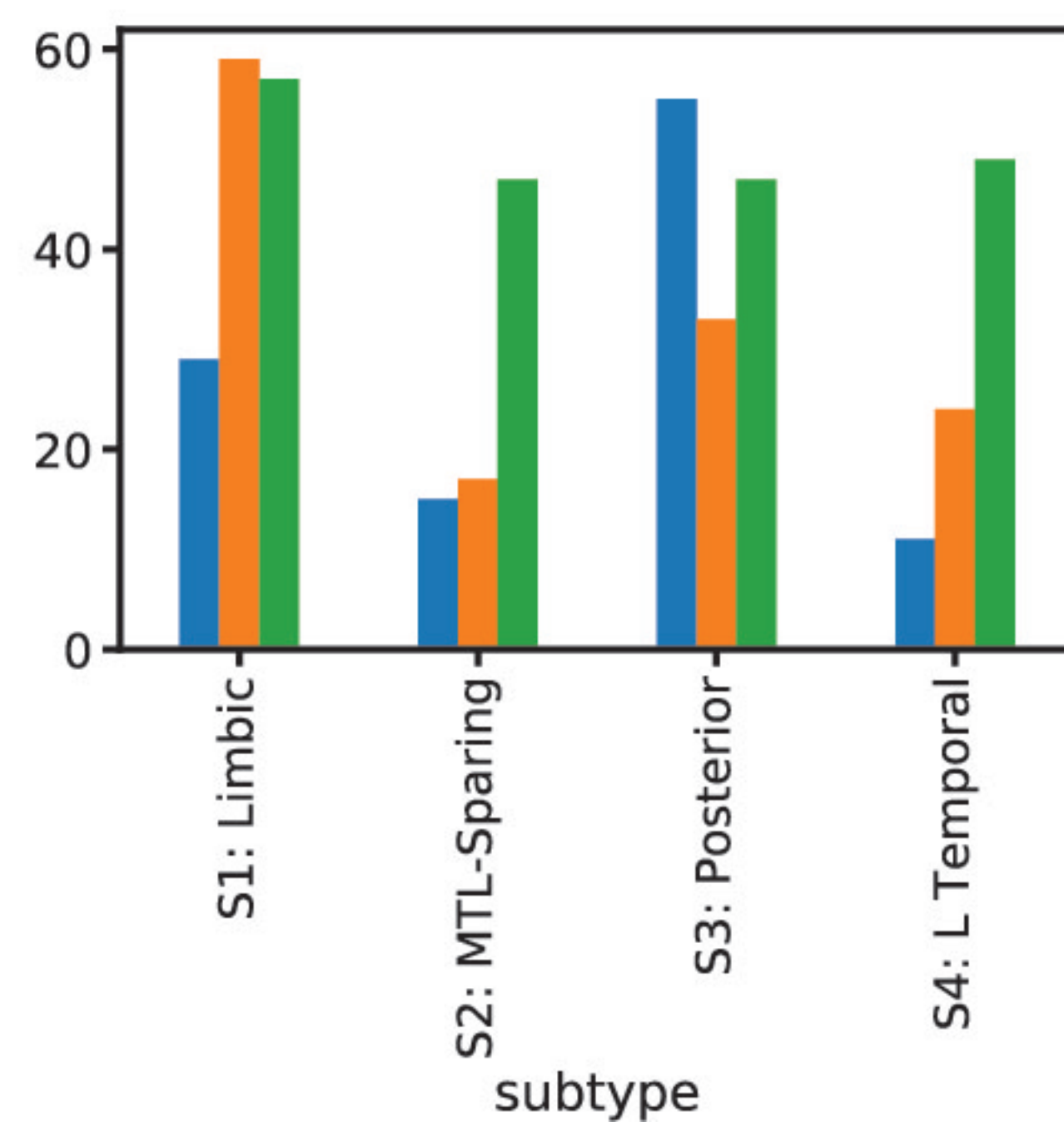
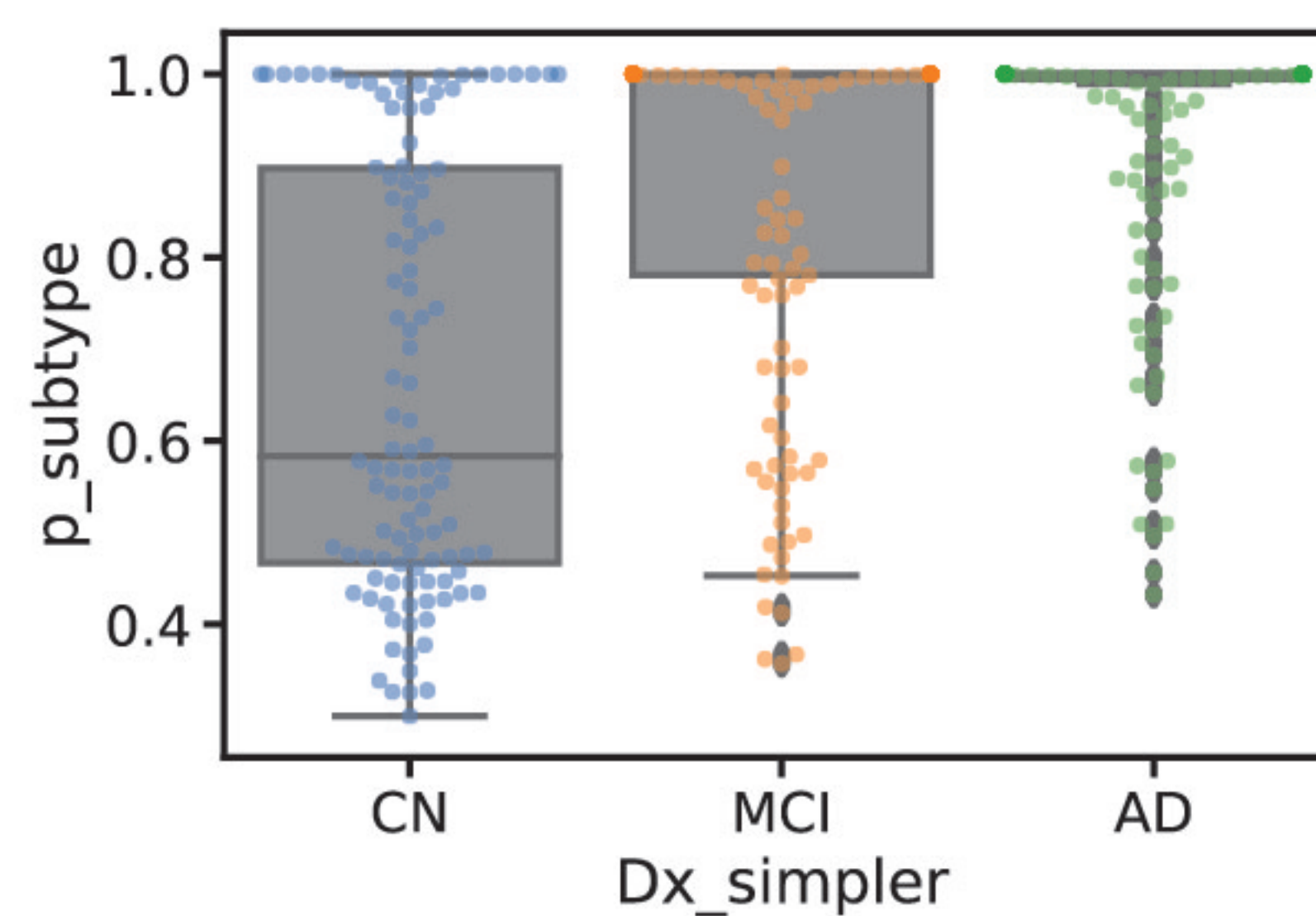
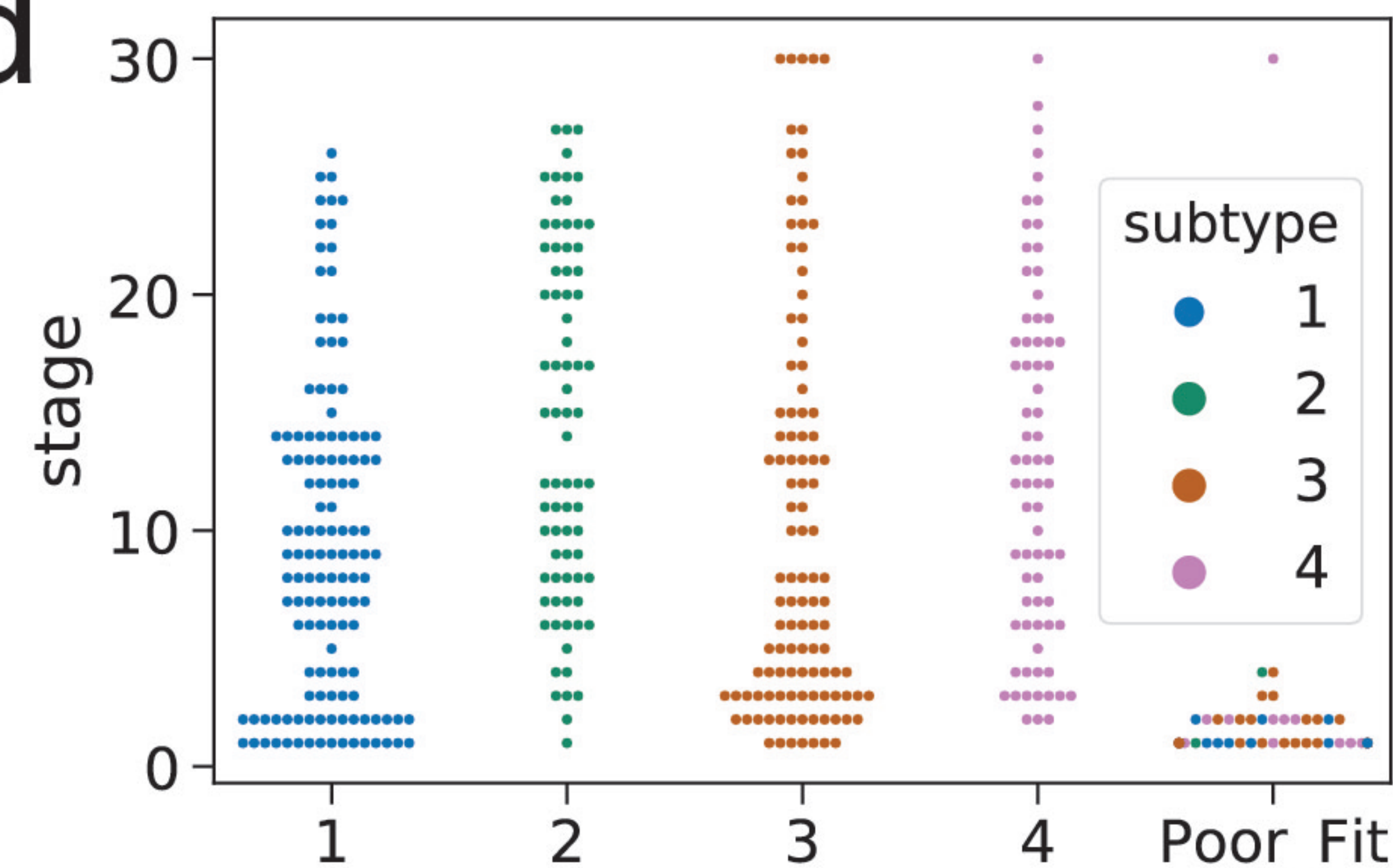
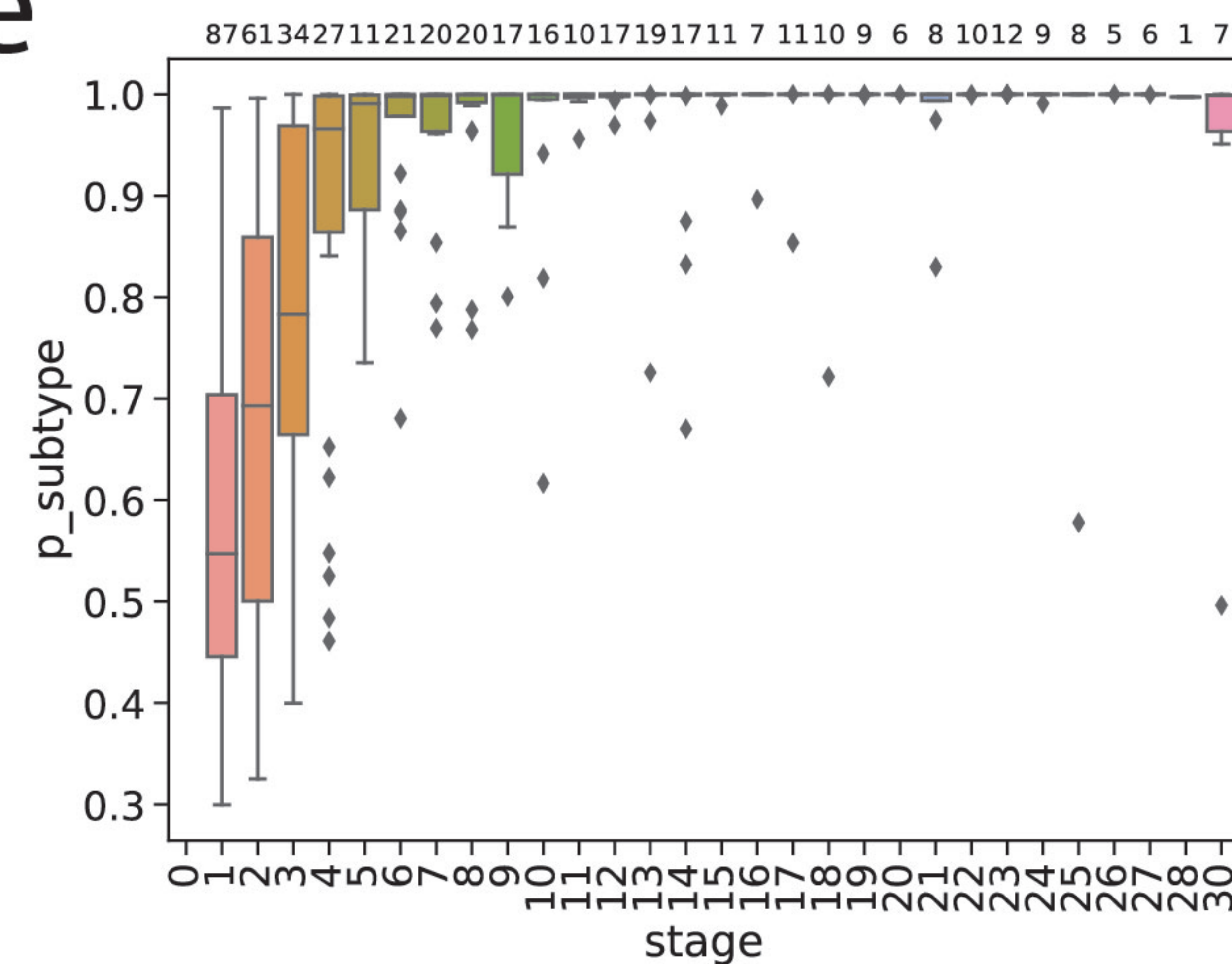
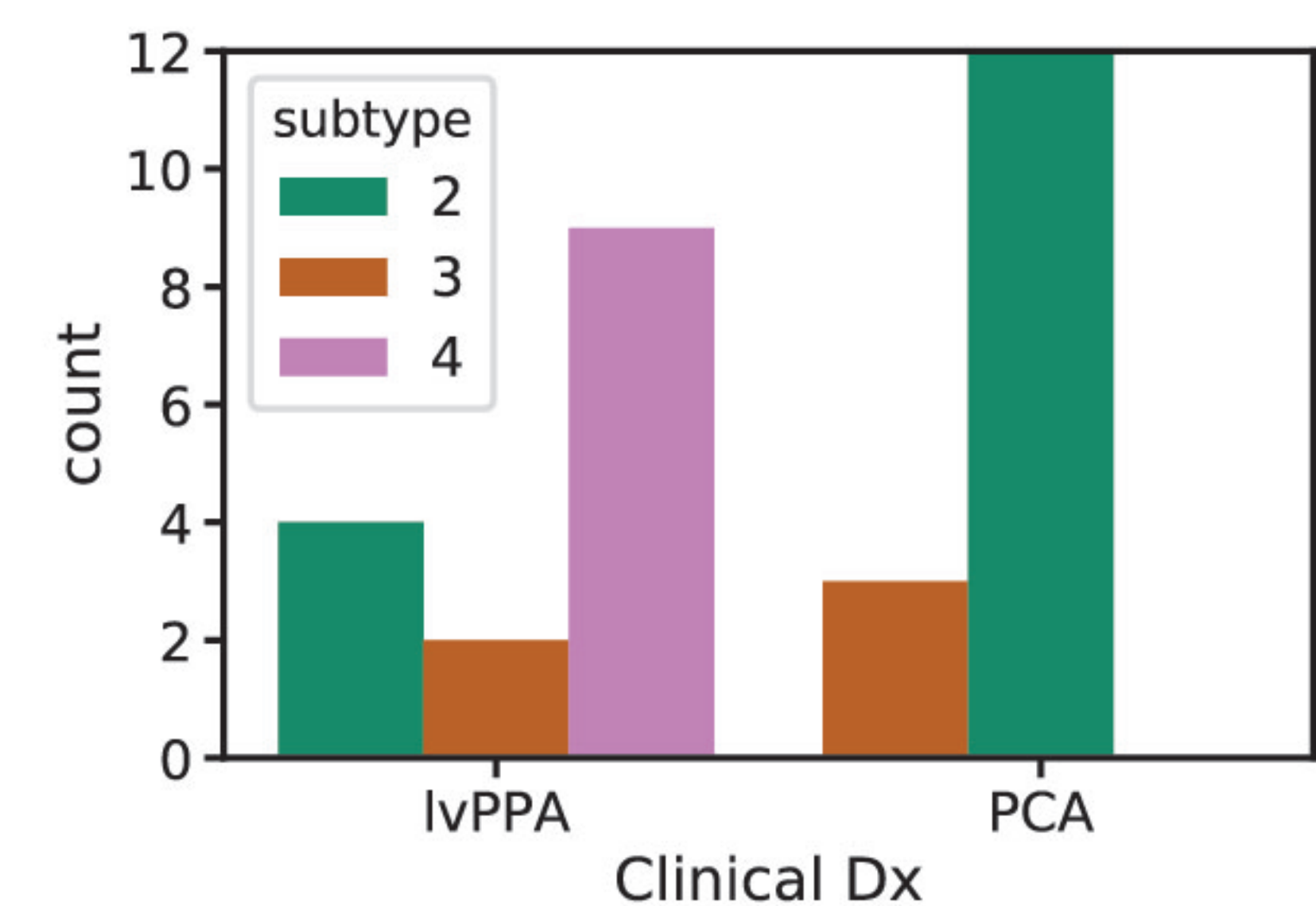
Visit 2

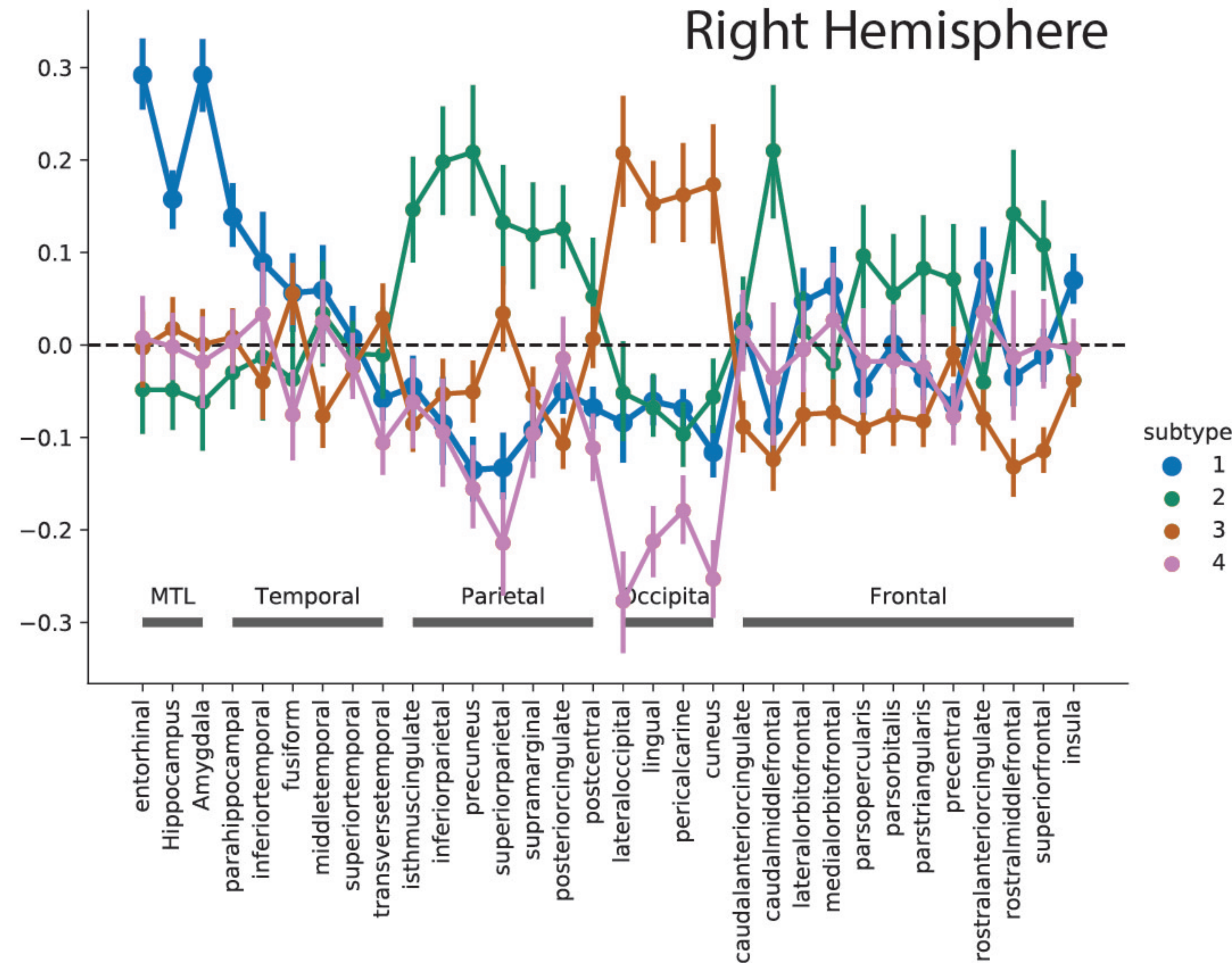
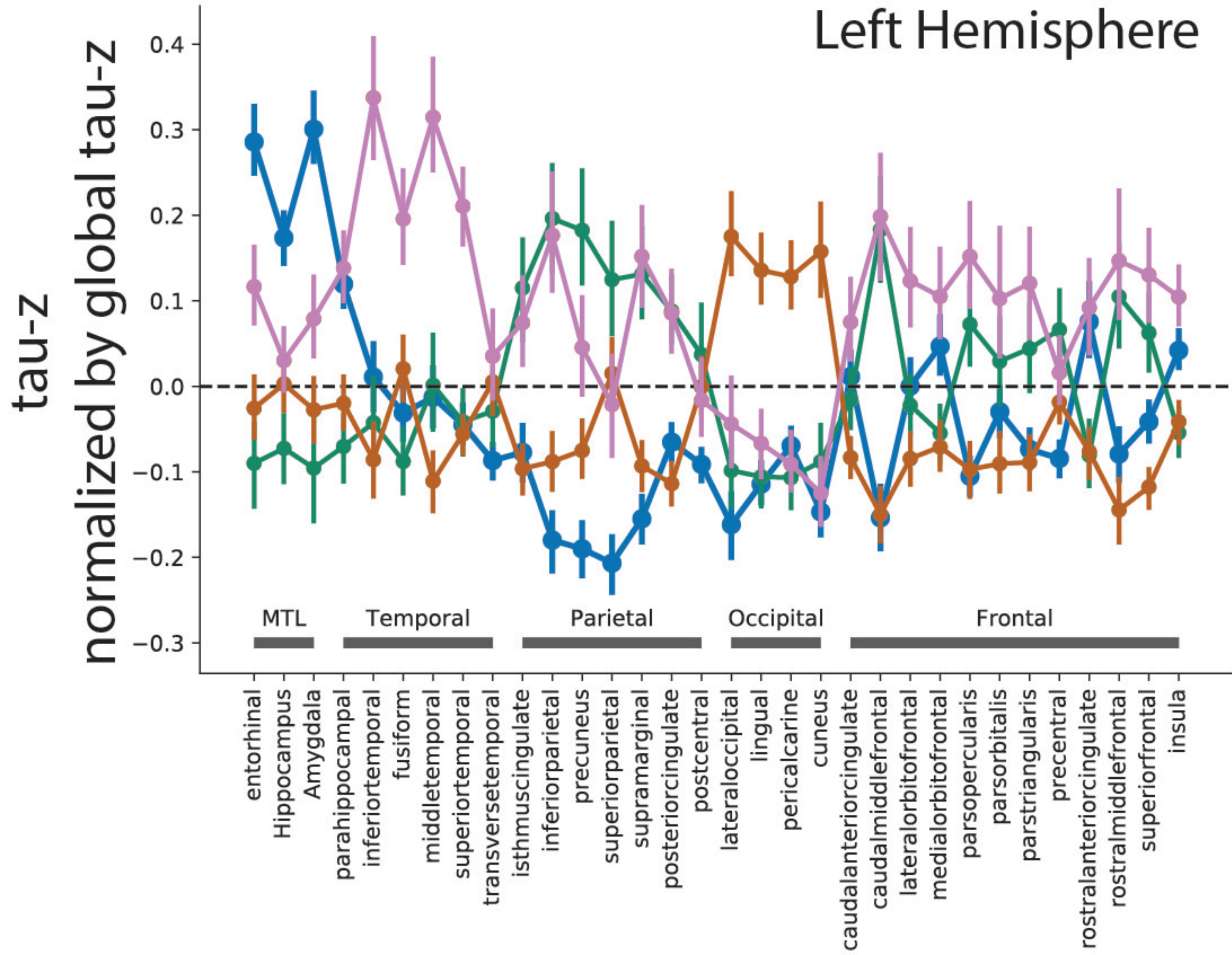


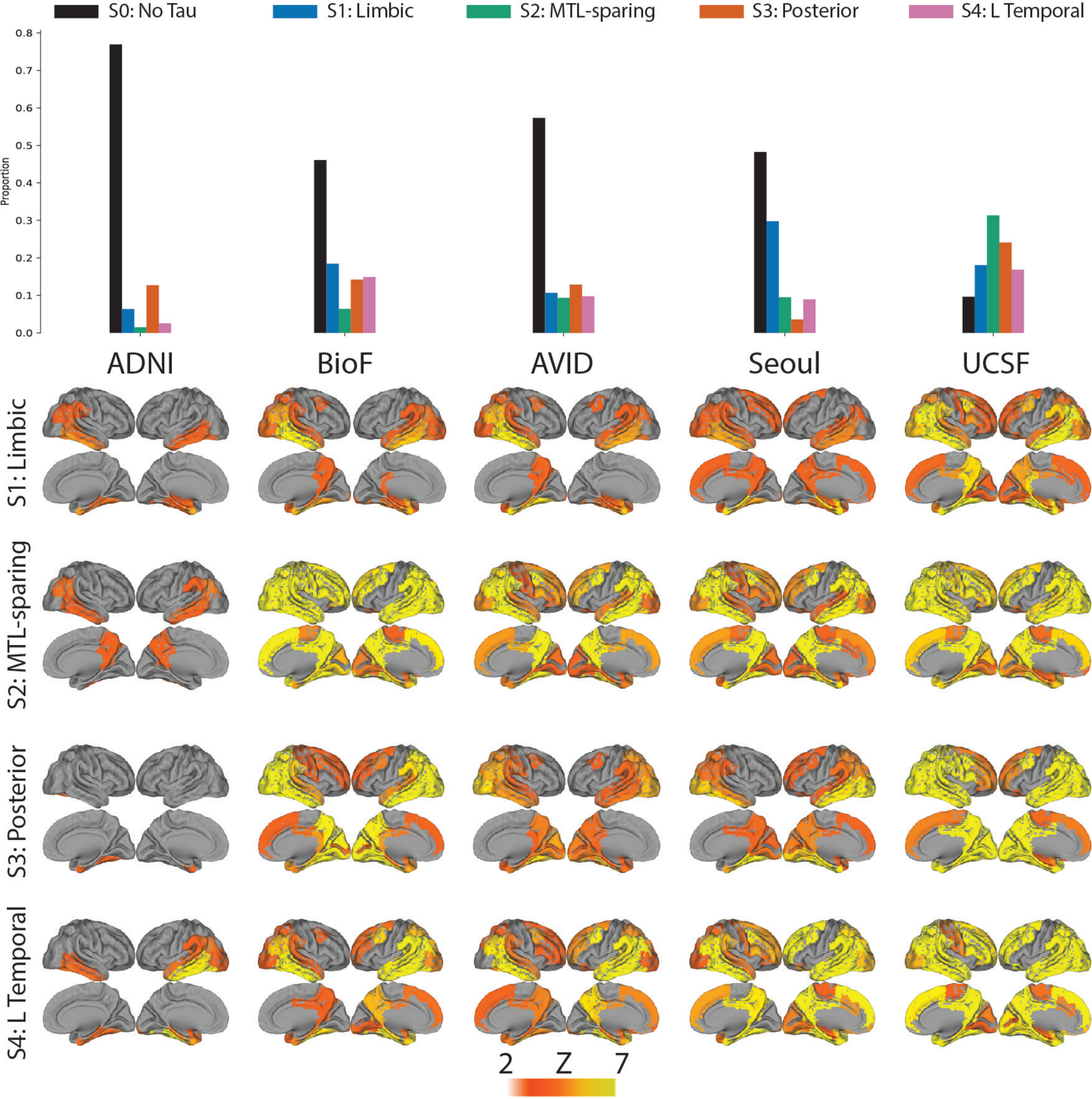


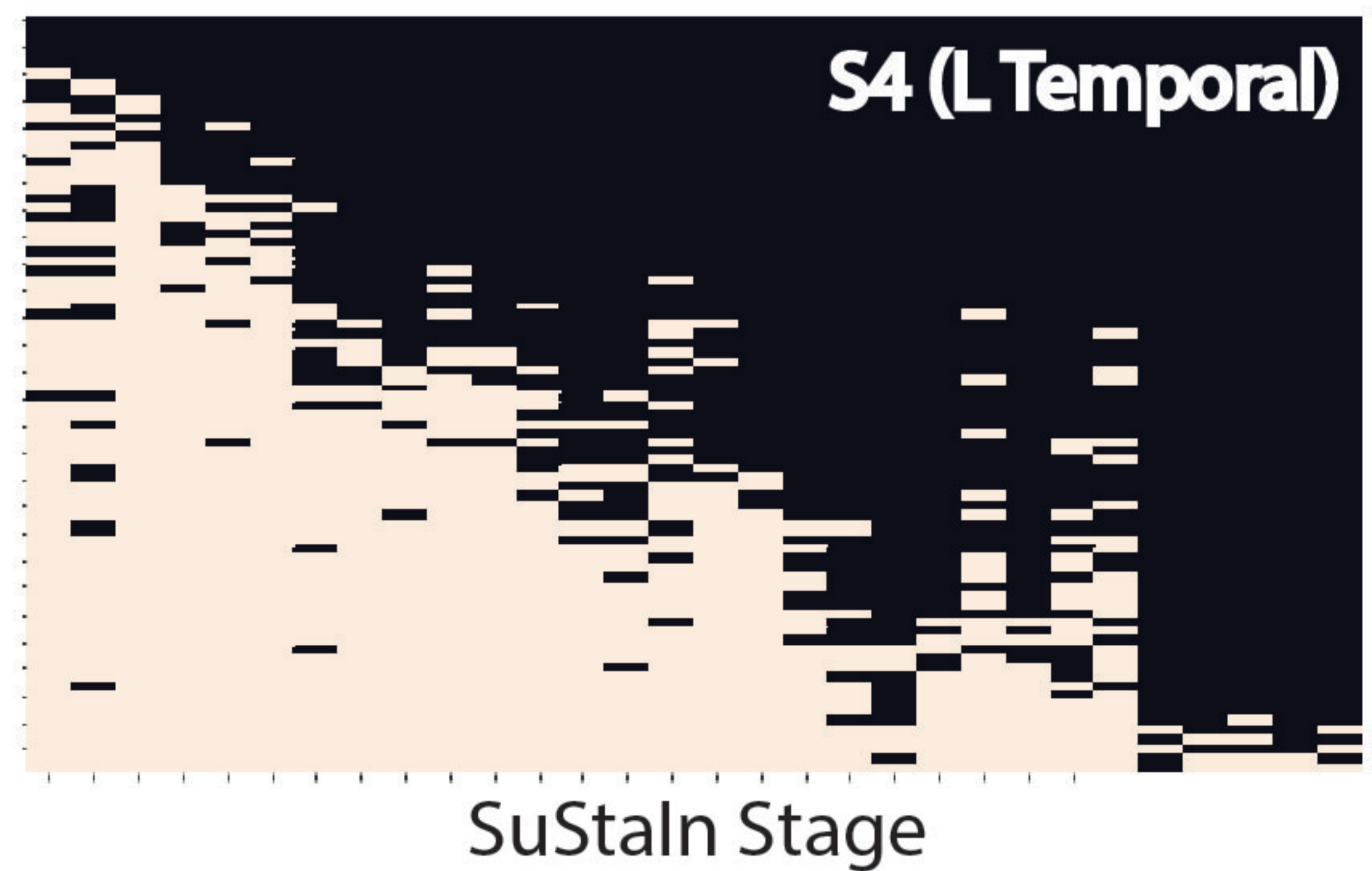
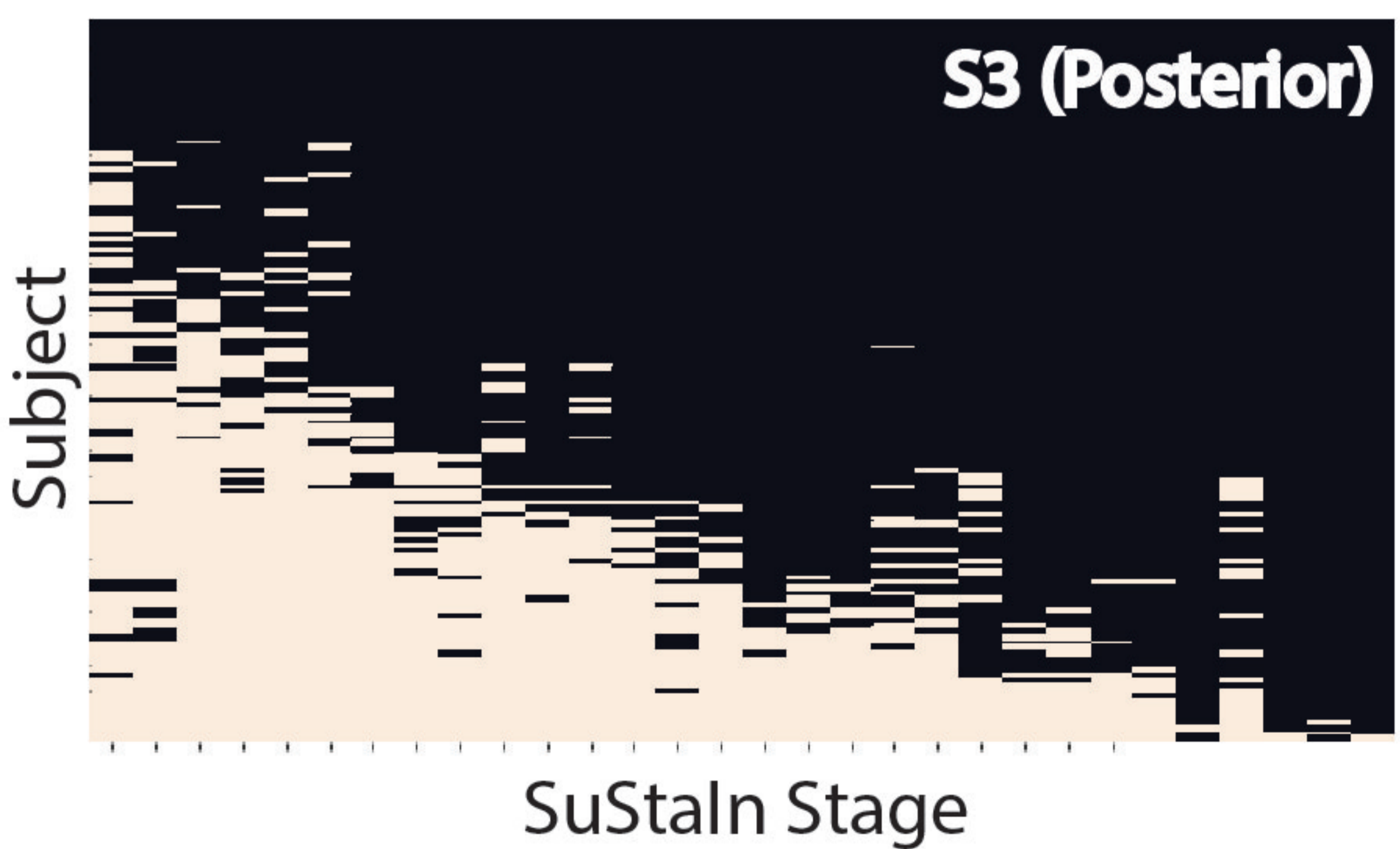
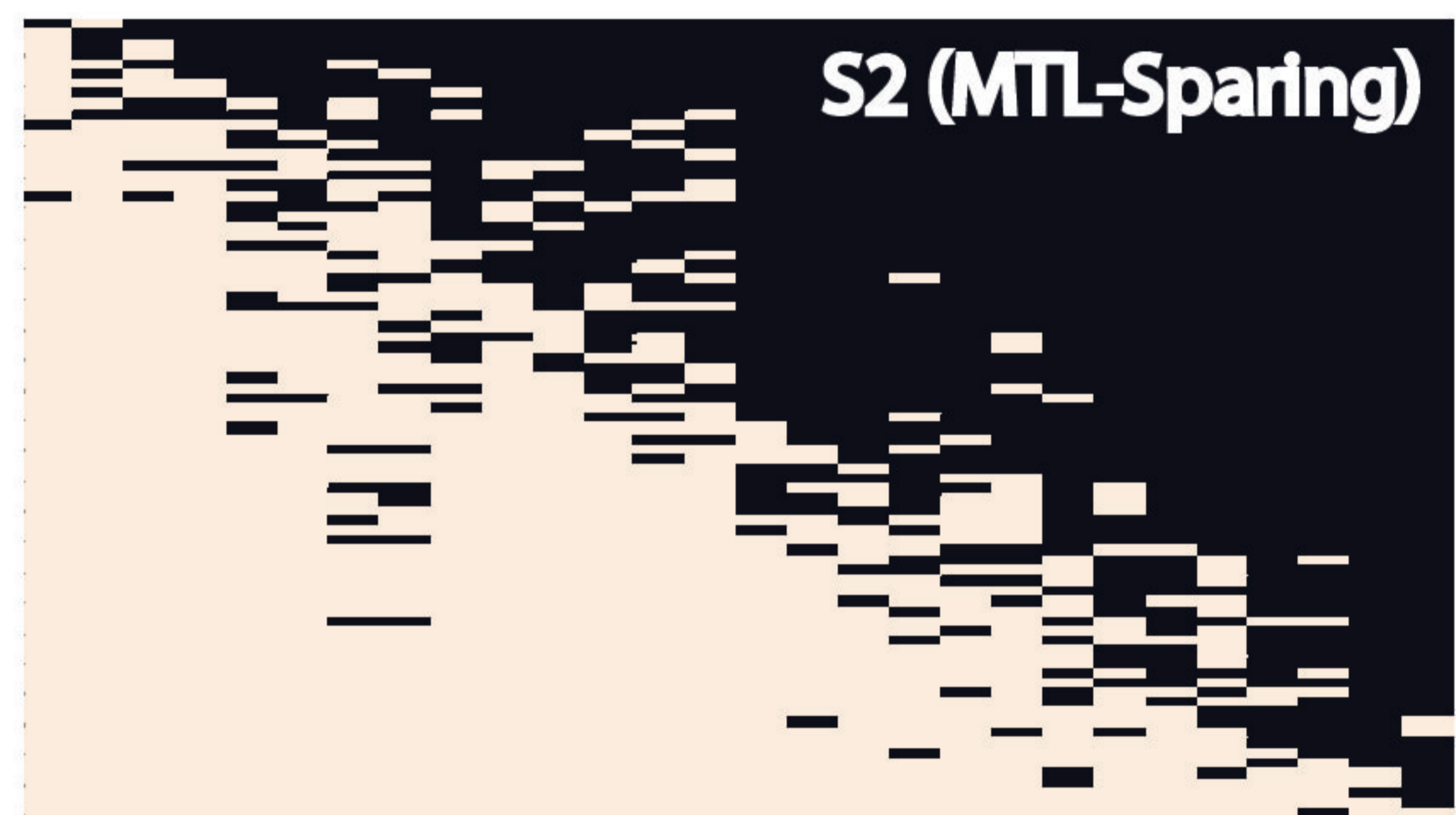
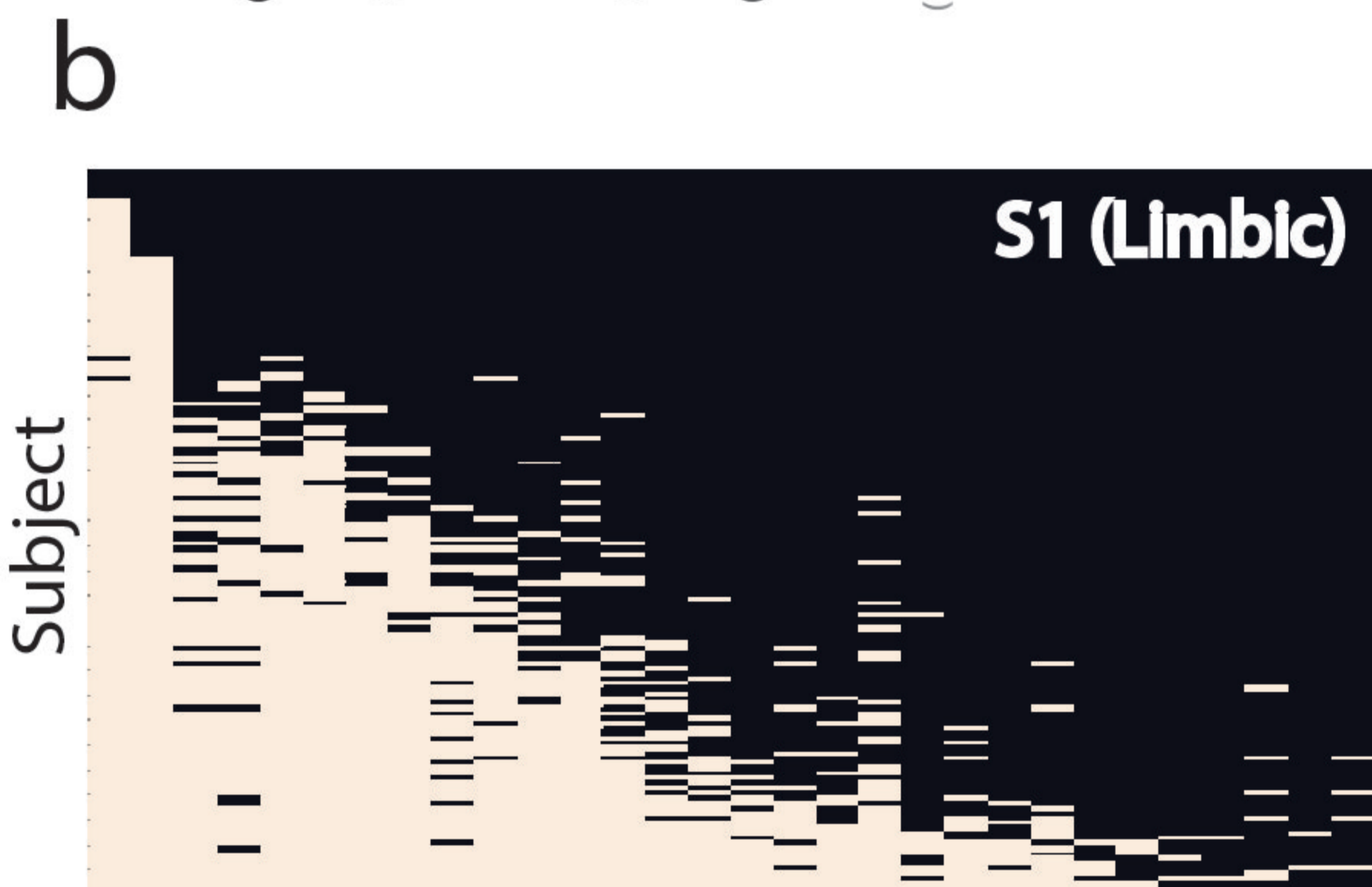
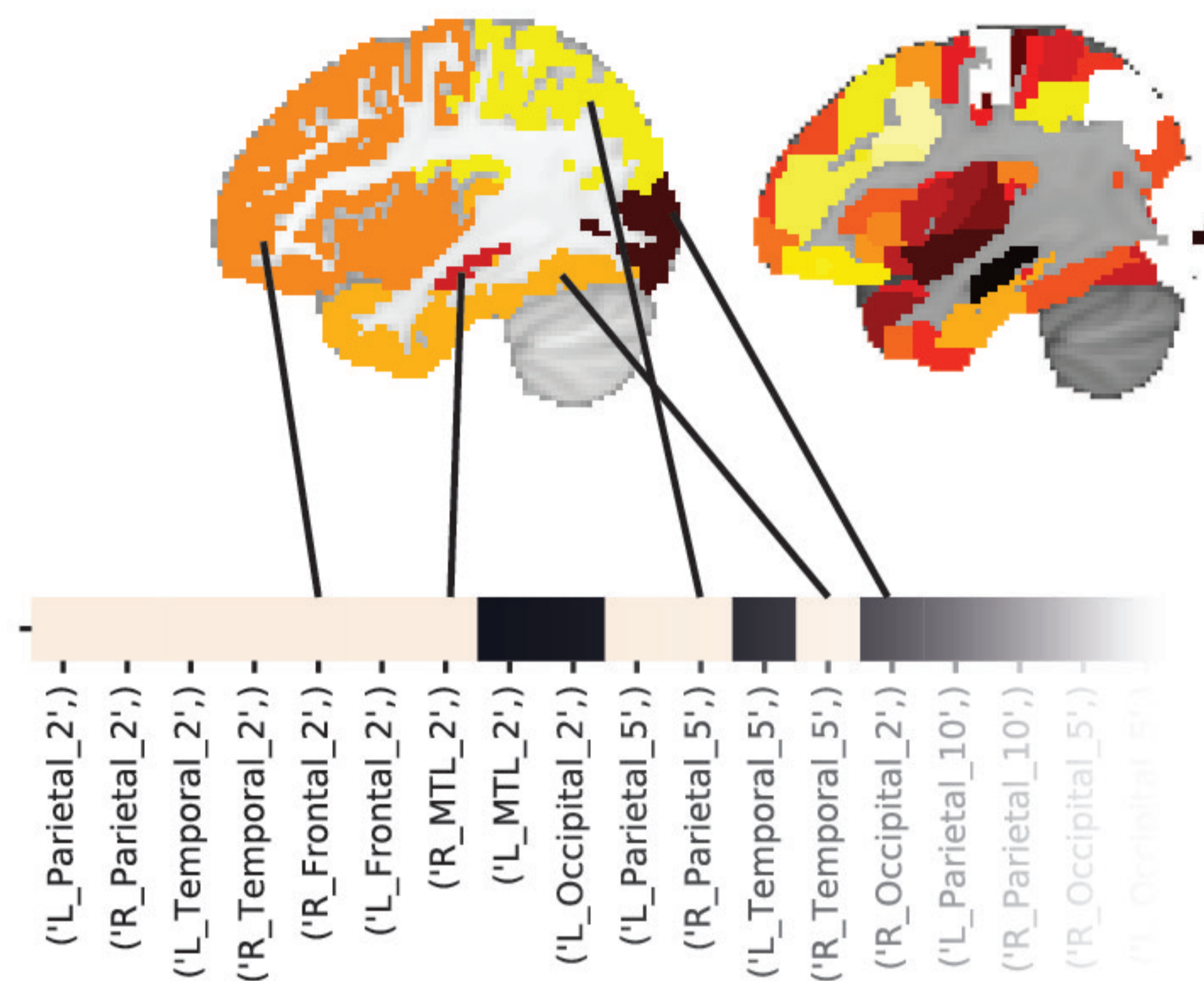
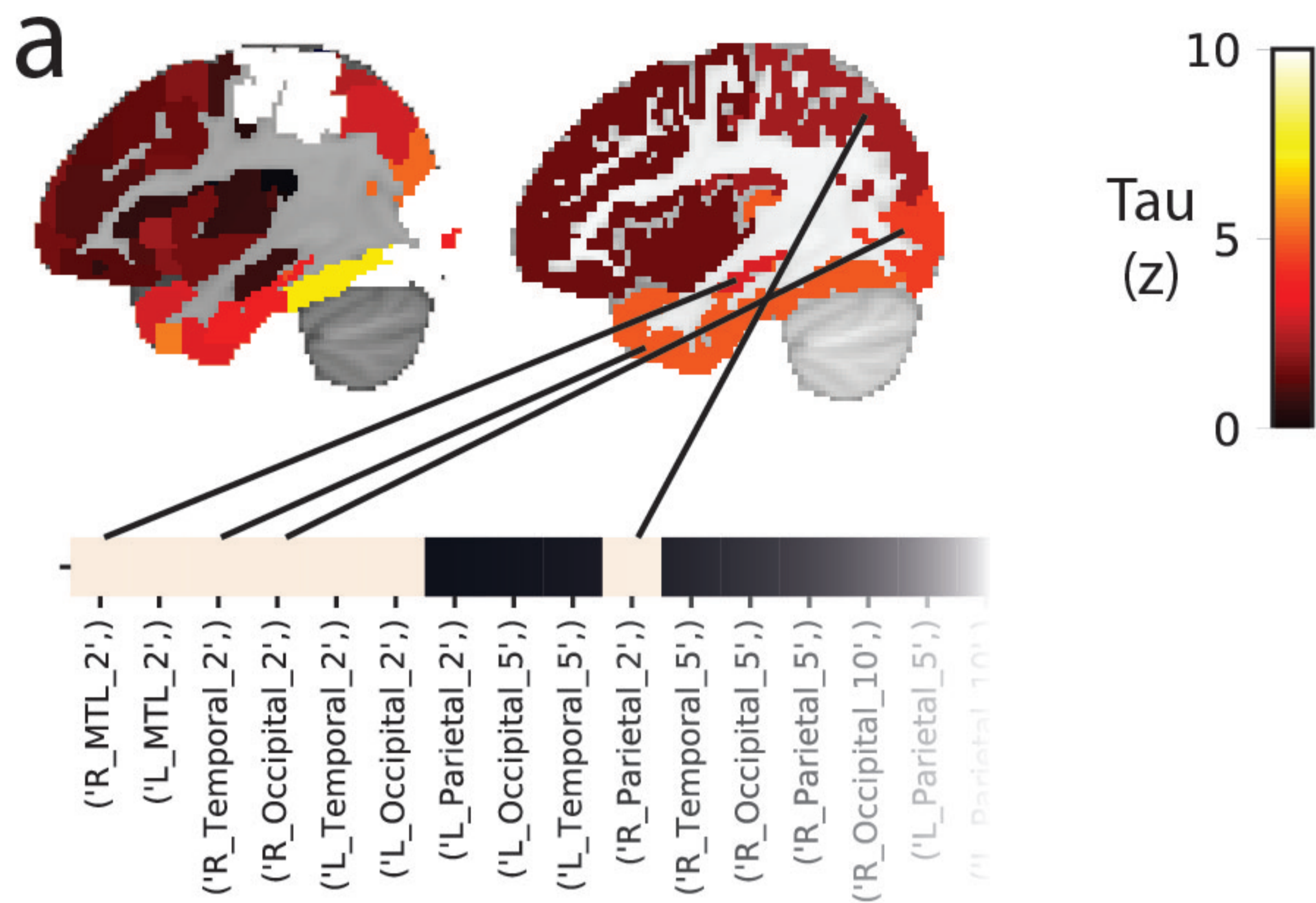


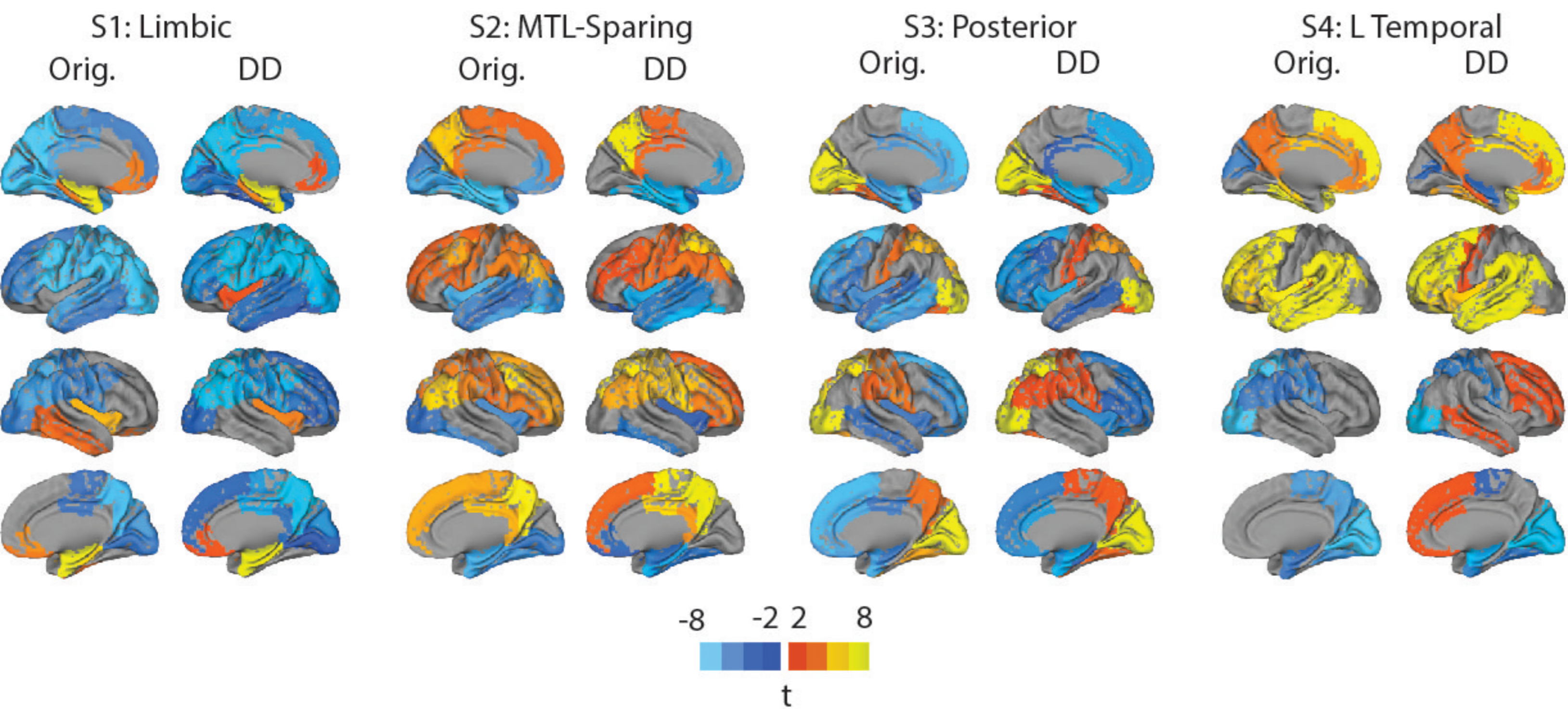
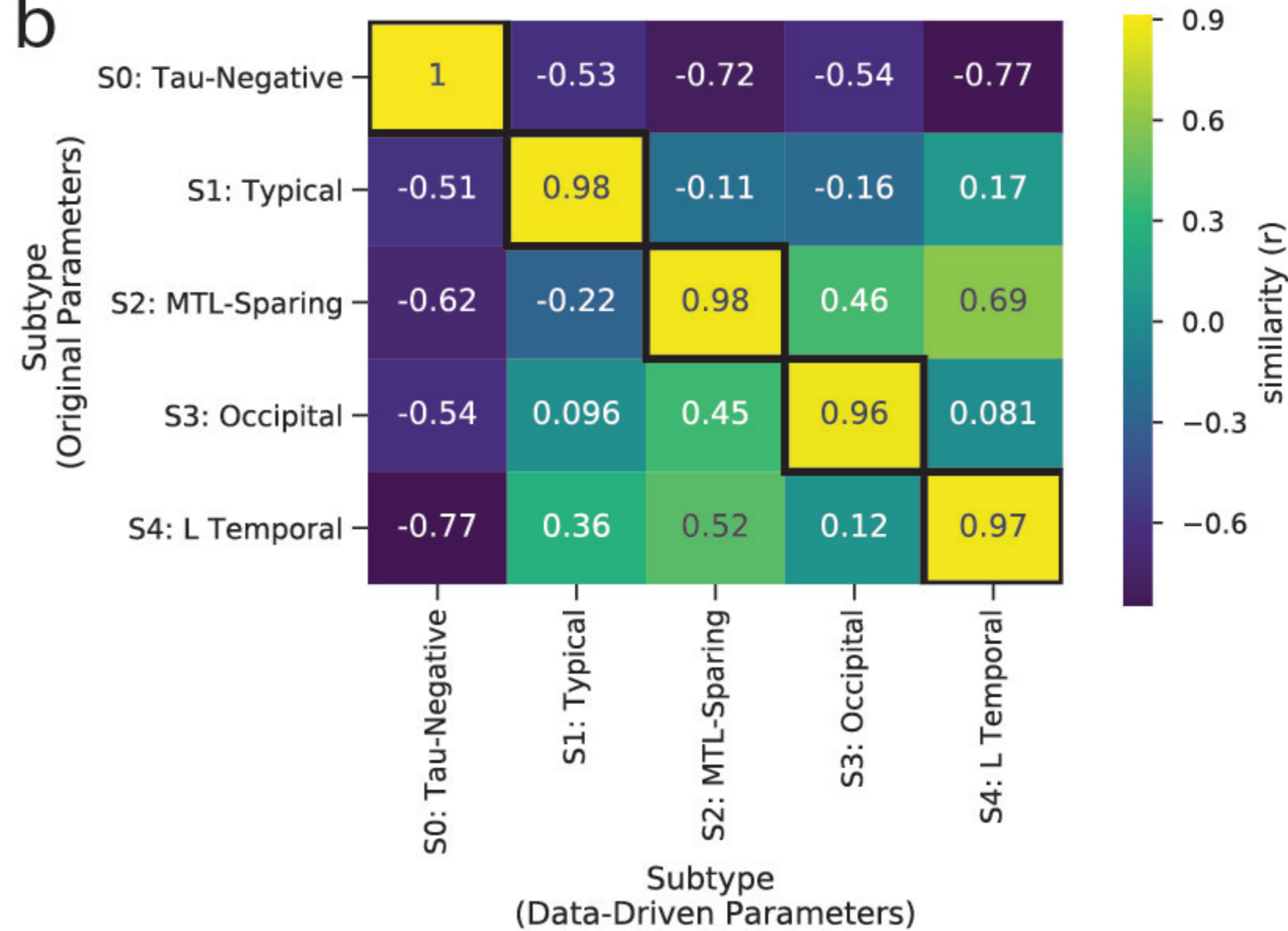


a**b****f****g****h****d****e****i**

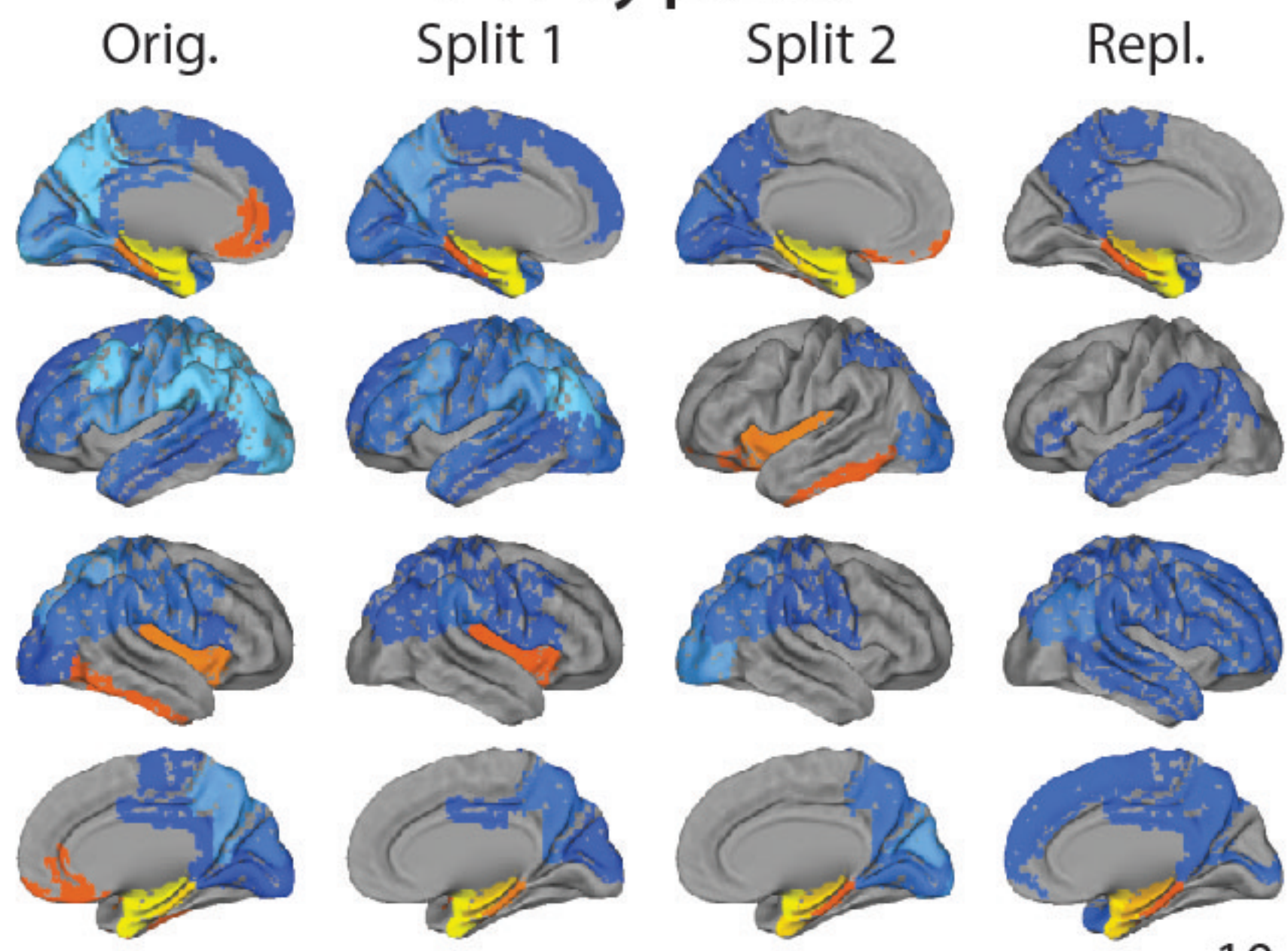




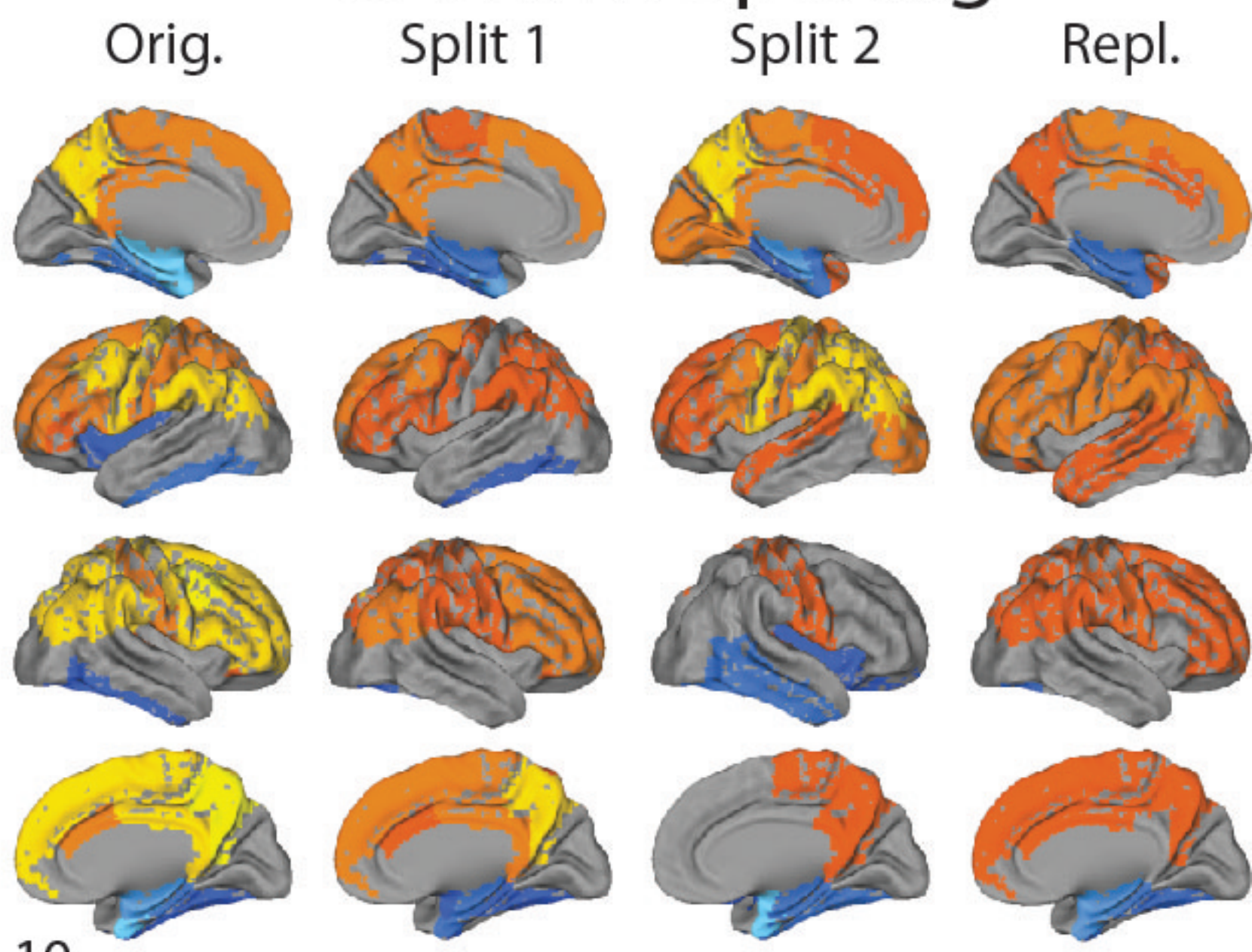


a**b**

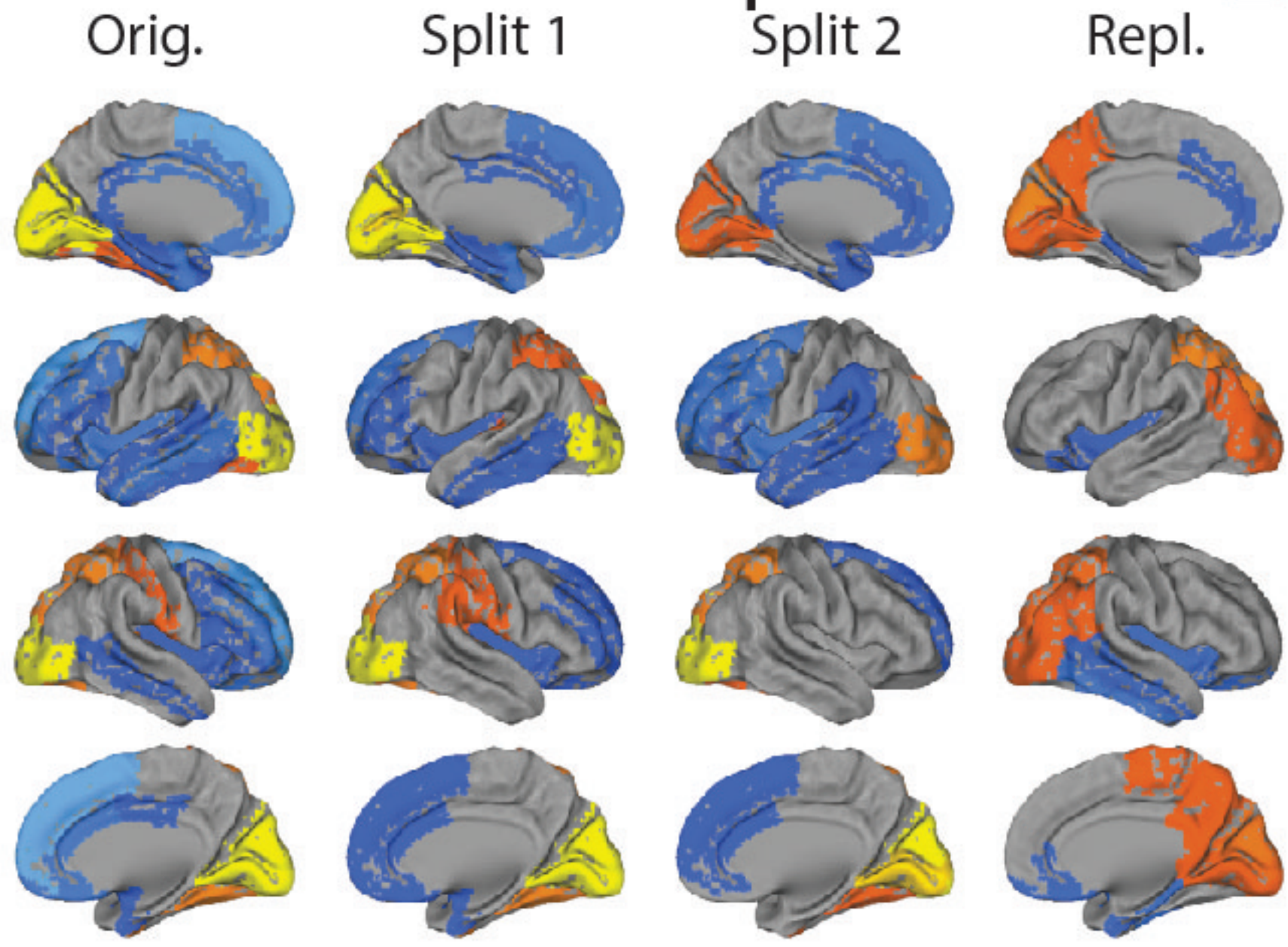
S1: Typical



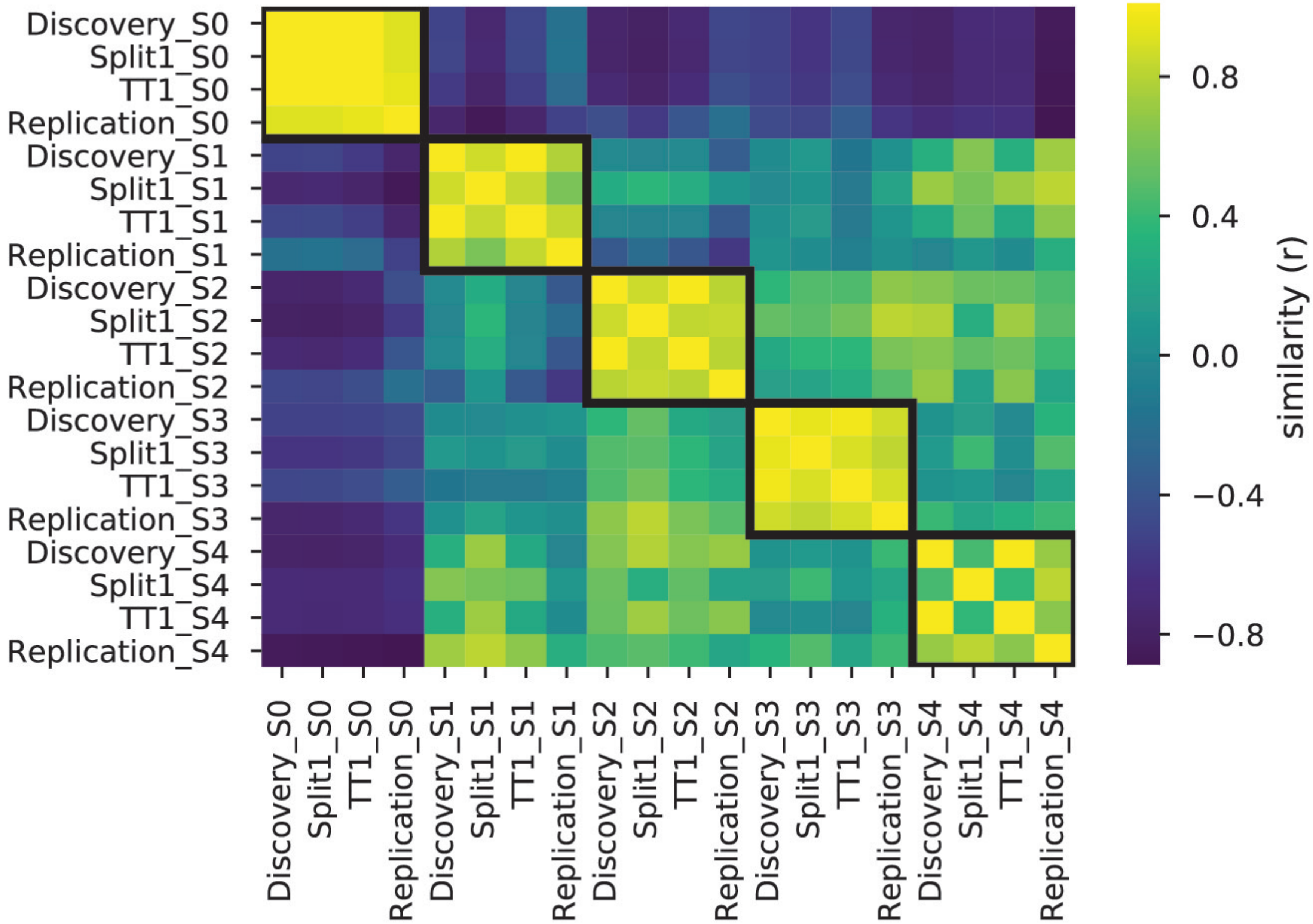
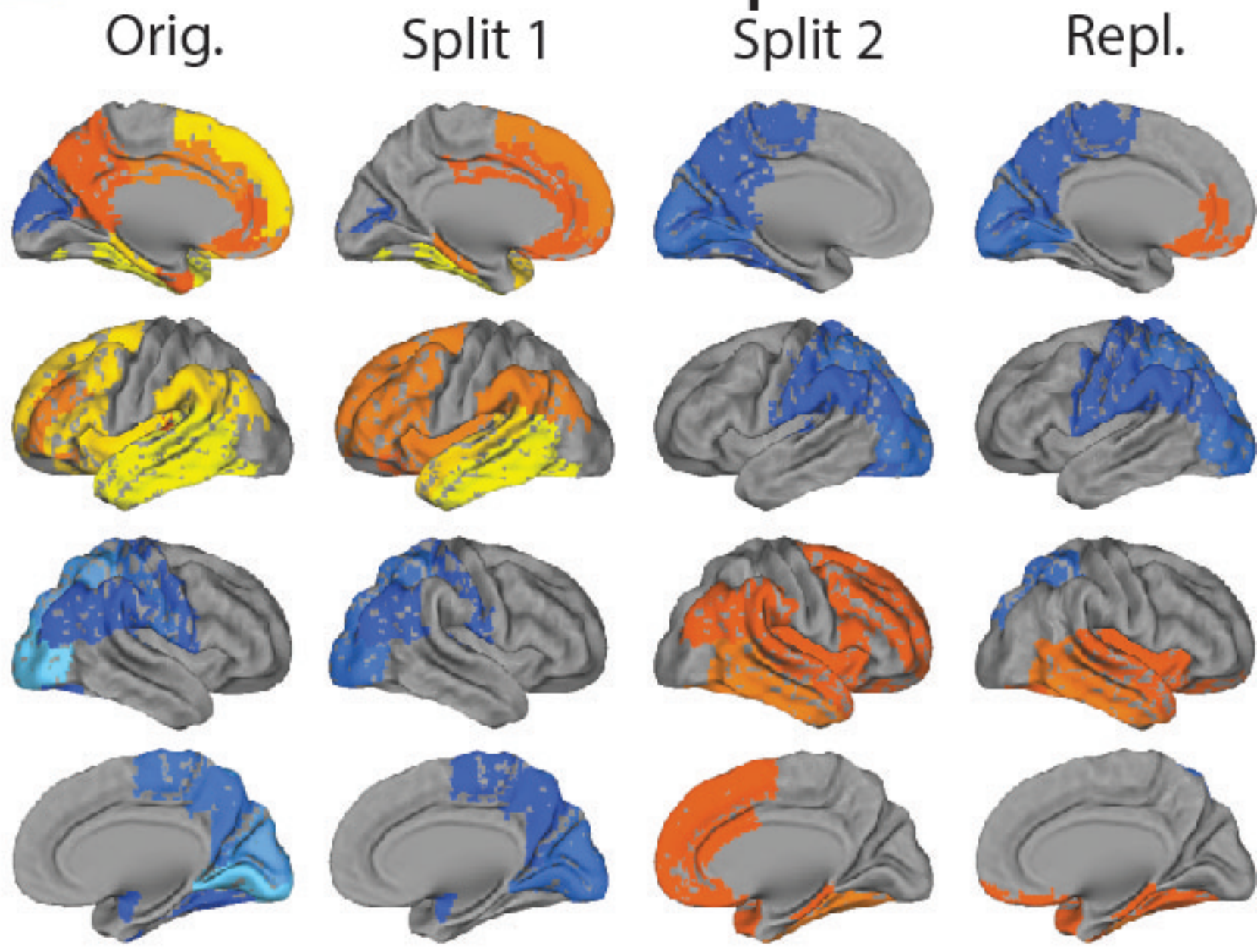
S2: MTL-Sparing

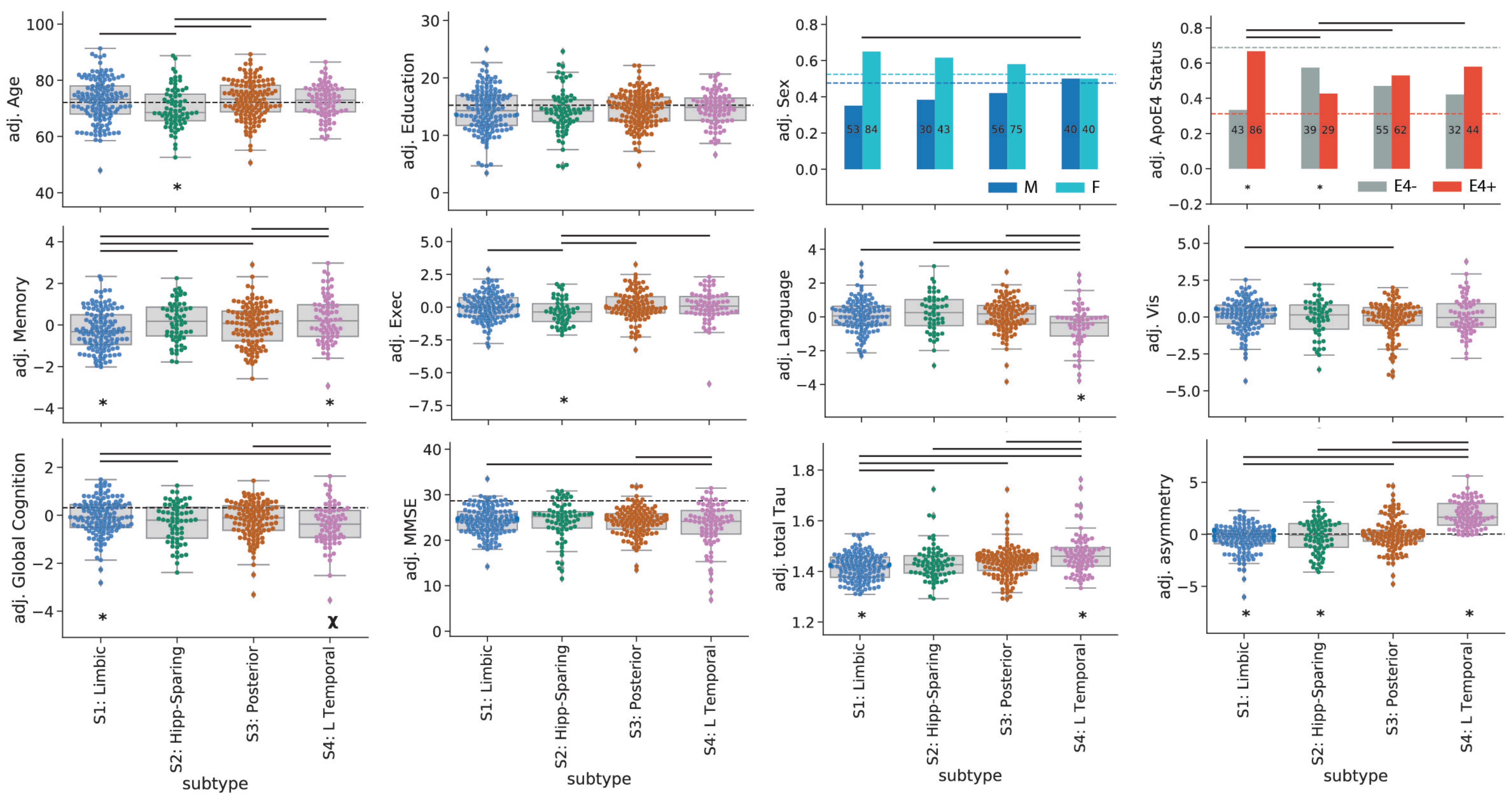


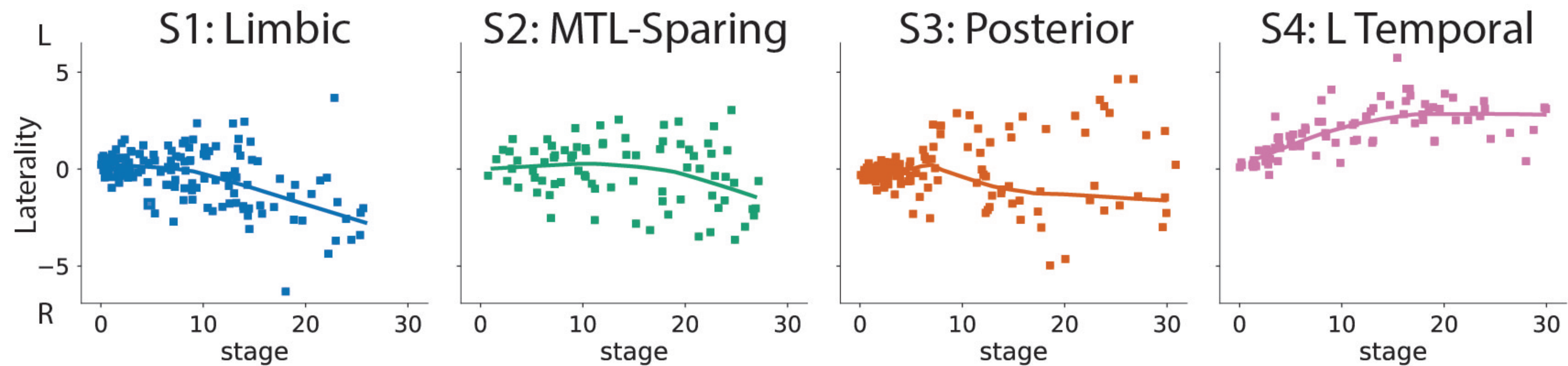
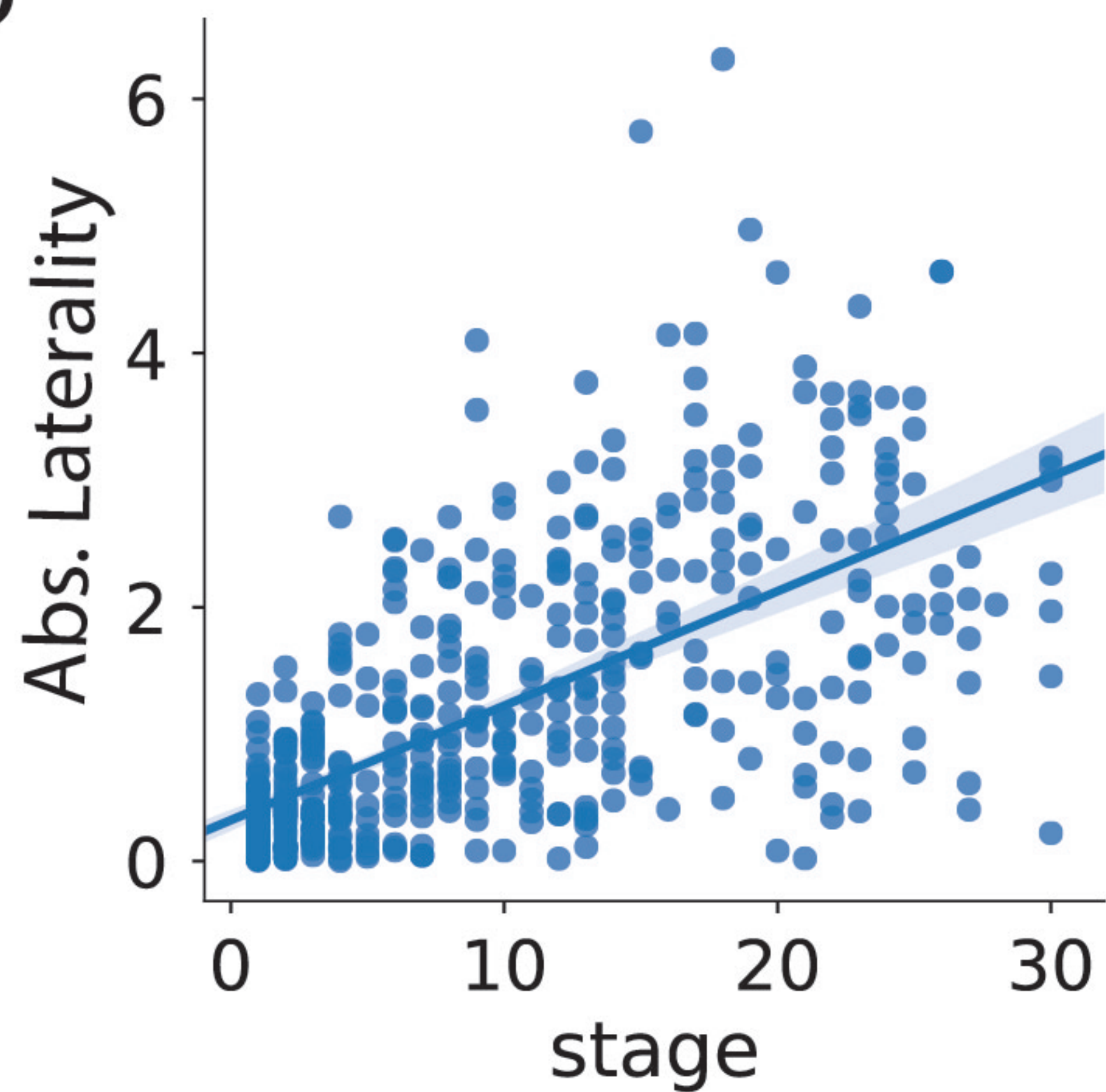
S3: Occipital



S4: L Temporal





a**b****c**